SP-1174

SAR ocean feature catalogue

GEN24

esa

esa SP-1174
October 1994

SAR ocean feature catalogue

J.A. Johannessen,* G. Digranes, H. Espedal
O.M. Johannessen & P. Samuel
Nansen Environmental & Remote Sensing Center
Edv. Griegsvei 3a
N-5037 Bergen, Norway
D. Browne, School of Ocean Sciences,
University of Wales, Bangor, UK
P. Vachon, Canada Centre for Remote Sensing,
Ottawa, Ontario, Canada

NERSC

*Now with ESA/ESTEC

european space agency / agence spatiale européenne

Title:
SAR ocean feature catalogue
Authors:
J.A. Johannessen*, G. Digranes, H. Espedal, O.M. Johannessen & P. Samuel
Nansen Environmental and Remote Sensing Center
Bergen, Norway
D. Browne, School of Ocean Sciences, University of Wales, Bangor, UK
P. Vachon, Canada Centre for Remote Sensing, Ottawa, Ontario, Canada
Technical contribution:
Juerg Lichtenegger, ESA, ESRIN
Published and distributed by:
ESA Publications Division, ESTEC, Noordwijk, The Netherlands
Printed in:
The Netherlands
Edited by:
W.R. Burke
Cover design by:
C. Haakman
Pre-press
P. Berkhout
International Standard Serial Number:
ISSN 0379 6566
International Standard Book Number:
ISBN 92-9092-133-1
Price:
50 Dutch Guilders (postage included)

*With ESA/ESTEC from 15 – 3 – 1994

Abstract

SAR-carrying satellites currently in orbit, and those planned for later this decade, provide images of the Earth at a variety of resolutions, incidence angles, radar wavelengths and polarisations. In order to take advantage of this large volume of data, it is essential that the means of interpreting SAR images of the ocean surface and applying them to practical problems be improved.

This SAR Ocean Feature Catalogue catalogue contains a selection of ERS-1 synthetic aperture radar (SAR) images, which illustrate radar backscatter signatures over the North Atlantic Ocean and coastal waters of Norway under a variety of environmental conditions.

The catalogue is intended to arouse and increase interest in SAR data as well as to provide guidance to SAR image interpretation. The catalogue is recommended for use in the education and training of operators at SAR receiving stations, ocean monitoring and forecasting centres, ship traffic control terminals and oil-pollution control authorities and of programme managers in industrial and government agencies.

Contents

Introduction

This catalogue was compiled for the European Space Agency and the Norwegian Space Centre by the Nansen Environmental and Remote Sensing Center under a study contract (10371/94/NL/US).

The European Space Agency (ESA) is an international organisation whose task is 'to provide for and to promote, for exclusively peaceful purposes, cooperation among European states in space research and technology and their space applications.' ESA has 14 Member States: Austria, Belgium, Denmark, Finland, Germany, Ireland, Italy, the Netherlands, Norway, Spain, Sweden, Switzerland and the United Kingdom. Canada takes part in some projects under a cooperation agreement. ESA's contribution to the monitoring of the environment worldwide in the nineties consists of a series of Earth-observation satellites of which ERS-1 is the first. ERS-2 will follow in late '94 or early '95, while ENVISAT is scheduled to be launched in '98. As part of the Prodex Programme, ESA has agreed to contribute to the development of means by which data from the SAR sensor on board ERS-1 can be used to monitor coastal waters and the ice-infested regions of the European Arctic.

The Norwegian Space Centre (NSC) is an independent organisation, established in 1989. The Centre works in accordance with government guidelines, for the benefit of — and in co-operation with — industry, research institutes, official agencies and norwegian interests in general. One of the Norwegian Space Centre's main priorities is Earth observation. On the basis of user requirements, the NSC has supported a national programme for developing near-real-time marine application of radar data from satellites. A national infrastructure has been set up for this purpose, and Tromsø Satellite Station has delivered the SAR, data presented in this report.

The Nansen Environmental and Remote Sensing Center (NERSC) is an independent, nonprofit, environmental- and climate-research institute affiliated to the University of Bergen. NERSC plans and performs basic and applied research programmes and projects funded by governmental agencies, research councils and industry. Research covers ice and ocean monitoring, climate modelling and application of remote sensing techniques to vegetation mapping.

The catalogue contains a selection of ERS-1 synthetic aperture radar (SAR) images, which illustrate radar backscatter signatures over ocean and coastal waters under a variety of environmental conditions. SAR-carrying satellites currently in orbit, and those planned for later this decade (Table 1), provide images of the Earth at a variety of resolutions, incidence angles, radar wavelengths and polarisations. In order to take

Table 1: SAR platforms this decade

Satellite	Wavelength	Pol	Cycle	Modes	Swaths	Launch/Life time
ALMAZ 1B	0.096 m	HH	variable	1	30—45 km	31 March 1991 — 17 Oct. 1992
ERS-1	0.057 m	VV	3/35 days	1	100 km	17 July 1991 —
JERS-1	0.235 m	HH	44 days	1	75 km	11 February 1992 —
ERS-2	0.057 m	VV	3/35 days	1	100 km	21 April 1995 —
Radarsat	0.057 m	HH	24/72 days	5	50—500 km	second half 1995 —
Envisat ASAR	0.057 m	VV/HH	35 days	5	50—410 km	1998 —

advantage of this potentially enormous volume of data, it is essential that the means of interpreting SAR images of the ocean surface and applying them to practical problems be improved. Consequently, this catalogue is intended to arouse and increase interest in SAR data as well as to provide guidance to SAR image interpretation. The catalogue is recommended for use in the education and training of operators at SAR receiving stations, ocean monitoring and forecasting centres, ship traffic control terminals and oil-pollution control authorities and of programme managers in industrial and government agencies.

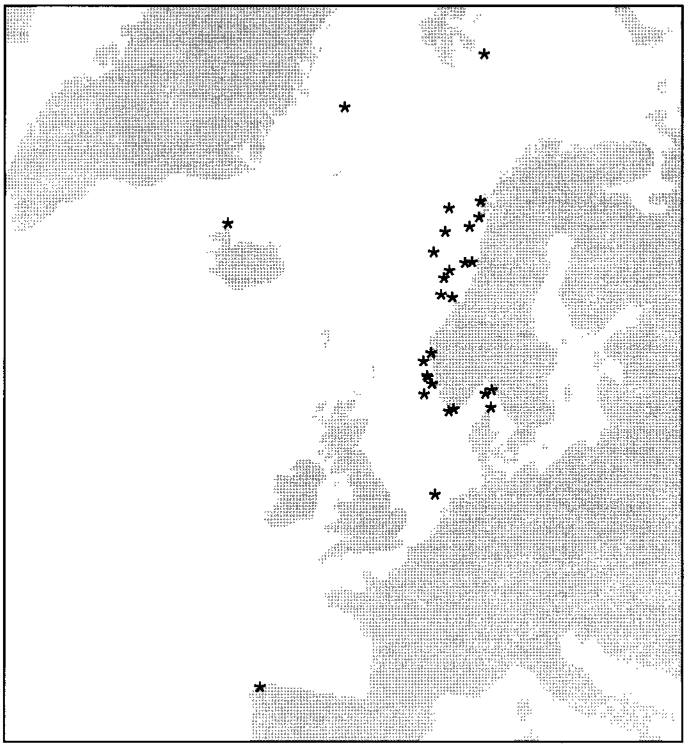

Figure 1: Locations of the SAR images used in the catalogue

The ERS-1 SAR images selected are mostly of the seas and coastal waters around Norway, from the launch date of ERS-1 in July 1991 up until December 1993. The centre positions of the scenes are marked by asterisks in Figure 1.

Unless indicated otherwise, the images in the catalogue are shown at full frame size, i.e. 100×100 km, and are based on the 100 m resolution images from Tromsø Satellite Station (TSS). In some cases, two or three images are concatenated, but the scale can be found from the fact that the width is still 100 km. A latitude/longitude grid is overlaid on each image and an accompanying figure shows:

— range/azimuth directions;
— an estimate of the overall wind conditions in the image. The wind data are taken from records made by the nearest meteorological stations.

The wind direction is given with respect to the image, and the wind speed is indicated by a long feather for 5 m/s and a short one for 2.5 m/s (1 m/s $\approx$2 knots). An interpretation and a weather map are shown on the page opposite each image. In the interpretation cartoon, land is masked out and grey arrows indicate positions of given radar cross-section profiles. A frame box indicates the position of the SAR image on each weather map.

In Section 2, the catalogue gives a brief review of the ERS-1 SAR sensor's characteristics, imaging principles and theory. A list of references is included for readers who wish to pursue these topics in more depth. Section 3 contains the SAR images classified by subject. Each subject is briefly described and interpreted. Section 4 contains one daily and one seasonal time series of SAR images. The appendix contains abstracts of some relevant recent publications. Reprints of the publications are available from NERSC on request. The address is given in the appendix.

We wish to thank Terje Wahl and Tom Andersen at the Norwegian Defence Research Establishment (NDRE) for their contribution to the catalogue. They have analysed a large number of images in an oil spill detection project [Wahl et at., 1994], and several of the images used in the catalogue have been supplied by them.

2. ERS-1 SAR

2.1 The instrument

Synthetic aperture radar is a side-looking imaging radar operating from a moving platform. SAR images of the Earth's surface represent the spatial pattern of reflected microwave energy. A series of electromagnetic pulses is transmitted towards the Earth in a direction perpendicular to the platform track. The pulses illuminate an elliptical footprint on the Earth's surface owing to the directional properties of the antenna (see Figure 2). The strength of the signal that is returned from area covered by the footprint depends upon the physical characteristics of the surface. The amount of energy reflected from a point target is given by the radar cross section, RCS, defined as the projected area (πr^2) of a metal sphere ($r \gg \lambda$) that returns the same echo signal as the target. For a diffuse target, such as the ocean surface, σ^0 is used. σ^0 is defined as the mean RCS normalised with respect to the illuminated projected area on the ground. σ^0 is expressed in dB, σ^0 of 0 dB being equivalent to 1 m^2 sphere per m^2 ground area. Quantifying the cross-sectional values makes it possible to relate the returned energy to the physical properties of the scene.

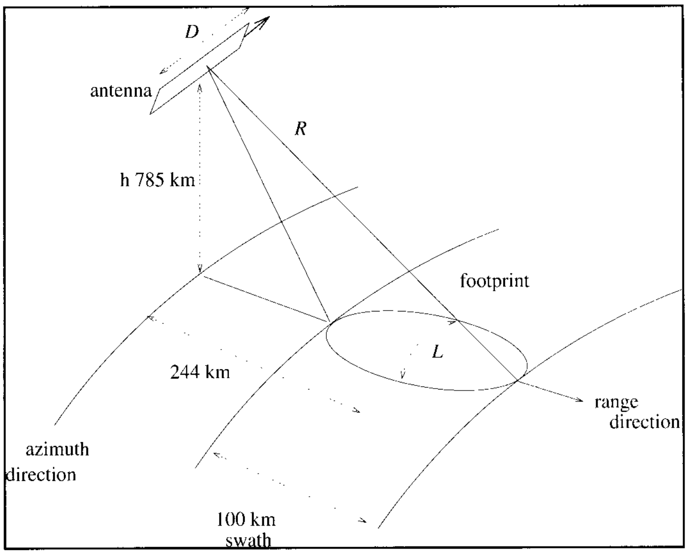

Figure 2: Ground pattern of SAR

In imaging mode the SAR provides high-resolution two-dimensional images with a spatial resolution of 26 m in range (across track) and between 6 m to 30 m in azimuth (along track). Image data are acquired for a maximum duration of approximately 12 minutes per orbit, and data are transmitted to ground receiving stations in line of sight. The duration of image-data acquistion is determined by the number of ground receiving stations in line-of-sight of the satellite.

The rectangular antenna of the SAR is aligned with respect to the satellite's line of flight in such a way as to direct a narrow beam sideways and downwards onto the Earth's surface (Figure 2). This yields strips of high-resolution imagery about 100 km in width (cross track direction). Imagery is built up from time delay and strength of the returned signals, which depend primarily on the roughness and dielectric properties of the surface and its range from the satellite.

Some of the key characteristics of the ERS-1 SAR are listed in Table 2.

2.2 Imaging principles

As the incidence angle of a SAR is oblique (23° for ERS-1 SAR) to the local mean angle of the ocean surface, there is almost no direct specular reflection except at very high sea states. It is therefore assumed that at first approximation Bragg resonance between the radar and ocean waves is the primary mechanism for backscattering radar pulses [42]. The Bragg equation is as follows:

$$\lambda_s = \frac{\lambda_r}{2 \sin \theta} \tag{1}$$

Table 2: Characteristics of the ERS-1 SAR system

Parameter	*Values*
Satellite altitude	(nominal) 785 km
Radar frequency	5.3 GHz$\pm$0.2 MHz
Radar wavelength	(C-band), 0.056 m
System bandwidth	15.55$\pm$0.01 MHz
Spatial resolution	along track $\leq$30 m; across-track $\leq$26.3 m
Radiometric resolution	$\leq$2.5 dB at $\sigma^0 = -18$ dB
Peak sidelobe ratio	along track $\geq$20 dB, across track $\geq$18 dB
Dynamic range	$\leq$25 dB
Swath width	80.4 km nominal, 102.5 km telemetered
Localisation accuracy	along track $\leq$1 km; across-track $\leq$0.9 km
Antenna dimensions	10 m long, 1 m wide
Incidence angle	23° from vertical at mid swath
Polarisation	linear vertical, transmit and receive
Maximum operation time	12 minutes per orbit
Transmitted pulse length	64 ns (compressed)
Pulse frequency repetition	299 μs
Transmitted peak power	4.8 kW
Down load rate	105 Mbit/s

where λ_r is the radar wavelength, λ_s is the sea surface wavelength and θ is the local angle of incidence. The short Bragg-scale waves form in response to wind stress. If the sea surface is rippled by a light breeze and no long waves are present, the radar backscatter is due to the component of the wave spectrum which resonates with the radar wavelength. The threshold wind-speed value for the C-band waves is estimated by Donelan and Pierson [7] to be about 3.25 m s^{-1} at a height of 10 m above the surface. Nominally, the crest of the Bragg resonant wave is at right angles to the range direction. For surface waves with crests at an angle ϕ to the radar line-of-sight (see Figure 4), the Bragg scattering criterion is:

$$\lambda_s' = \frac{\lambda_r \sin \phi}{2 \sin \theta} = \lambda_s \sin \phi \qquad (2)$$

where λ'_s is the wavelength of the surface waves propagating at angle ϕ to the radar line-of-sight.

Figure 3 (left): The Bragg relationship between radar incidence angle and surface wavelength

Figure 4 (right): Bragg resonant relationship when wave crests are at an angle ϕ to the line of sight

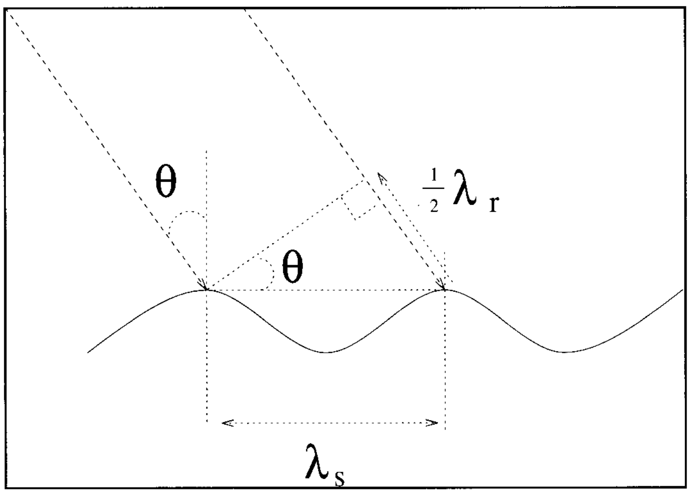

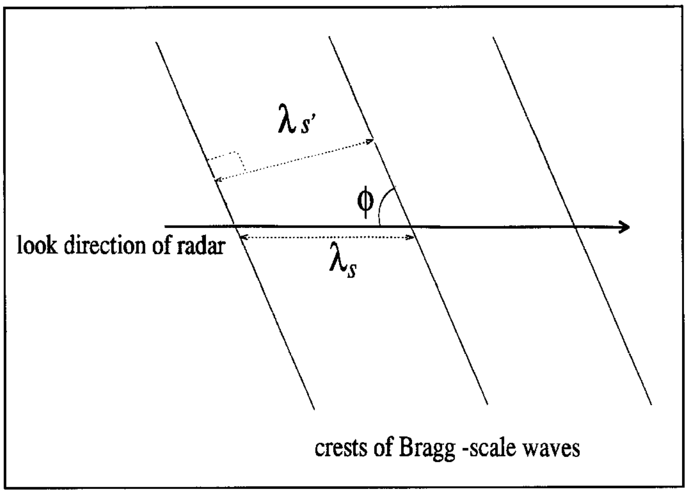

The SAR directly images the spatial distribution of the Bragg-scale waves. The spatial distribution may be affected by longer gravity waves, through tilt modulation, hydrodynamic modulation and velocity bunching [14]. Moreover, variable wind speed, changes in stratification in the atmospheric boundary layer, and variable currents associated with upper ocean circulation features such as fronts, eddies, internal waves and bottom topography also influence the Bragg waves.

Range resolution

The range resolution of a pulsed radar system is limited fundamentally by the bandwidth of the transmitted pulse (the wider the bandwidth the better the range resolution). Although a large bandwidth can be achieved by a short-duration pulse, the shorter the pulse the poorer the signal-to-noise ratio and hence the radiometric resolution will be. To preserve radiometric resolution, a long transmit pulse is desirable, and this is achieved by phase coding the transmit pulse with a linear chirp (a linear frequency modulation). Range resolution may be determined by means of the pulse travel time, the range resolution corresponding to the minimum distance between two points on the Earth's surface which are separable. If two points are separated by a distance X_r, their respective echoes will be separated by a time difference:

$$\Delta t = \frac{2X_r}{c} \sin\theta \tag{3}$$

where c is the speed of light. In general the pulse bandwidth is defined as $B=1/\tau$, where τ is the pulse length. Thus the range resolution may be given by

$$2\frac{X_r}{c} \sin\theta = \tau \tag{4}$$

$$\circ \; X_r = \frac{c\tau}{2\sin\theta} = \frac{c}{2B\sin\theta} \tag{5}$$

Thus a signal of bandwidth B=15.55 MHz (ERS-1 SAR) will provide a range resolution equal to 24.8 m for a centre swath incidence angle θ equal to 23°.

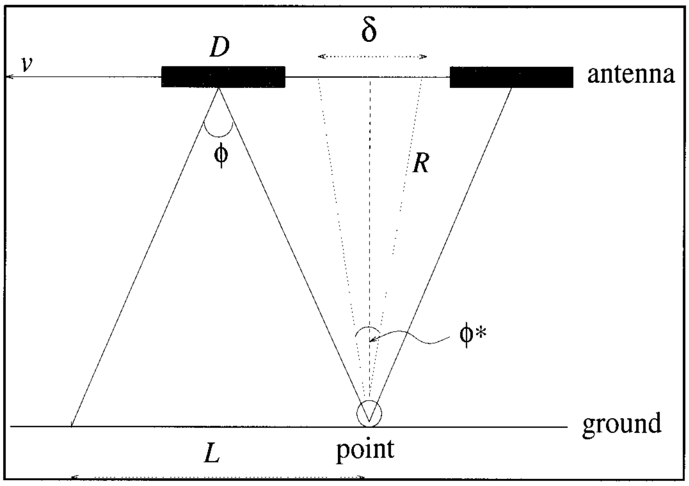

Figure 5: A section-linear trajectory idealisation of the ERS-1 SAR. *D* is the radar aperture length, *R* the slant range, *L* is the ground coverage — a function of φ the beam width and φ* the returned beamwidth — δ is the resolution

Azimuth resolution

SAR uses the forward motion of the satellite to synthesise a longer antenna which enhances the azimuthal resolution. The azimuth resolution is achieved by recording the phase as well as the amplitude of the echoes along the flight path. A point on the Earth's surface is illuminated for a finite time period T (Figure 5), where

$$T = \frac{L}{v} \tag{6}$$

in which v is the velocity of the platform and L is the along-track dimension of the footprint. The azimuthal beamwidth is $\phi \approx \lambda/D$, so we can write:

$$L = vT = R\frac{\lambda}{D} = R\phi \tag{7}$$

for a narrow beam. Here R is the distance from the antenna to the Earth's surface (the slant range), D is the length of the aperture and λ is the radar wavelength.

In order to calculate the azimuth resolution, we may consider the target as an antenna (for simplicity). It remains within the illuminated beam for the time $T=L/v$. Hence, we introduce an 'antenna' length L, leading to an azimuth beamwidth resolution:

$$\phi^* = \frac{\lambda}{L} = \frac{\lambda}{R(\lambda/D)} = \frac{D}{R} \tag{8}$$

Thus we obtain for the resolution

$$\delta = R\phi^* = R\frac{D}{R} \tag{9}$$

$$\delta \simeq D \tag{10}$$

In order to maintain a minimum 3 dB (50%) as the lower limit in both transmitted and received pulses the effective azimuth resolution approximates to $\delta \simeq D/2$.

The azimuth resolution is inversely proportional to the real aperture length and this is independent of the range and the platform altitude, which is a unique advantage of the SAR method.

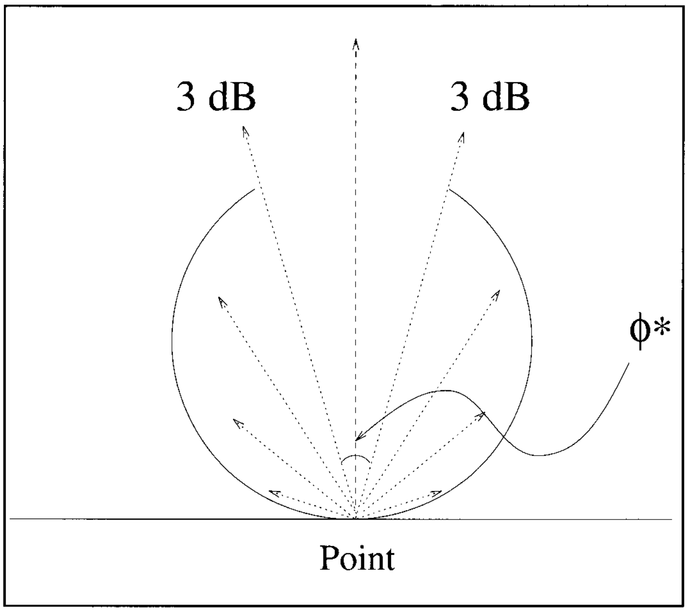

Figure 6: Ground pattern of SAR wave scattering

3. Classes of SAR images

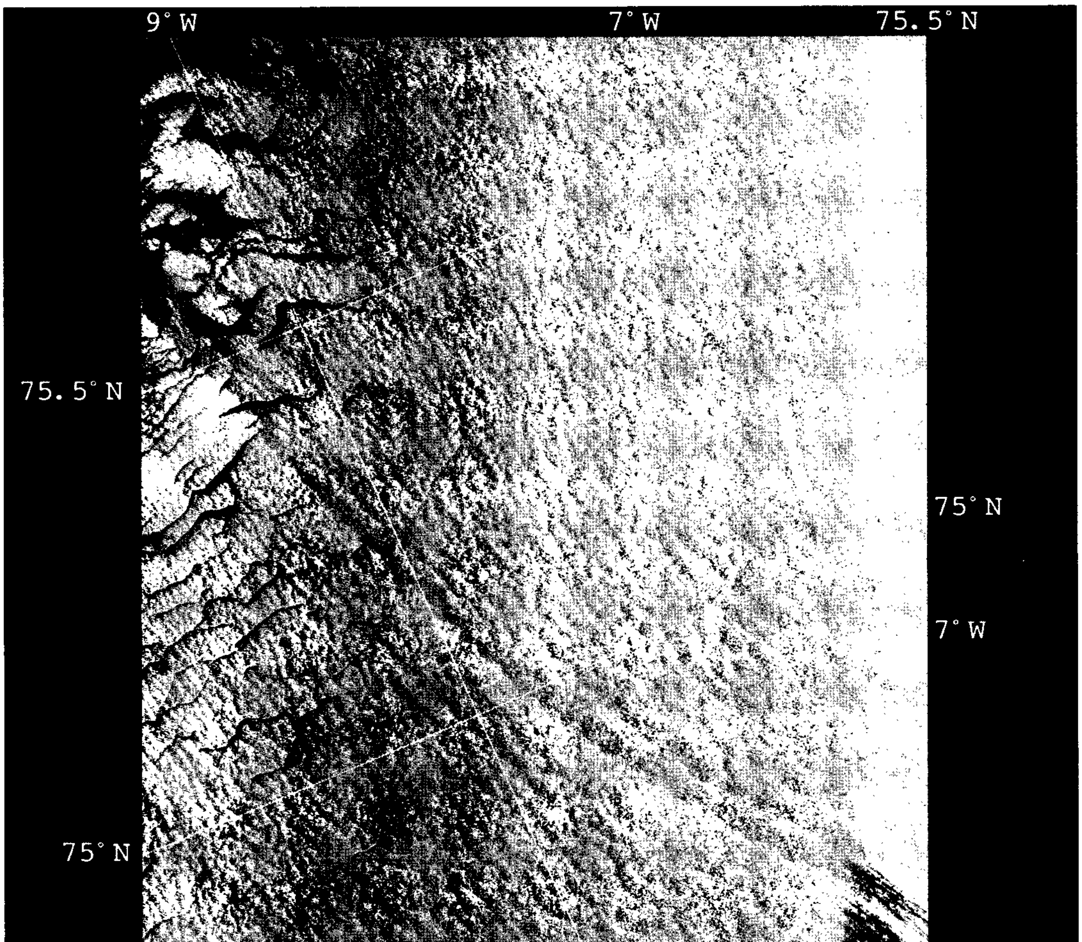

16-01-92

Figure 7: NOAA AVHRR infrared image

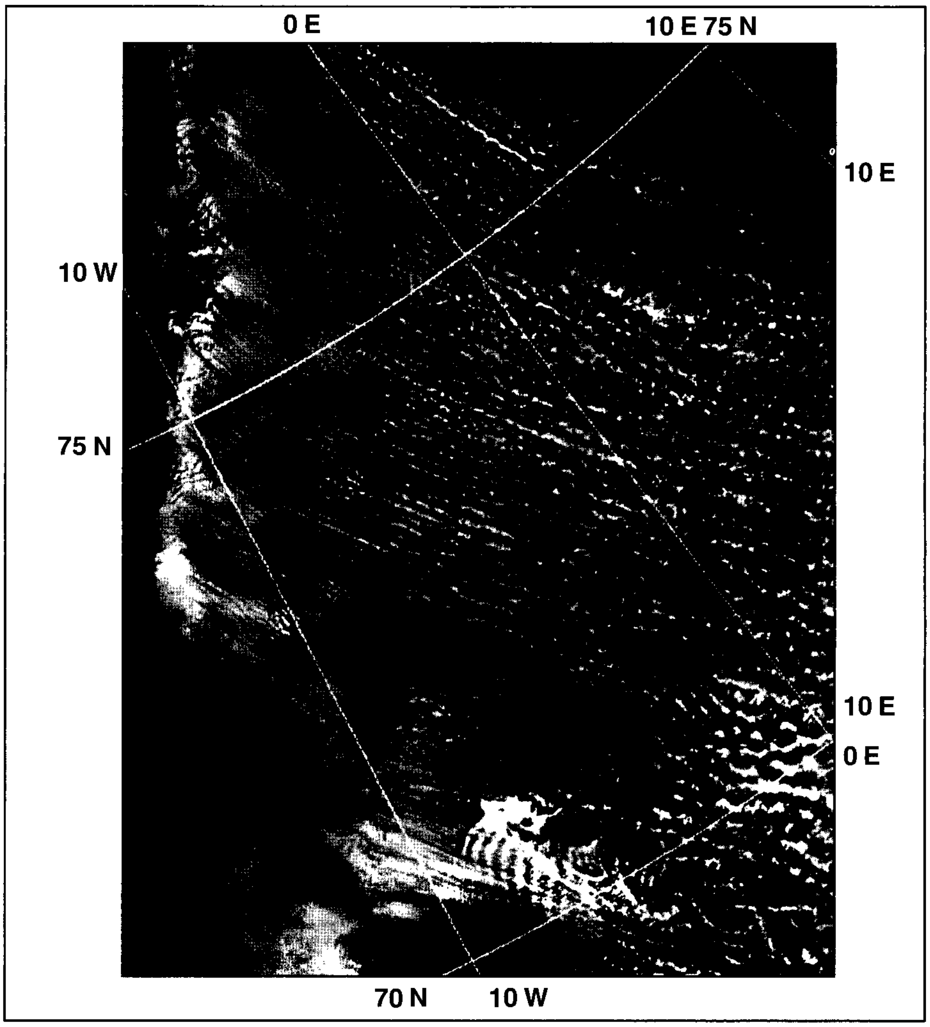

3.1 Atmospheric boundary layer

3.1.1 Wind rolls

This case from 16 January 1992 offers the possibility of comparing boundary-layer cloud structure and surface-roughness patterns in a synergistic fashion. The image in Figure 7, made with the NOAA advanced very-high-resolution radiometer (AVHRR), and the ERS-1 SAR image introducing this section were obtained within about 20 minutes of each other off the edge of the ice in the East Greenland Current. The SAR image represents an area about 100 km × 100 km, while the NOAA image covers the region between Greeenland, northern Norway and Svalbard. The rectangular region of SAR coverage is indicated in the NOAA image. The NOAA AVHRR image depicts the cloud structure evolving downwind from the ice edge in the Greenland Sea. Such structures are reported to be associated with horizontal roll vortices in the atmospheric planetary boundary layer [26]. In the vicinity of the ice edge, the rolls are not seen, while a gradual increase in the spacing of the horizontal rolls with distance downwind is observed. This is explained by the growing boundary layer height, which eventually reaches a depth where the available energy decays and the organisation of the roll structure breaks down. The mean wave number is estimated to be 1.5 km^{-1}, which is equivalent to a roll spacing of about 5 km. The spacing is reported to range from two to four times the planetary boundary-layer depth [26]. In this case, the implication is that the boundary layer ranges from 1.25 to 2.50 km in height.

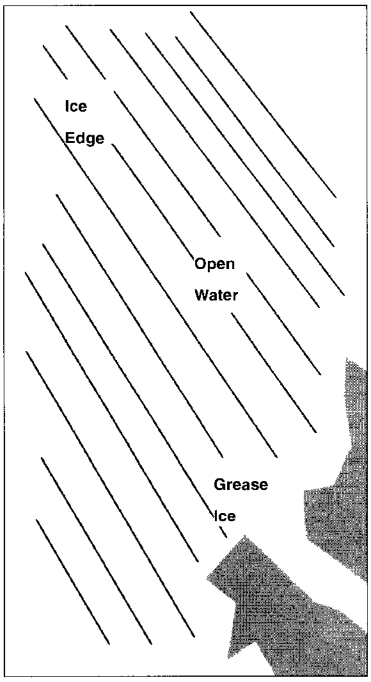

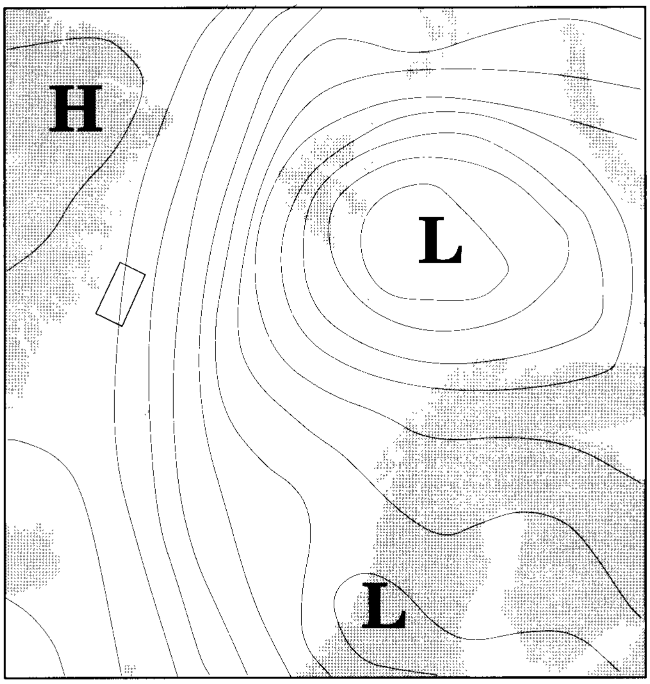

Figure 8: Interpreted image and weather map

Rolls are frequently observed in IR images downwind of the ice edge and are assumed to be due to cold air flowing over warmer water, leading to unstable stratification in the boundary laver with significant moisture flux. They are also reported to be of substantial importance for the heat flux [26]. The SAR image reveals the corresponding surface roughness in the open water off the ice edge. One can clearly see a perturbed, streak-like pattern with a mean orientation aligned with the direction of the roll vortices. The estimated wave number ranges from 1.5 to 2.0 km^{-1}, which is in agreement with the estimate based on the IR image. The surface waves that lead to this characteristic pattern are formed primarily in response to variations in the surface wind introduced by the horizontal roll vortices. In turn, atmospheric phenomena that induce a varying sea-surface-wind field, and hence wind stress, are detectable by the SAR. Several bands of dark backscatter are also observed. We interpret these to be areas of new ice, which damps out the short gravity waves [33].

According to LeMone [26] and Alpers and Brümmer [1], we can compute surface-wind-speed fluctuations induced in the mean wind direction by the convective motion associated with the horizontal roll vortices. On the basis of the CMOD4 scatterometer wind-retrieval model [35], we obtain a wind speed variation of about $\pm 1\ m\,s^{-1}$.

The analysed weather map reveals that the pattern is aligned almost along the isobars and consequently in the geostrophic wind direction. The wind speed is reported to be 7 to 8 $m\,s^{-1}$ from a nearby weather station on Jan Mayen Island, while the off-ice direction implies that cold (−16°C), dry air is advected over warmer water having a temperature ranging from −1.5 to +3.0°C. This is turn leads to strong unstable stratification.

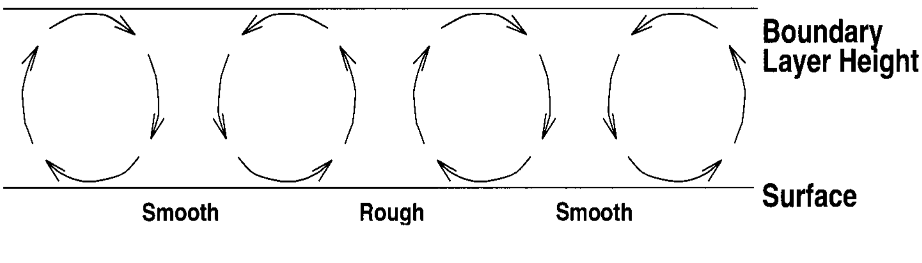

Figure 9: Schematic illustration of the atmospheric rolls in the vertical plane and the resulting effect on the surface

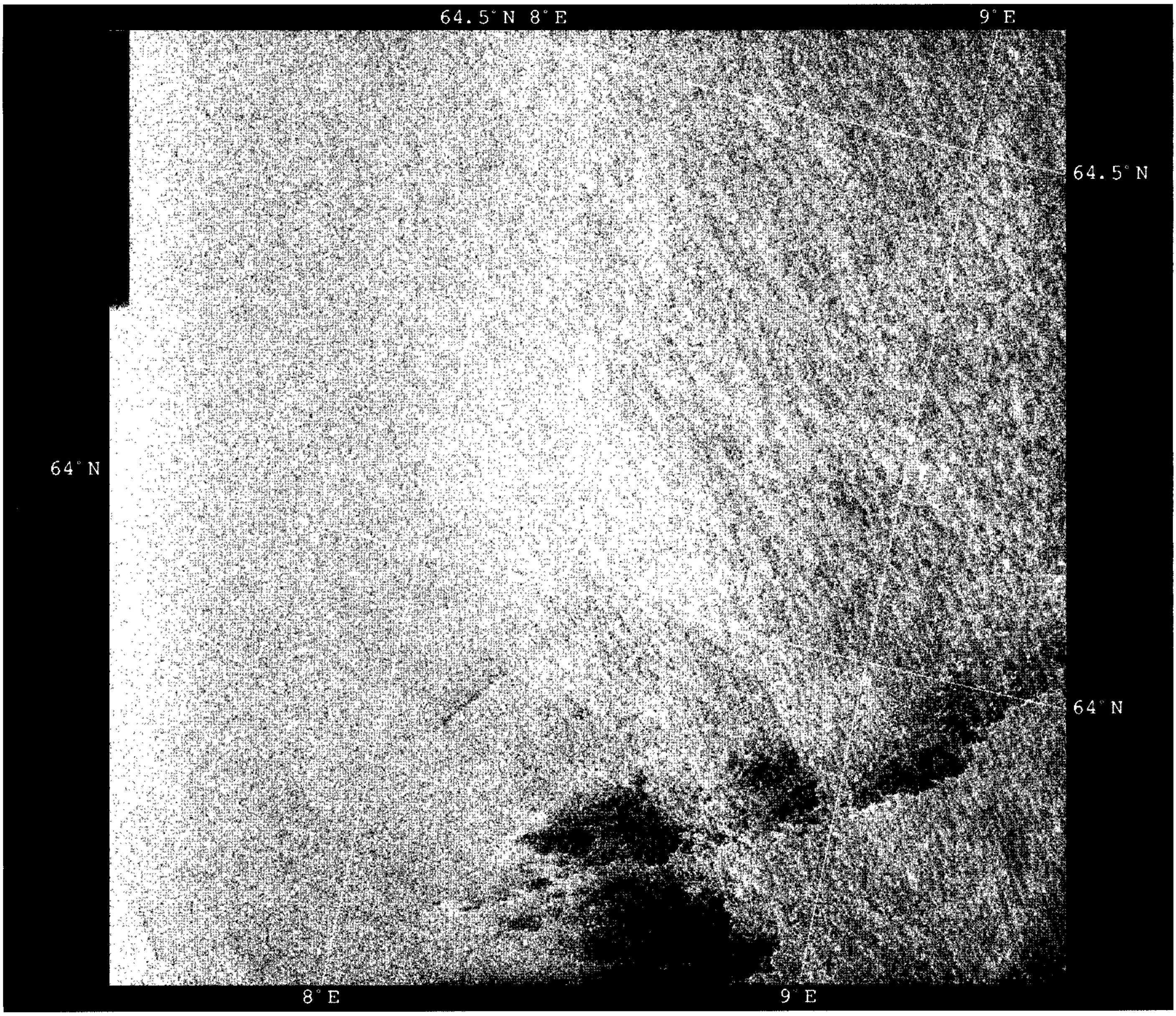

10-11-91

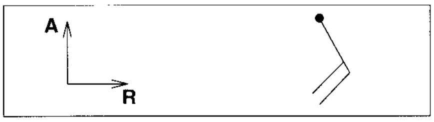

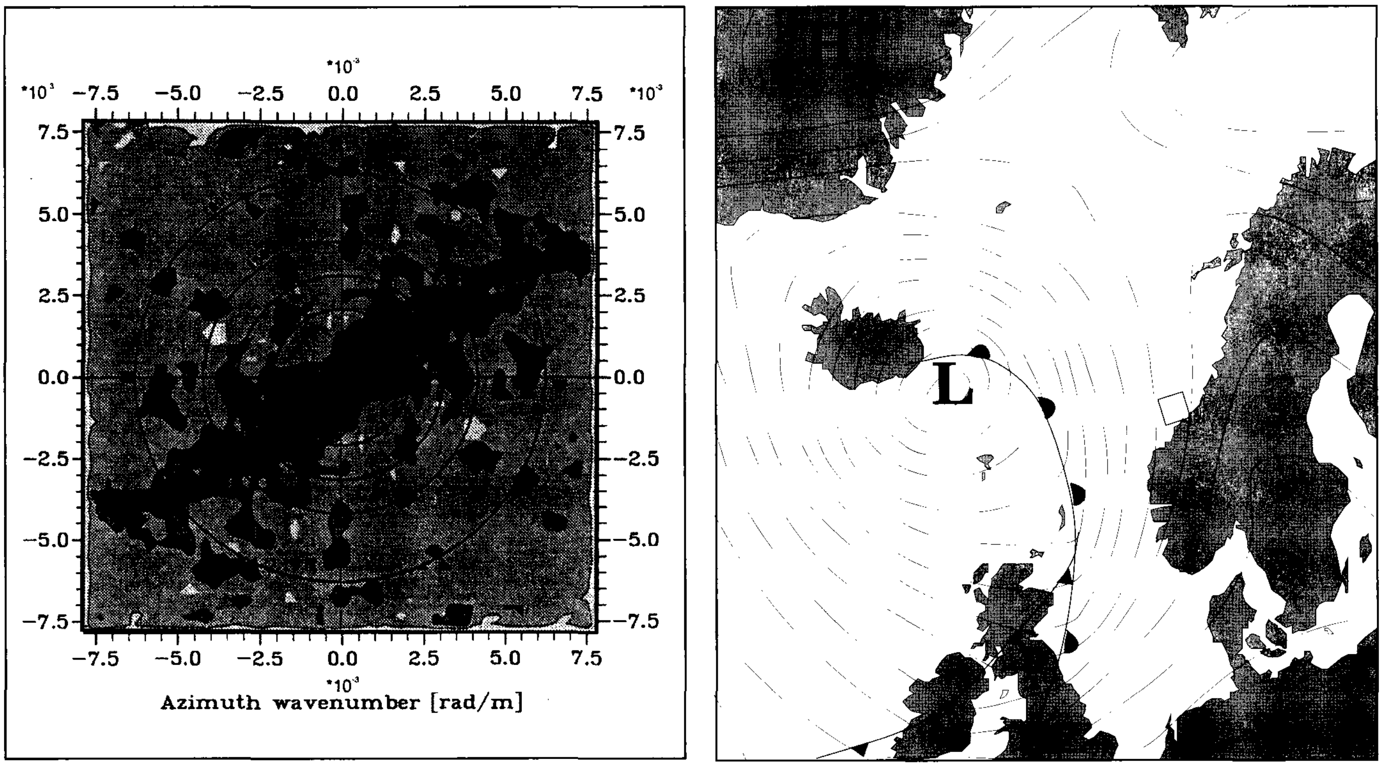

Figure 10: Image spectrum and weather map

The wind direction can be estimated in SAR images by examination of the low spatial frequency in the image spectrum. As the presence of rolls in the atmospheric boundary layer can cause streaks to appear in the SAR images, the direction of these can be used to estimate the wind direction with an ambiguity of 180°. Figure 10, left, shows a low-frequency wave-number spectrum derived from the SAR image on the opposite page, which was made on 10 November 1991. The energy in the spectrum is concentrated in a SW-NE direction, and this will be perpendicular to the streaks and hence to the wind direction. Taking into account the image azimuth angle, the derived wind direction (with the 180° ambiguity) is shown to the left in Figure 11. An *in situ* measurement (approx. 200 km SW of the image centre) of the wind direction is indicated to the right.

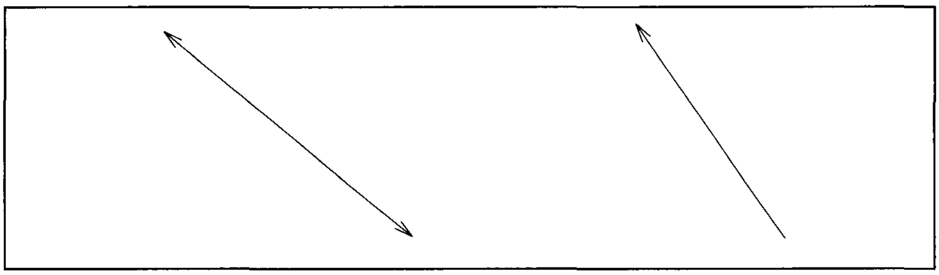

Figure 11: Wind direction computed from SAR image (left) compared with the measured wind direction (right)

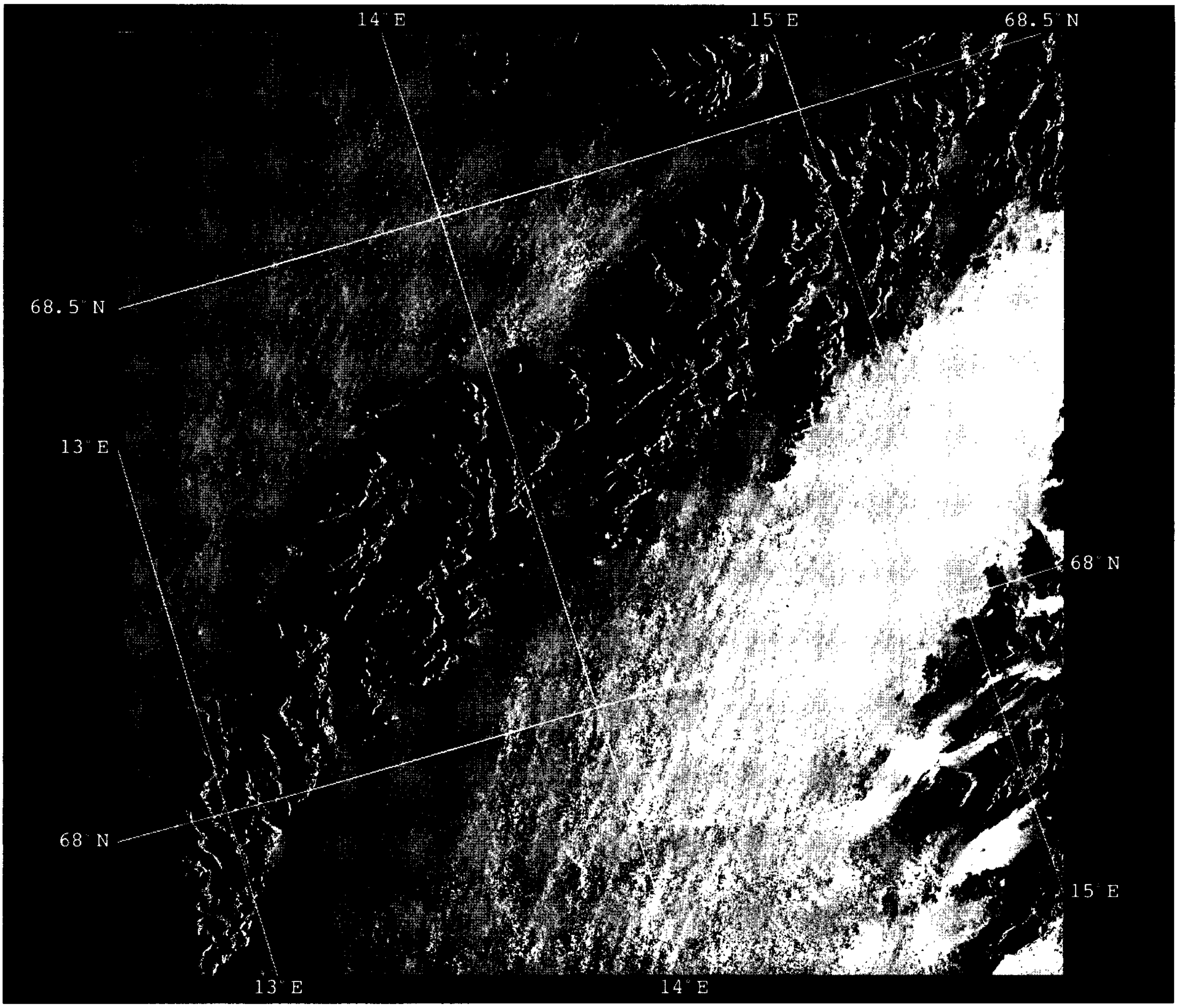
14° E
15° E
68.5° N
68.5° N
13° E
68° N
68° N
15° E
13° E
14° E

19-10-93

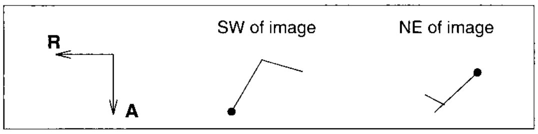
R
A
SW of image
NE of image

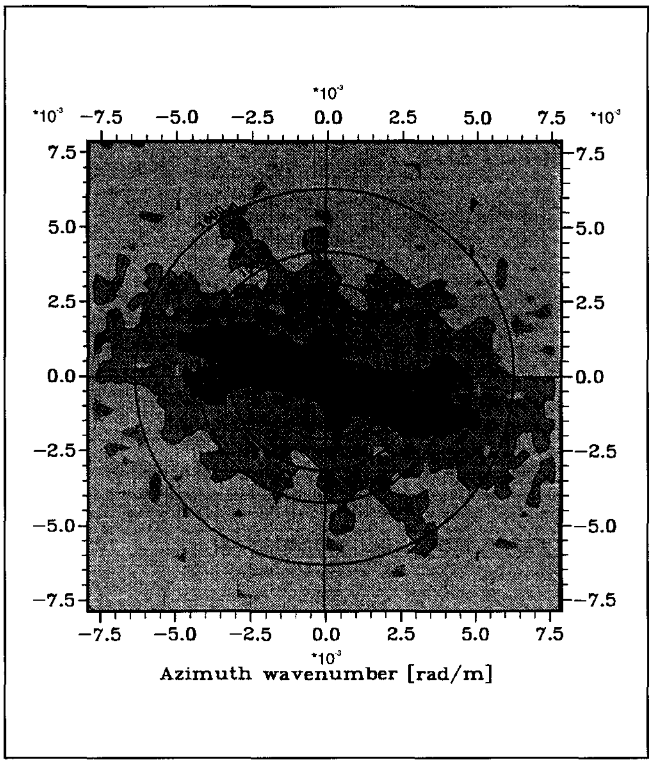

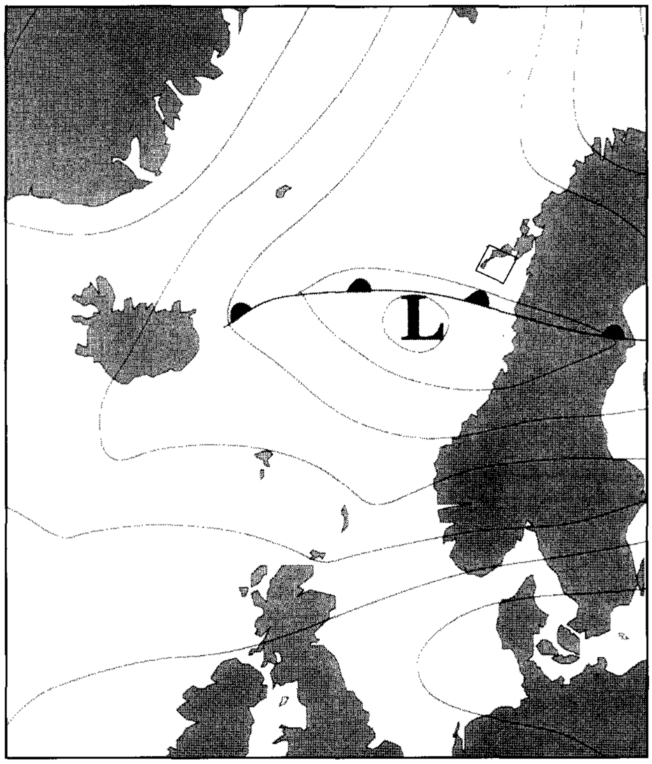

Figure 12: Image spectrum and weather map

Another image with streak pattern due to horizontal roll vortices is the one shown here from 19 October 1993. The measured wind pattern in this area just NE of the low-pressure centre is very inhomogeneous. This is shown in Figure 13, where the left-hand arrow indicates the wind direction measured 100 km SW of the image centre, while the right-hand arrow indicates the wind 50 km NE of the centre. The middle arrow shows the wind direction derived from the SAR image. The wind speed is low, about 5 knots.

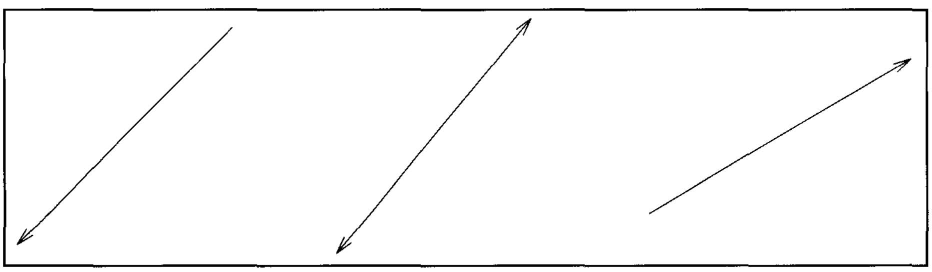

Figure 13: Left: Measured wind direction 100 km SW of the image centre. Middle: wind direction derived from SAR image. Right: Wind direction measured 50 km NE of the image centre

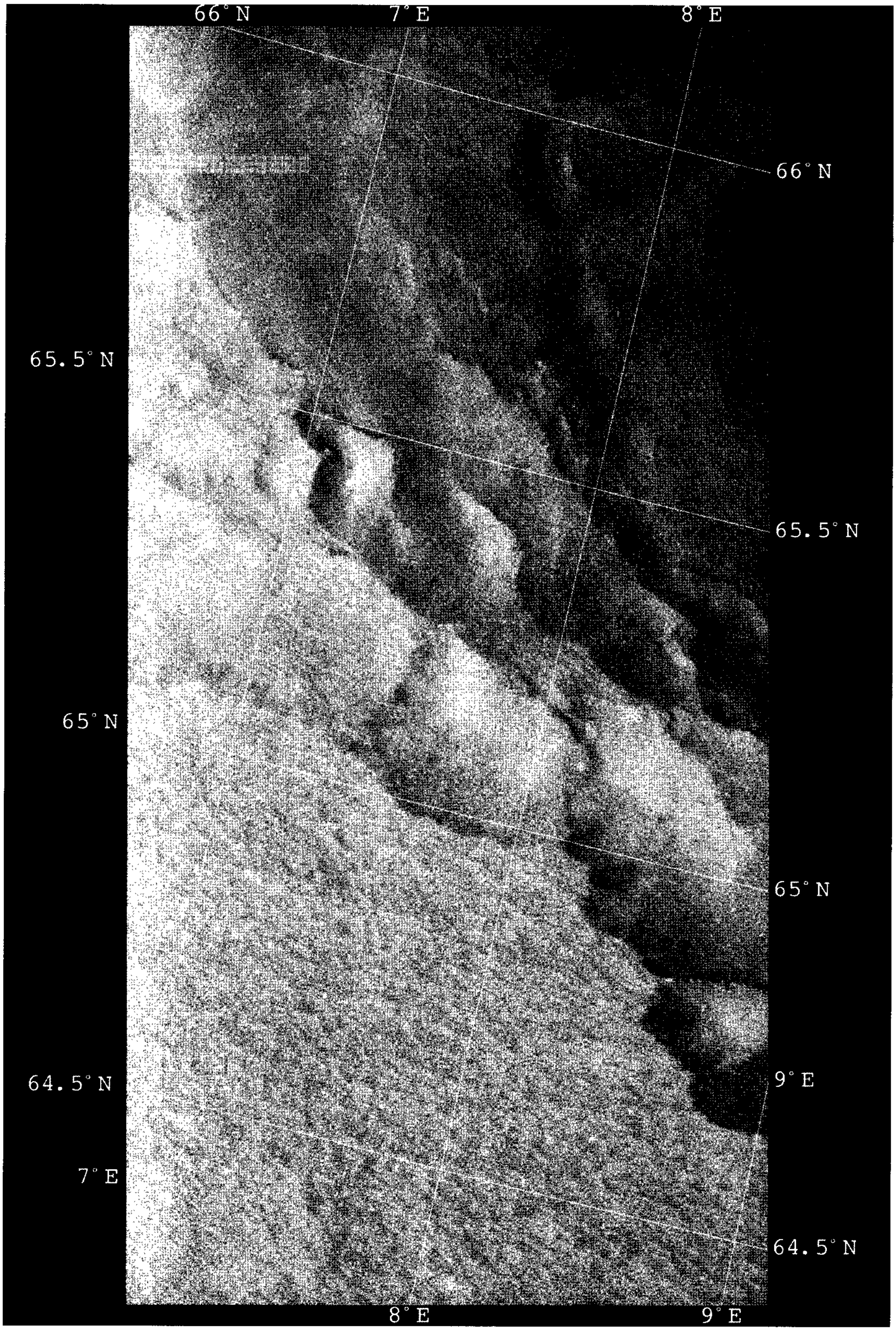

16-11-91

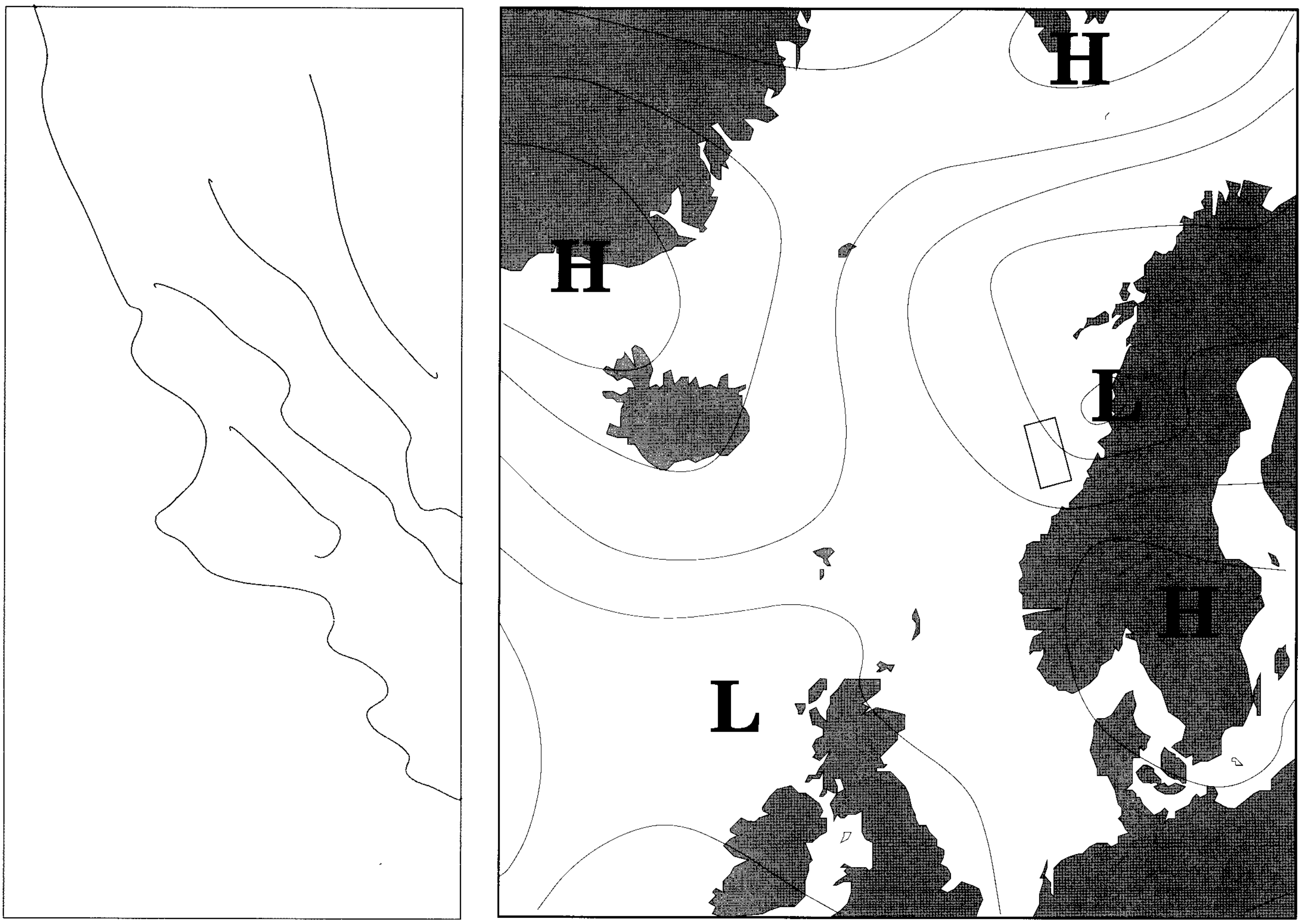

Figure 14: Interpreted image and weather map

3.1.2 Wind fronts

The SAR images the capillary waves which are formed primarily in response to the wind over the ocean. The higher the wind speed, and the more directly towards the antenna the wind blows, the brighter the image. This is the basis of the empirical equation, CMOD4 [35], which relates wind speed and wind direction to ς^0.

Figure 15: Backscatter cross section through the wind front. The position of the profile is marked by the arrow in the interpretation figure

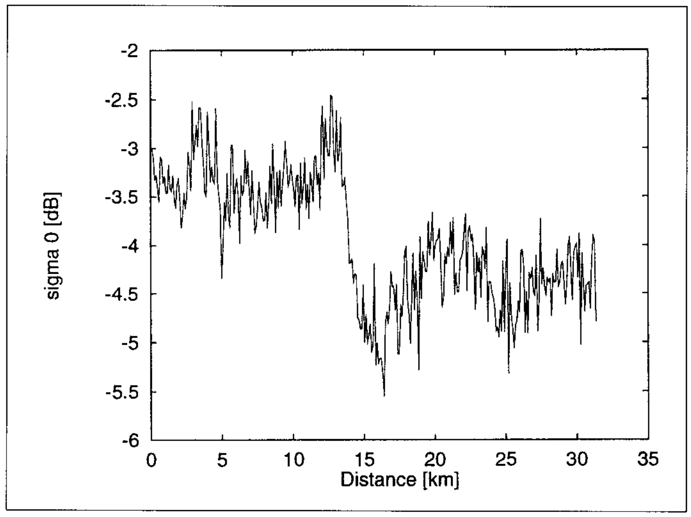

The first image in this section, obtained on 16 November 1991, shows the characteristic cross-sectional signature of a wind front [22]. The profile across the front is shown in Figure 15. Comparison with the analysed wind fields from this day shows good agreement. The centre of the low-pressure area is located northeast of the SAR image, as shown in Figure 14, and the wind changes gradually from 15 m s^{-1} to 10 m s^{-1} across the SAR swath, while the SAR image shows that the wind speed undergoes a series of steplike decreases across the scene from near to far range.

In the image, a northwesterly wind direction in the high wind speed region can be identified from the series of streaks almost parallel to the front, in qualitative agreement with the weather map. In the weather map, it can also be seen that the isobars, and hence the wind, turn more westerly near the coast.

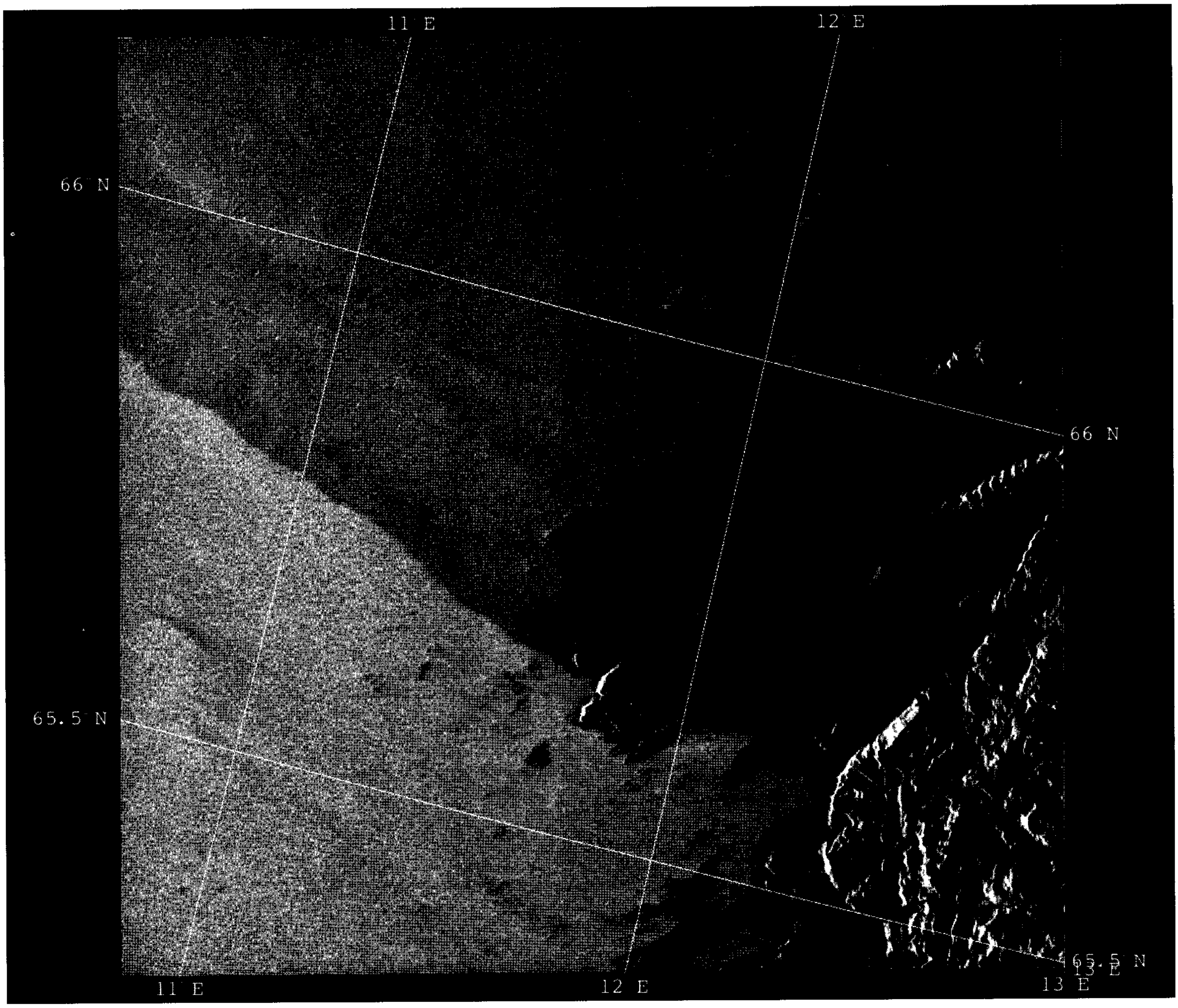

18-10-93

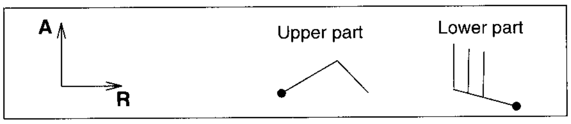

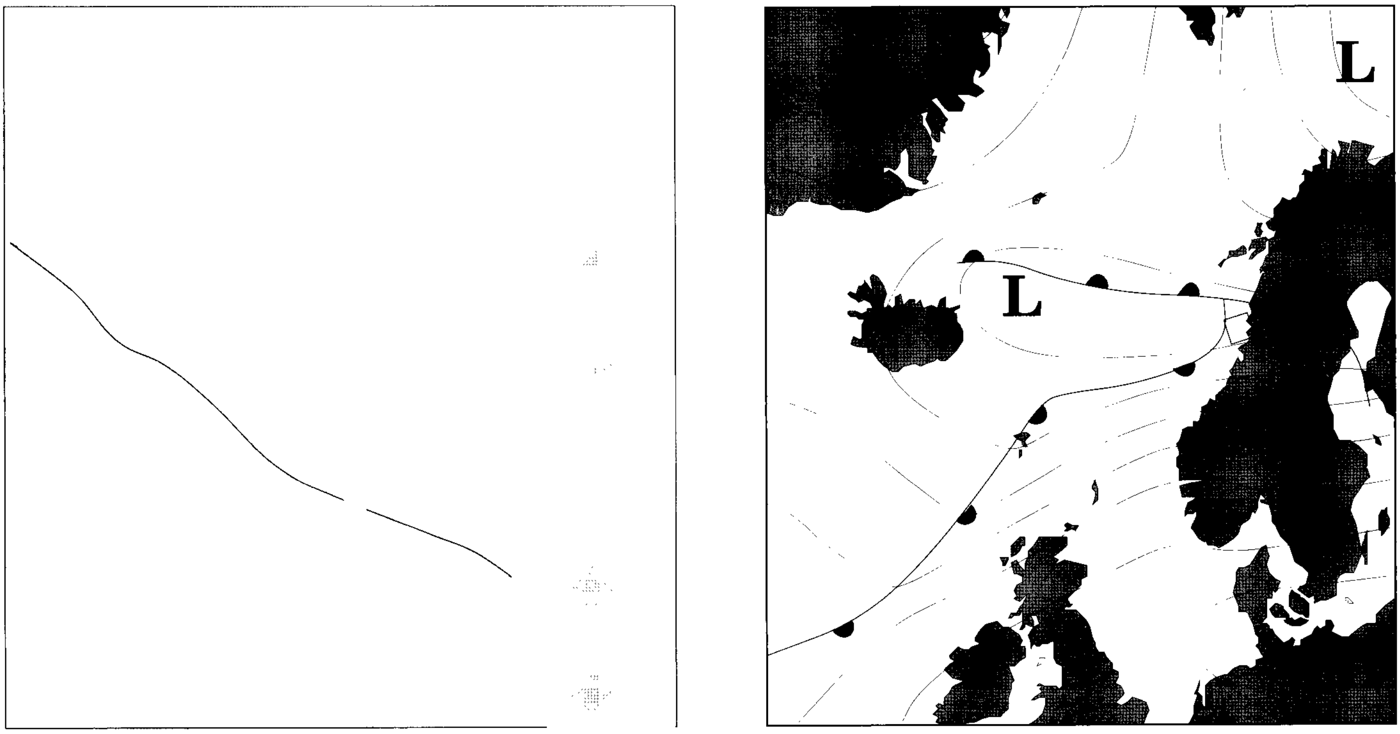

Figure 16: Interpreted image and weather map

The next image, from 18 October 1993, shows a very distinct wind front in the NW-SE direction, marked as the thin line in the interpretation given in Figure 16. The front differs from the previous one in that the border is more abrupt.

The analysed weather map in Figure 16 also shows fronts in the same region. The upper front in the weather map is aligned with the front seen in the SAR image and the offset between the imaged and the analysed front is approximately 100 km. This discrepancy in distance can be explained partly by the uncertainty in positioning the front on the weather map and partly by the time difference of approximately 15 minutes between SAR acquisition and meteorological observations.

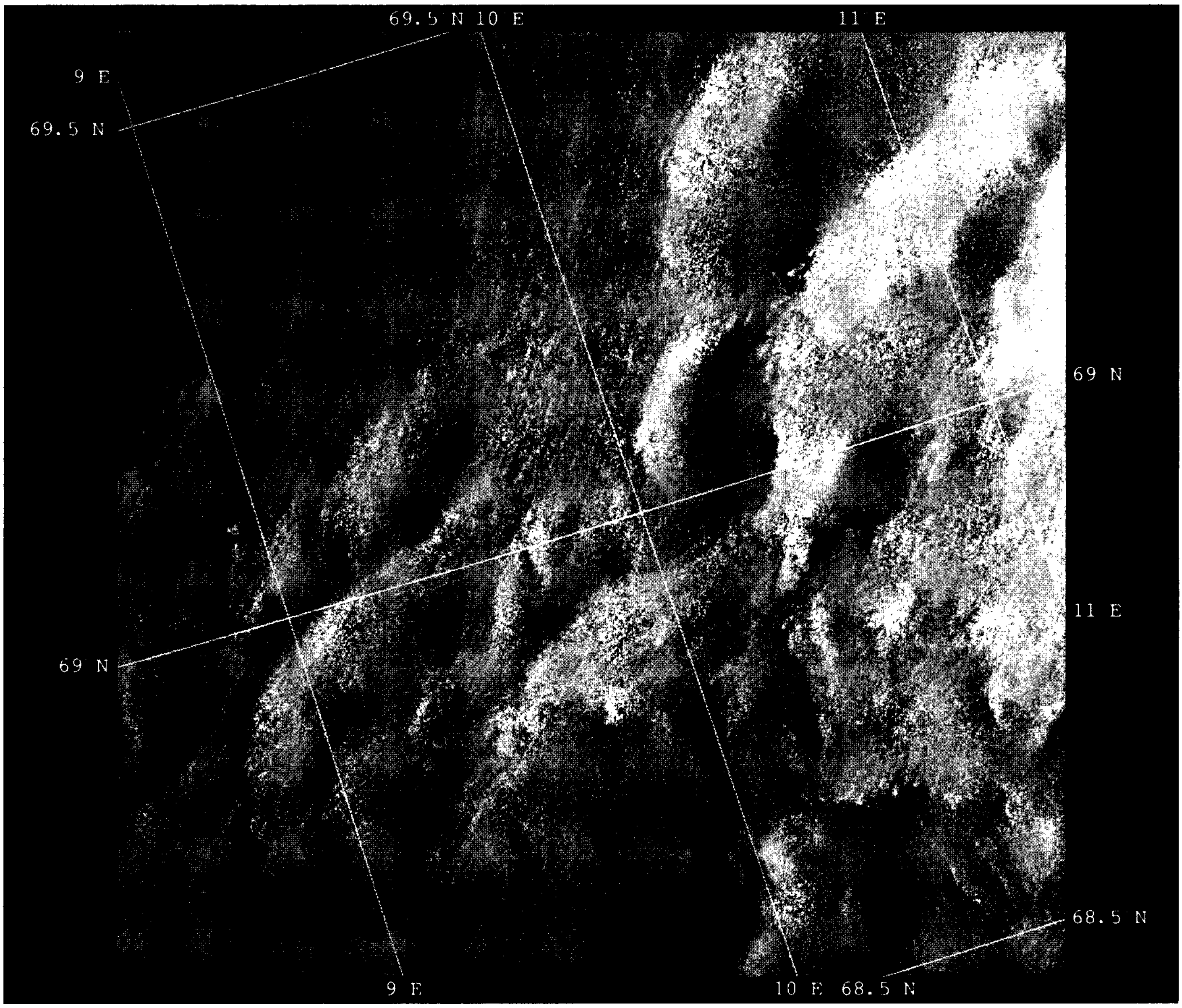

12-10-93

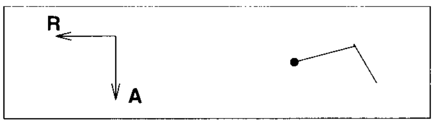

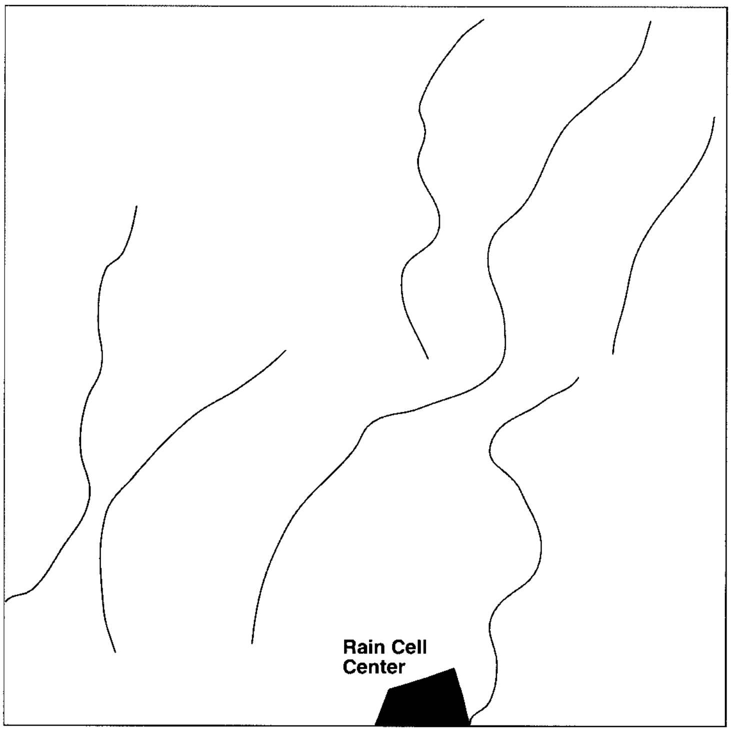

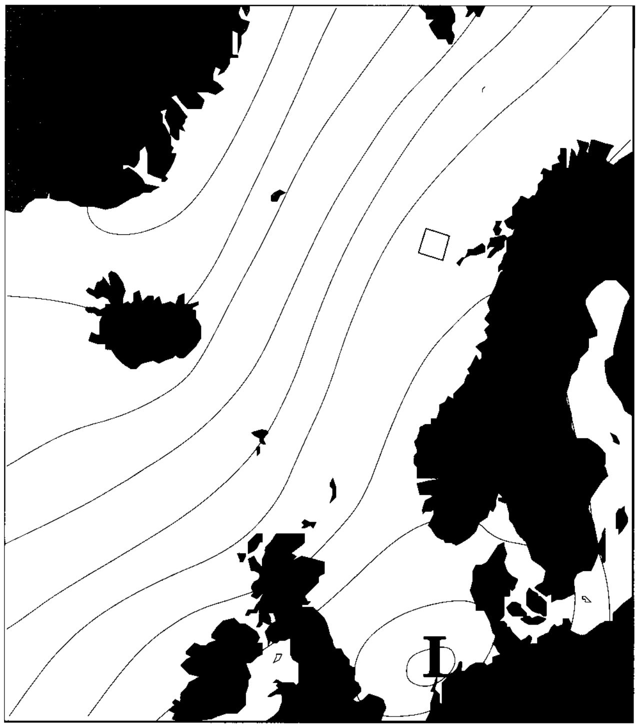

Figure 17: Interpreted image and weather map

The image from 12 October 1993 again shows stepwise changes in wind speed. The measured local wind is 5 m s^{-1} blowing from the east. The individual wind fronts are shown in the interpretation in the left-hand part of Figure 17.

The weather map does not indicate a wind front, but the the pressure gradient to the west of the SAR scene could be the cause of the unstable situation in the image.

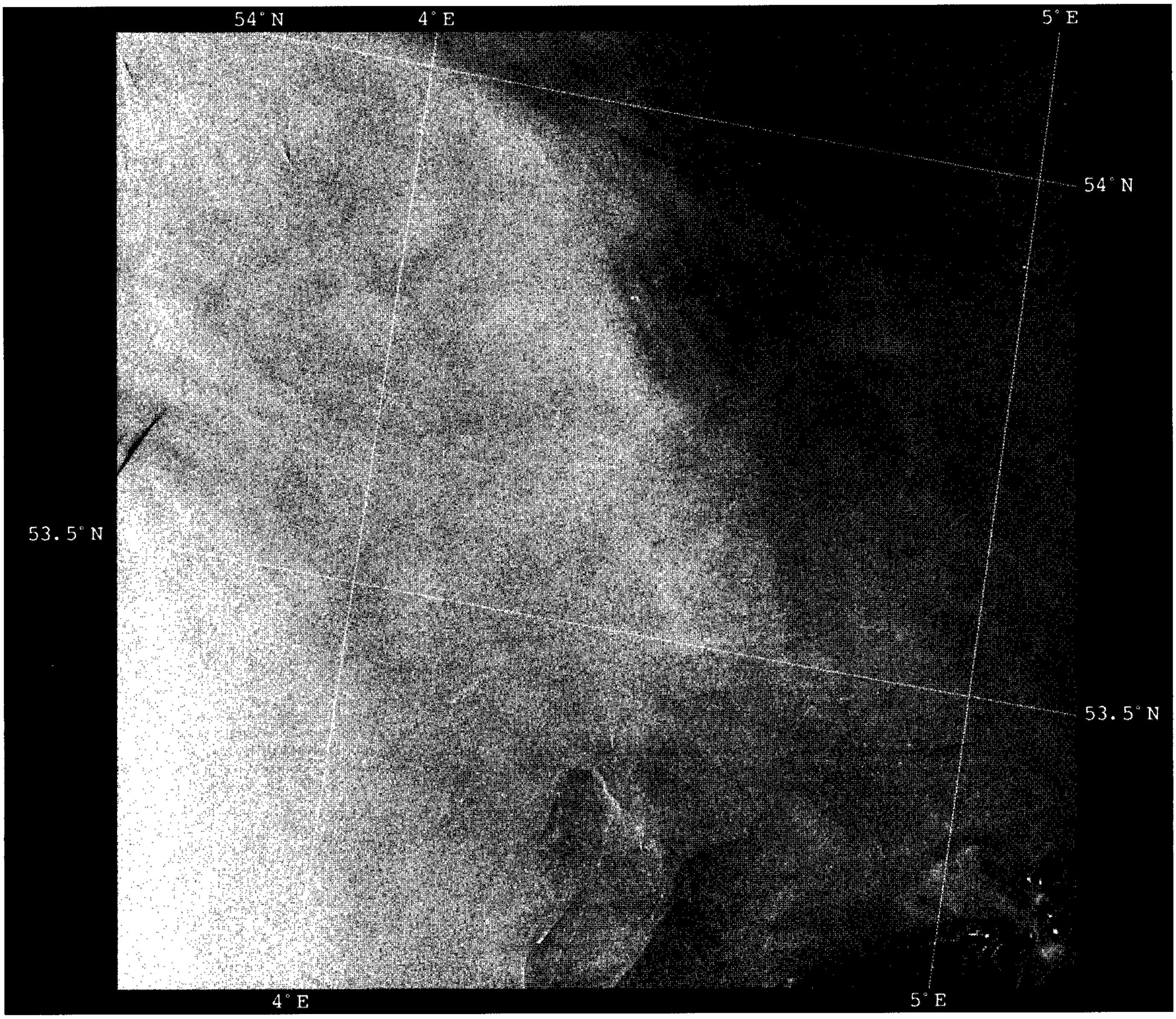

16-07-93

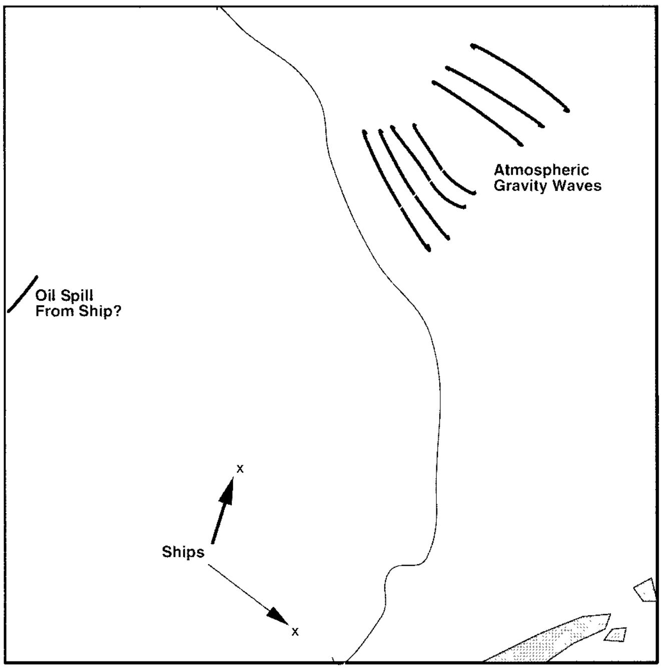

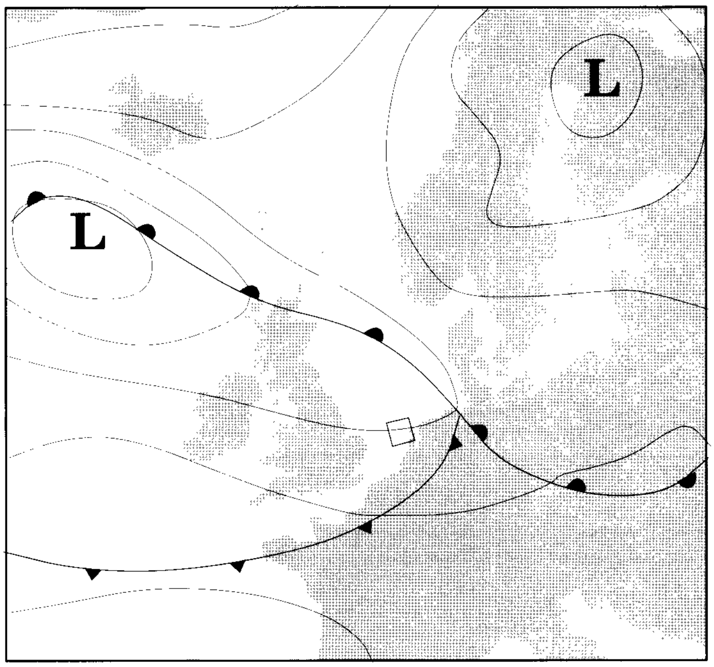

Figure 18: Interpreted image and weather map

3.1.3 Atmospheric gravity waves

The first example, from 16 July 1993, shows a group of atmospheric gravity waves off the coast of The Netherlands which may be associated with a frontal disturbance. In this case, the surface analysis shows the front to the northeast of the image location. The image appears to contain the front, shown by the transition from the light region (high-wind-speed side of the front) to the dark region (low-wind-speed side). The waves were apparently generated by the northeastwardly propagating front, and were themselves propagating towards the northeast. Figure 19 illustrates the variation in radar backscatter associated with the surface wind perturbation of atmospheric gravity waves. The successive troughs are numbered and their wavelengths are estimated to be ≈ 5 km. The position of the wind front apparent in the SAR image is indicated in the profile.

Figure 19: Profile of radar backscatter along the transect highlighted on the interpretation image

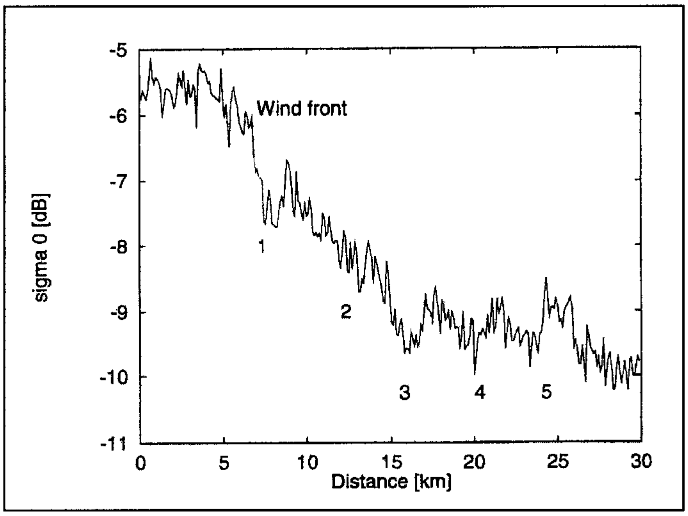

Variations in wind speed at the ocean surface affect the local surface roughness and may, in turn, be detected by means of imaging radars. The variations in wind speed may be associated with wave phenomena in the atmospheric boundary layer. Gravity waves are internal waves for which gravity is the restoring force. They may be associated with temperature inversions; these cause stably stratified layers in the lower troposphere, which serve as waveguides. They may also be associated with wind shear aloft and will generally propagate in the direction of the wind shear. The generation mechanism is often uncertain, but some possible mechanisms are orographic interactions, frontal disturbances or convective instability, to name a few.

Atmospheric gravity waves are commonly seen in ERS-1 SAR images over the open ocean. They have been observed with wavelengths of 1 to 20 km. Unfortunately, only one image of each wave group is available from ERS-1. Consequently, it is impossible to carry out a closed-form model validation, such as

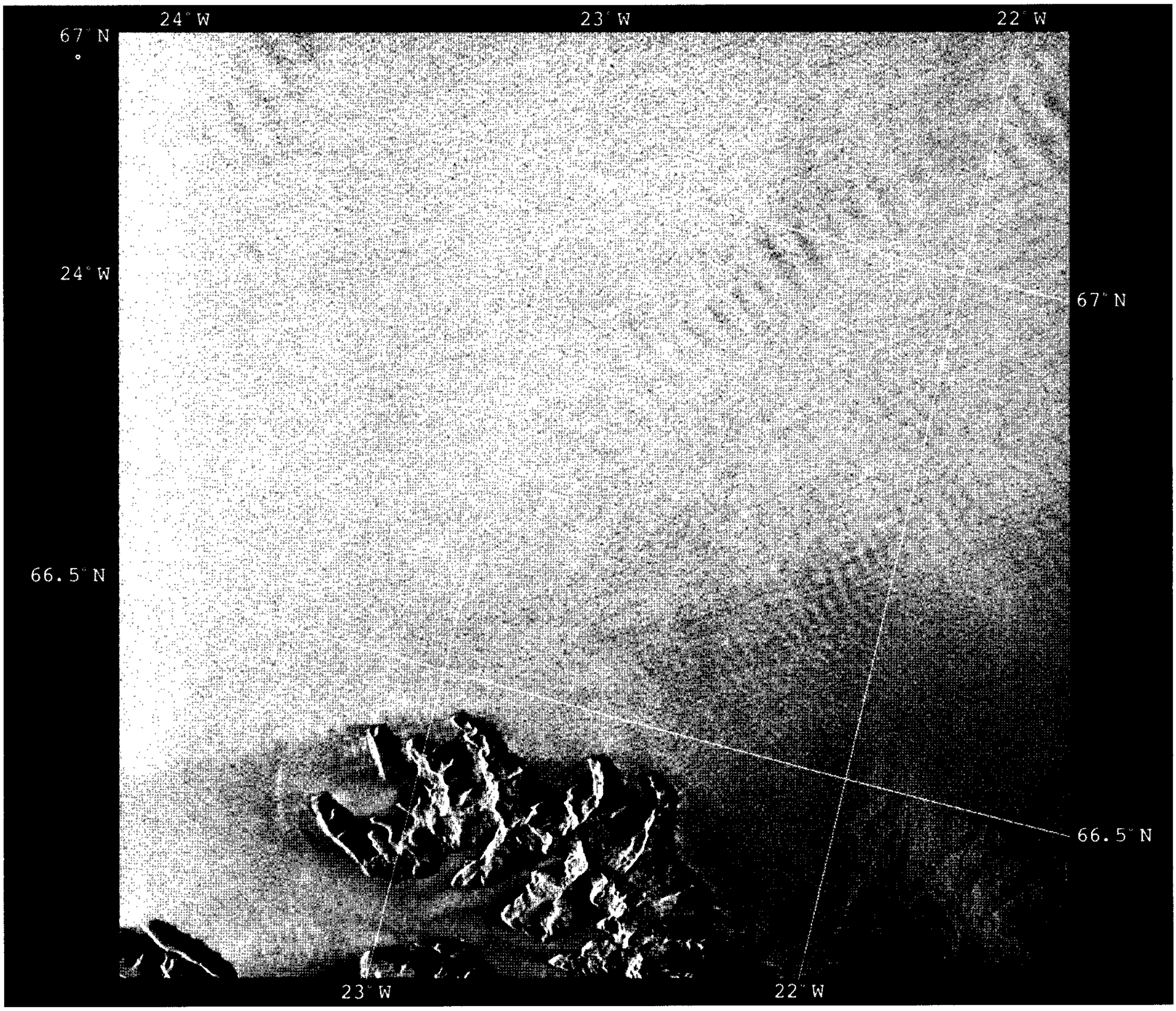

01-10-93

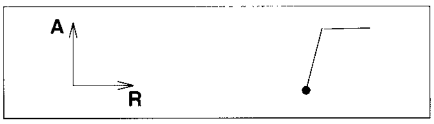

was done with the airborne SAR data from the coast of Canada [37]. In other words, the wave number may be estimated directly from the SAR image, but we do not have any temporal information from which to deduce the wave frequency and eventually the phase speed.

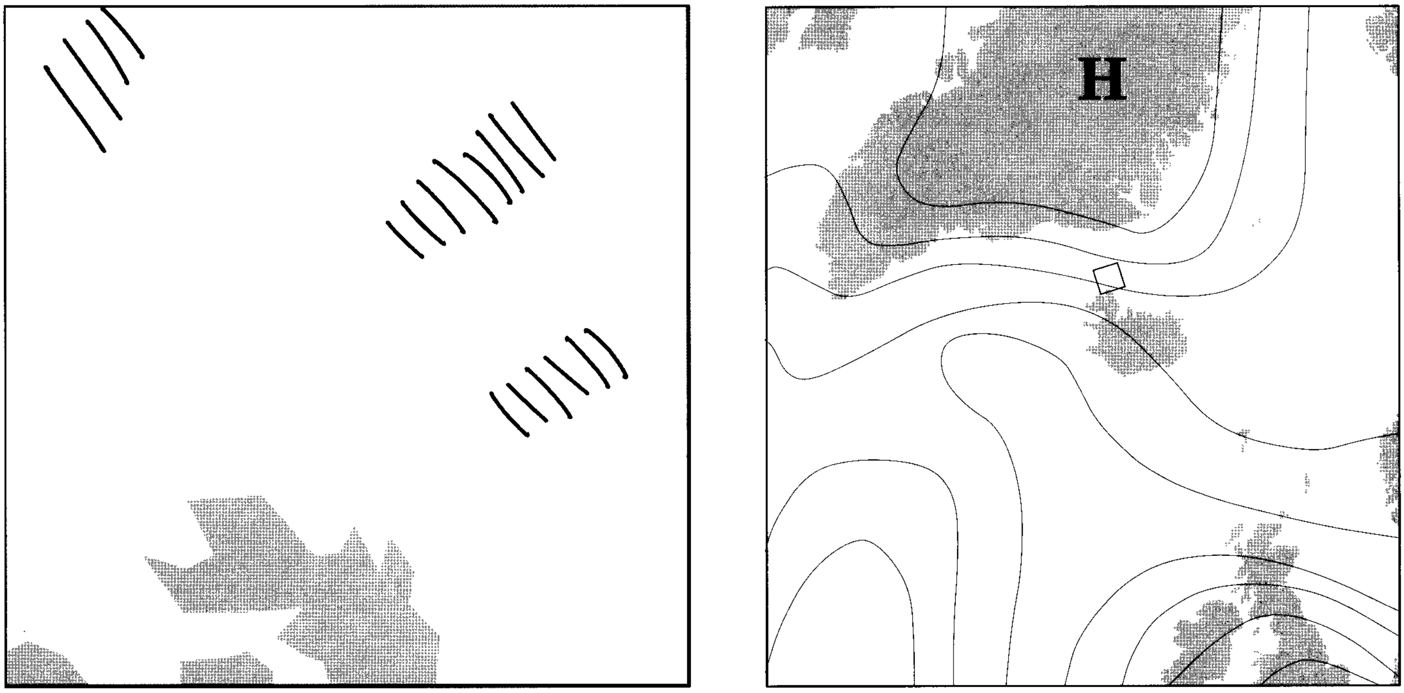

The second example (coast of Iceland) shows three distinct wave groups which were propagating towards the southwest, in the nominal direction of the surface wind velocity. The wave groups each have distinct wavelength scales: 3.8 km for the group near the northwest corner of the image, 3.1 km for the group near the northeast corner of the image, and 2.7 km for the group near the eastern side of the image. In this case, the generation mechanism is unknown. Note that all three wavelength scales could be supported by the same atmospheric conditions.

Figure 20: Interpreted image and weather map

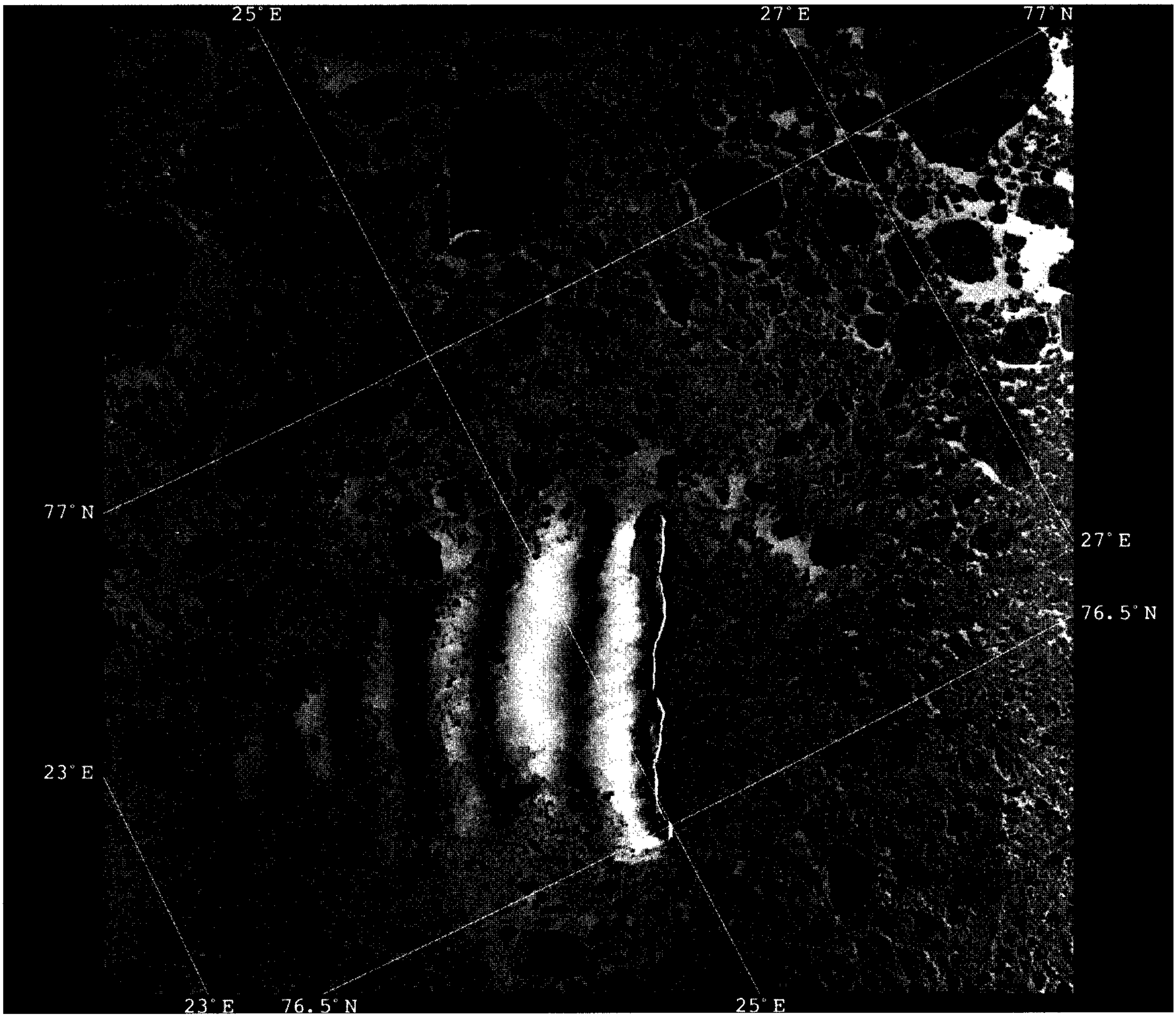

20-06-93

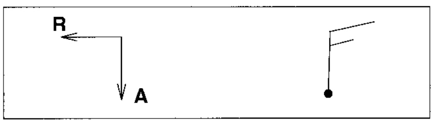

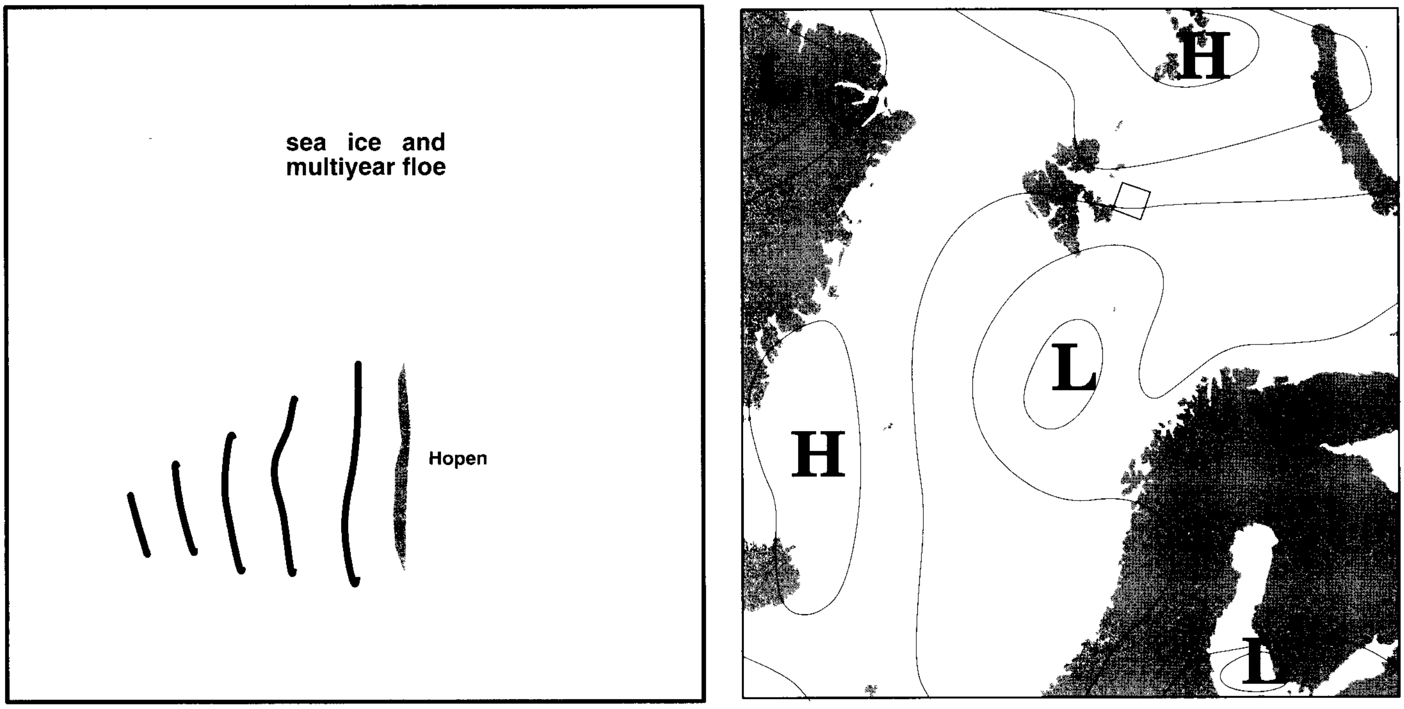

Figure 21: Interpreted image and weather map

The accompanying figure shows an ERS-1 SAR image which includes an atmospheric lee-wave pattern associated with the island Hopen. The image clearly shows the island surrounded by loosely packed ice floes, with a large ice-free area on the western side, created by easterly winds that had persisted during the previous 24-hour period. Six well-defined wave crests having a wavelength of 7.6 km and oriented nearly parallel to the island are readily apparent. With the calibrated ERS-1 SAR image and a wind-retrieval model, it is possible to estimate the amplitude of these waves, in addition to their wavelength scale, directly from the SAR image. Thus, these SAR observations are an improvement on visible-image remote-sensing studies of atmospheric lee waves, where only the wavelength scale and the arrangement of the wave crests, based upon the cloud pattern, could be analysed.

With the aid of the ERS-1 Scatterometer wind-retrieval model CMOD4 [35], the wind speed associated with the first two wind speed maxima was estimated to be 12 ± 3 m s^{-1} [38], and the intervening minimum wind speed was estimated to be 3 ± 3 m s^{-1}. Furthermore, it was shown that the observed wavelength and horizontal wind speed modulation were consistent with a simple lee-wave model that included an exponential decay of the Scorer parameter (the ratio of the buoyancy frequency and the wind speed) in the lower troposphere, and a bell-shaped barrier [29]. This model includes forced motion over the barrier plus a resonant oscillation downwind. In this case, the lee waves were trapped by a thin surface-based inversion layer and accompanying wind shear aloft. The lee-wave model was configured on the basis of atmospheric soundings taken at Bear Island, some 250 km to the southwest of Hopen.

Lee waves are a special case of atmospheric gravity waves in which the wave motion is forced over a terrain obstacle (see Gossard and Hooke [11] for example); i.e. they are generated by orographic interaction. In the steady state, lee waves are stationary with respect to the terrain feature, but they propagate with respect to the mean airflow above the Earth's surface. Observations of lee waves are rather common in visible remote-sensing imagery (see Gjevik and Marthinson [10], for example). In this case, they manifest themselves as wave-like cloud patterns: spatially periodic uplifting of

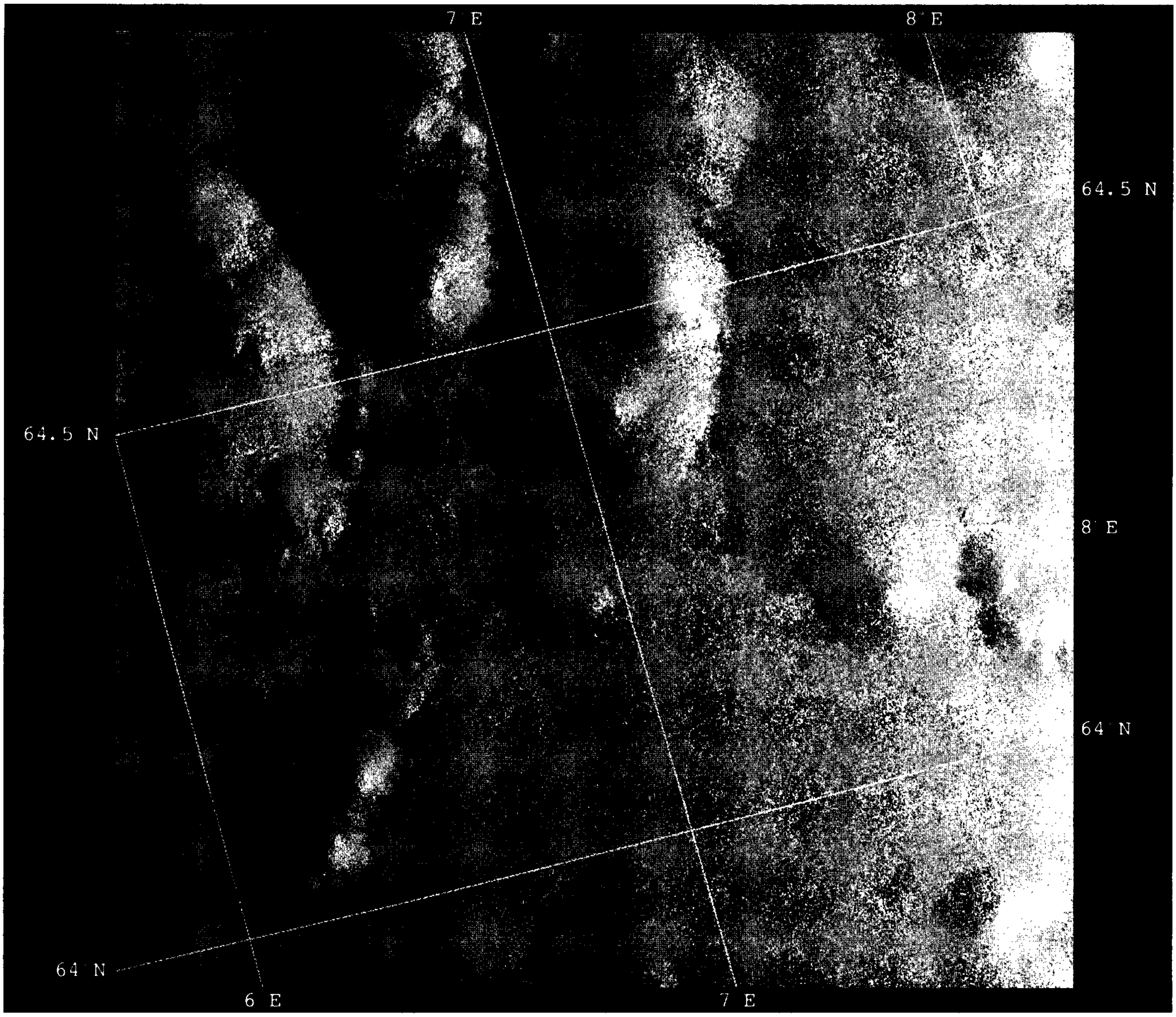

20-11-91

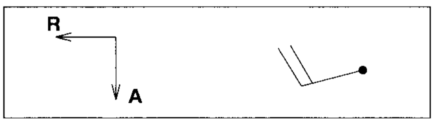

moist air results in condensation and forms cloud patterns associated with the lee-wave crests. The main advantages of analysing lee waves rather than more generic atmospheric gravity waves are that the wave pattern may be taken as steady-state (not propagating) and that the vertical and horizontal motion associated with the lee wave may be estimated since the lower boundary condition must follow the known terrain profile.

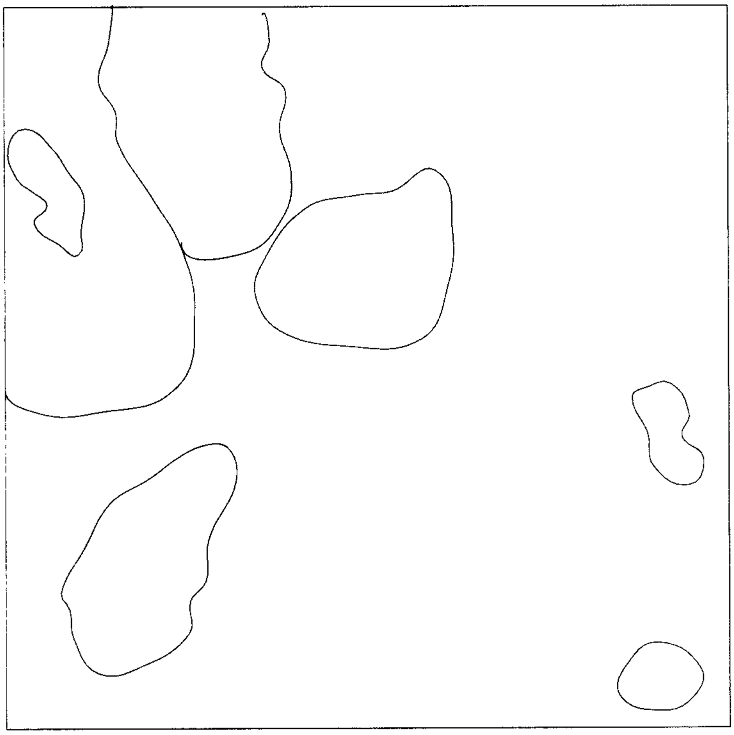

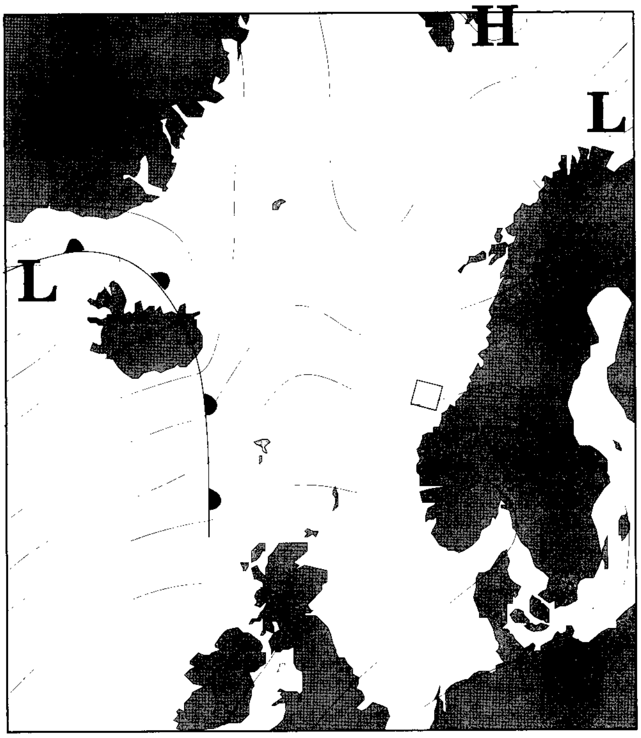

Figure 22: Interpreted image and weather map

3.1.4 Rain cells

This ERS-1 SAR image of Haltenbanken off the west coast of Norway shows a series of squall lines. At the top left of the image there is some indication of heavy rain creating dark areas. The sketched curves in the interpretation indicate the areas of rain cell coverage.

When heavy rain falls on the ocean surface, it creates turbulence which may damp out the Bragg scattering waves. The result is an area of low radar backscatter in the centre of the heavy rainfall and an increased backscatter from the surrounding areas. The areas have characteristic forms due to the strong wind squalls that carry the cold descending air away from the cell centre (see Figure 23). The distinct boundaries between the wind squalls and the surrounding calm water are called squall lines. Rain squalls are particularly common in subtropical regions, but are also observed elsewhere, e.g. along the coast of Norway.

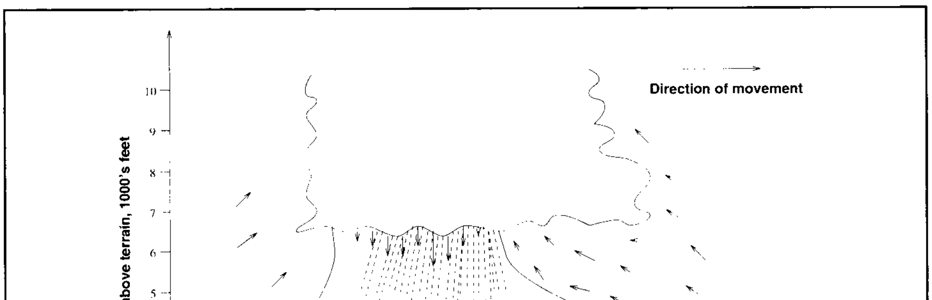

Figure 23: A sketch of the downdraft in a storm which creates distinct patterns in SAR imagery

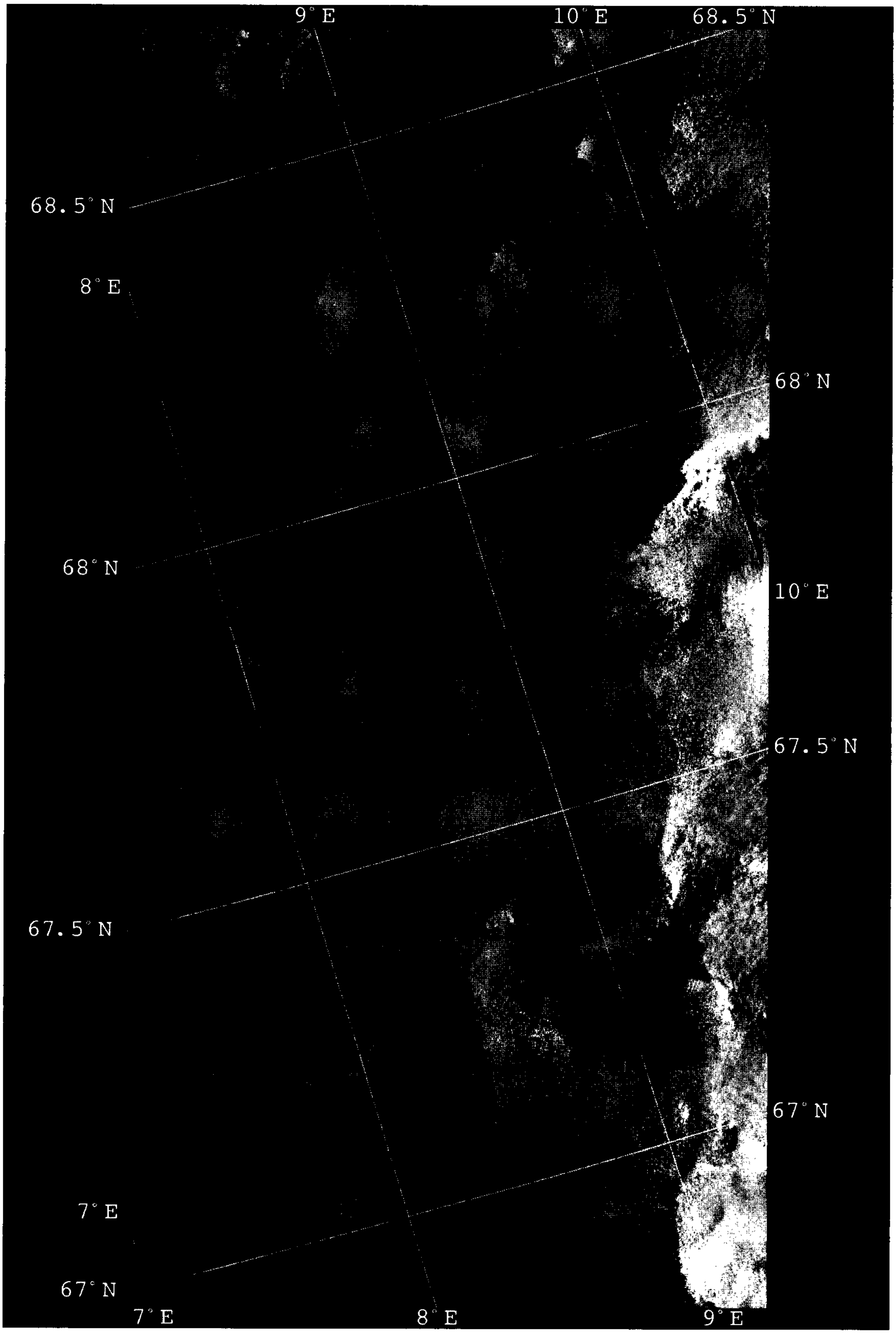

12-10-93

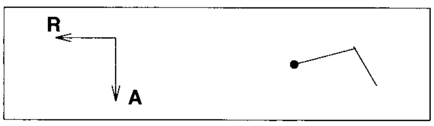

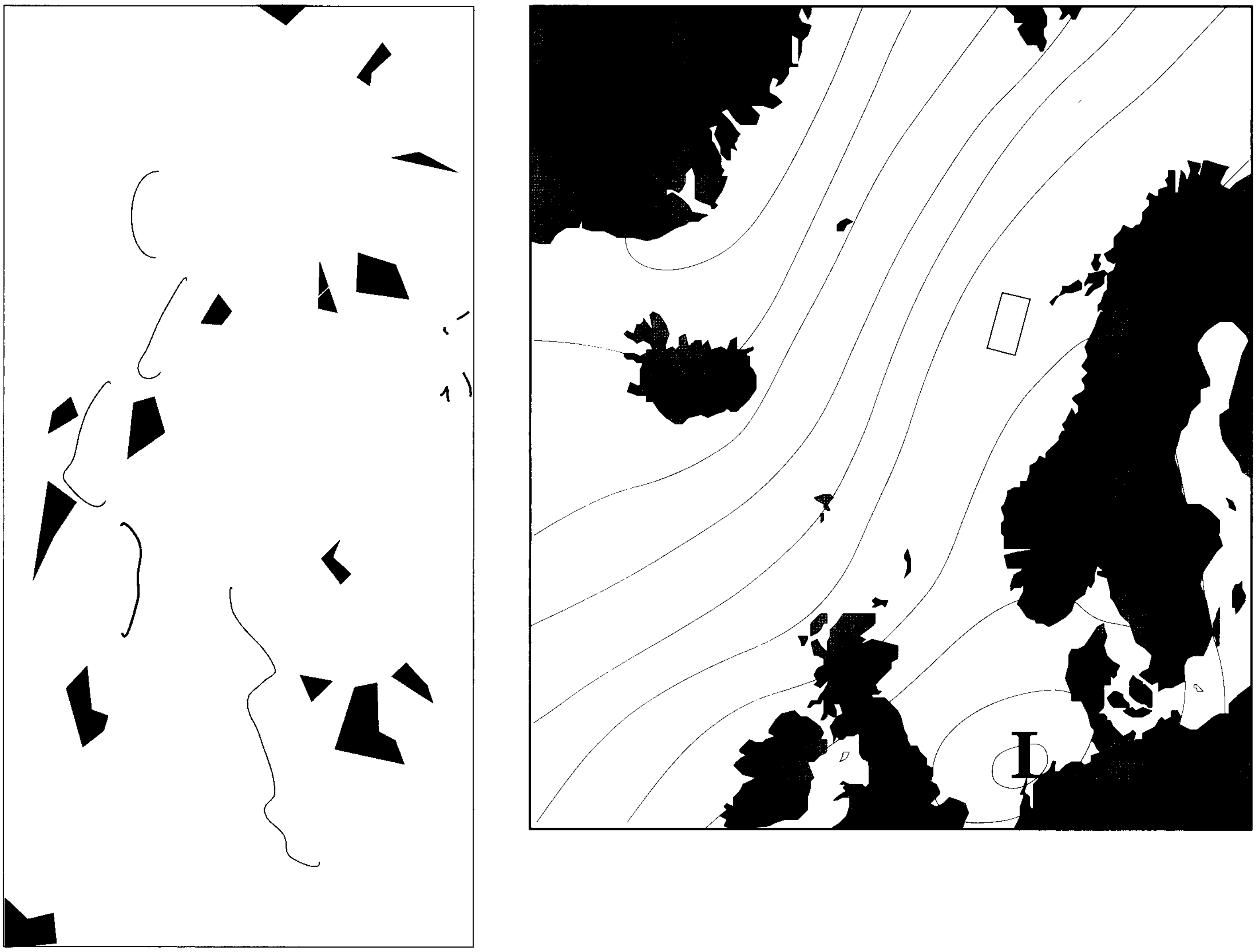

Figure 24: Interpreted image and weather map

In the next image, taken on 12 October 1993, there is some indication of heavy rain creating dark areas. A cluster of rain cells is seen off Vaerøy, southwest of Lofoten. The cell centres have a very low radar backscatter, and are indicated as the black regions in the interpretation image. The major squall lines are also marked. A back-scatter profile through one of the centres is shown in Figure 25.

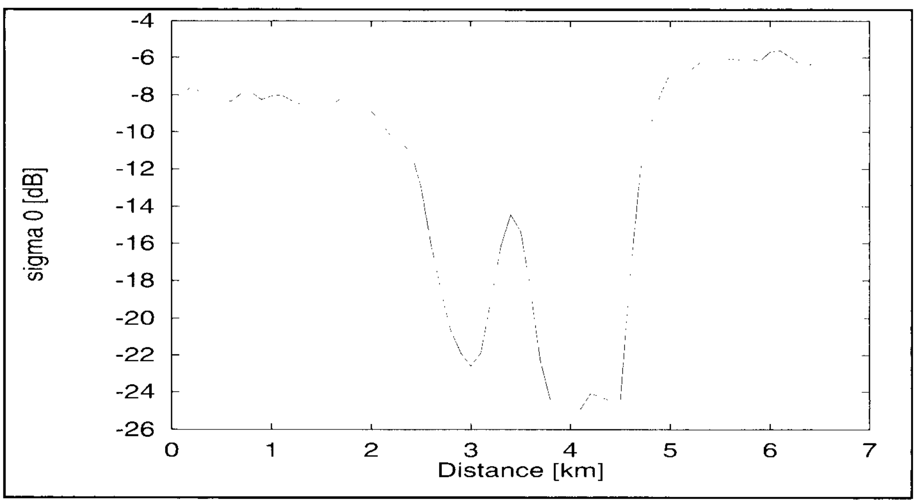

Figure 25: Backscatter cross section through a rain cell centre. The position of the profile is marked by the arrow in the interpretation figure

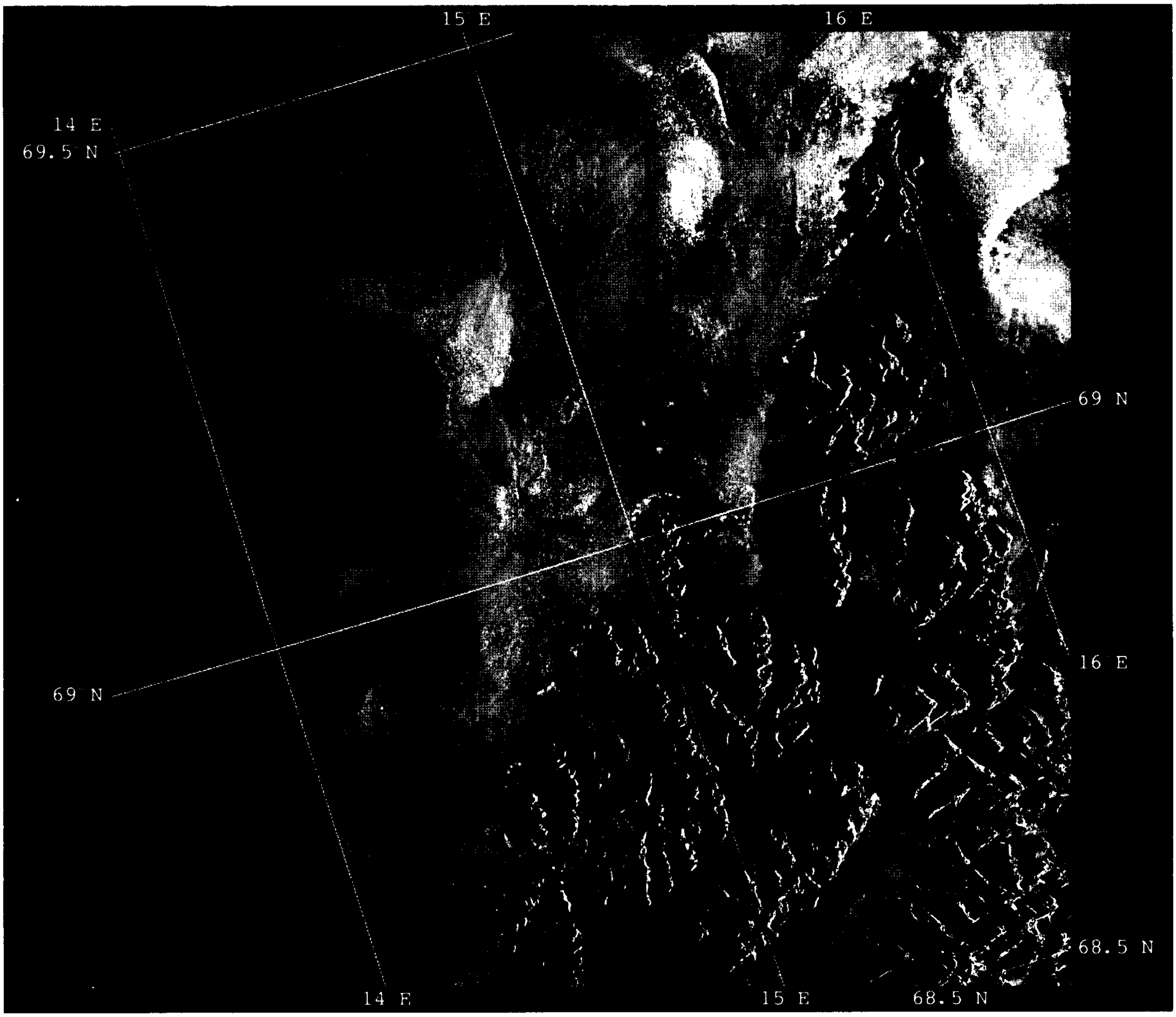
15 E
16 E
14 E
69.5 N
69 N
69 N
16 E
68.5 N
14 E
15 E
68.5 N

19-10--93

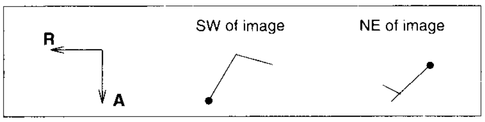
R
A
SW of image
NE of image

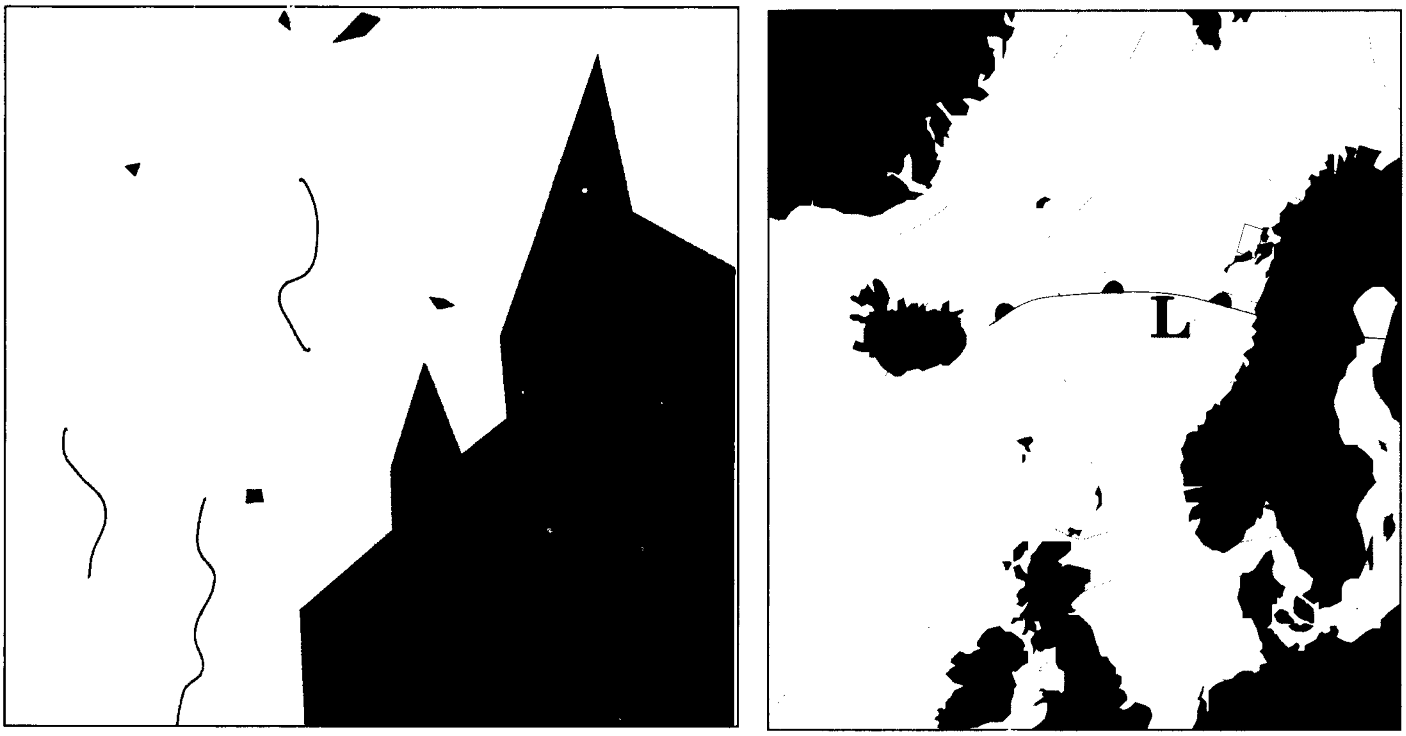

Figure 26: Interpreted image and weather map

In the image taken on 19 October 1993, there are seen to be rain cells creating squall lines off the coast of Lofoten on a day when the wind speed was measured to be only about 2 to 3 m s^{-1}. The squall lines are shown as thin lines and rain cell centres are indicated by dark spots in the interpretation image.

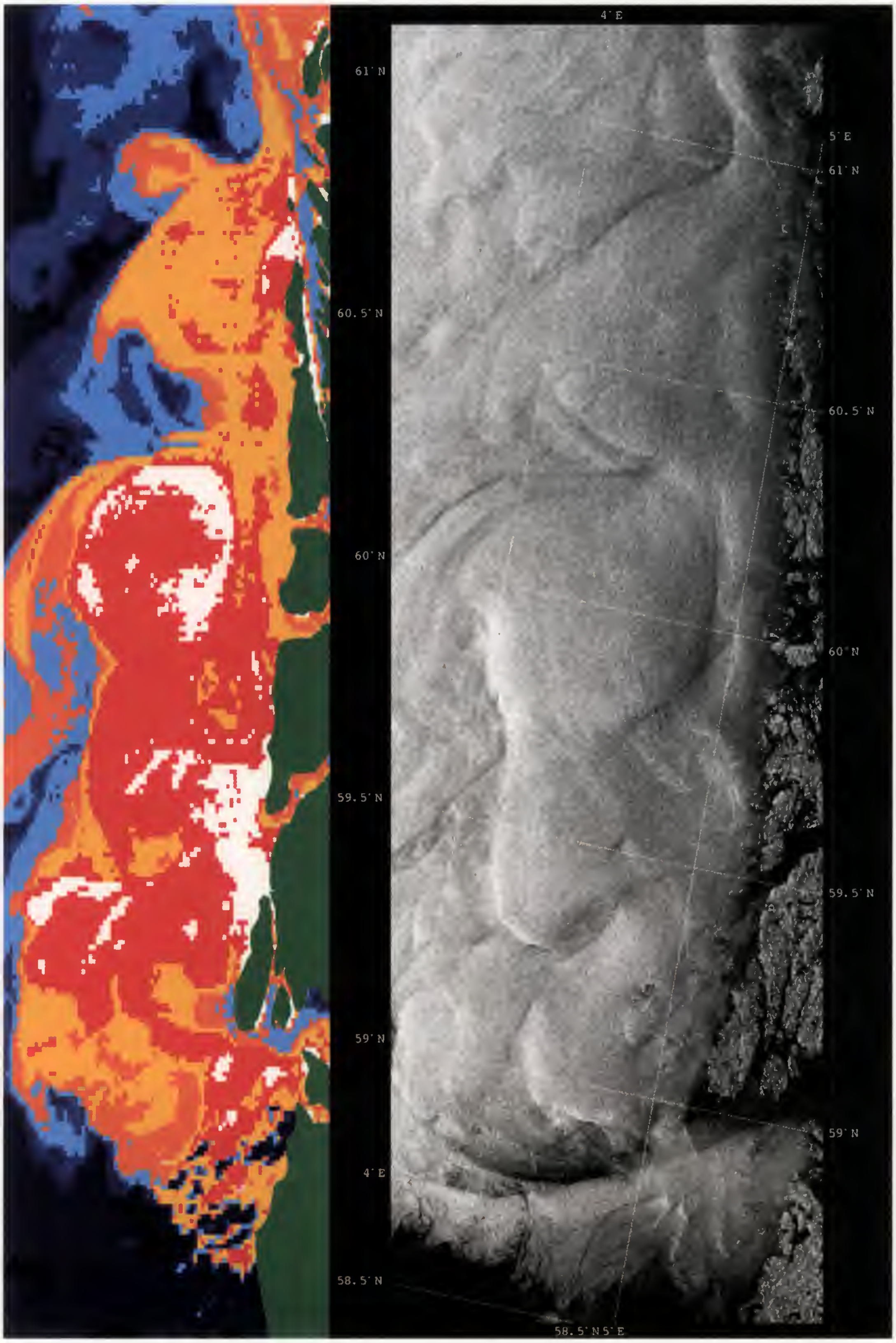
4°E
61°N
5°E
61°N
60.5°N
60.5°N
60°N
60°N
59.5°N
59.5°N
59°N
4°E
59°N
58.5°N
58.5°N 5°E

03-10-92


A
R

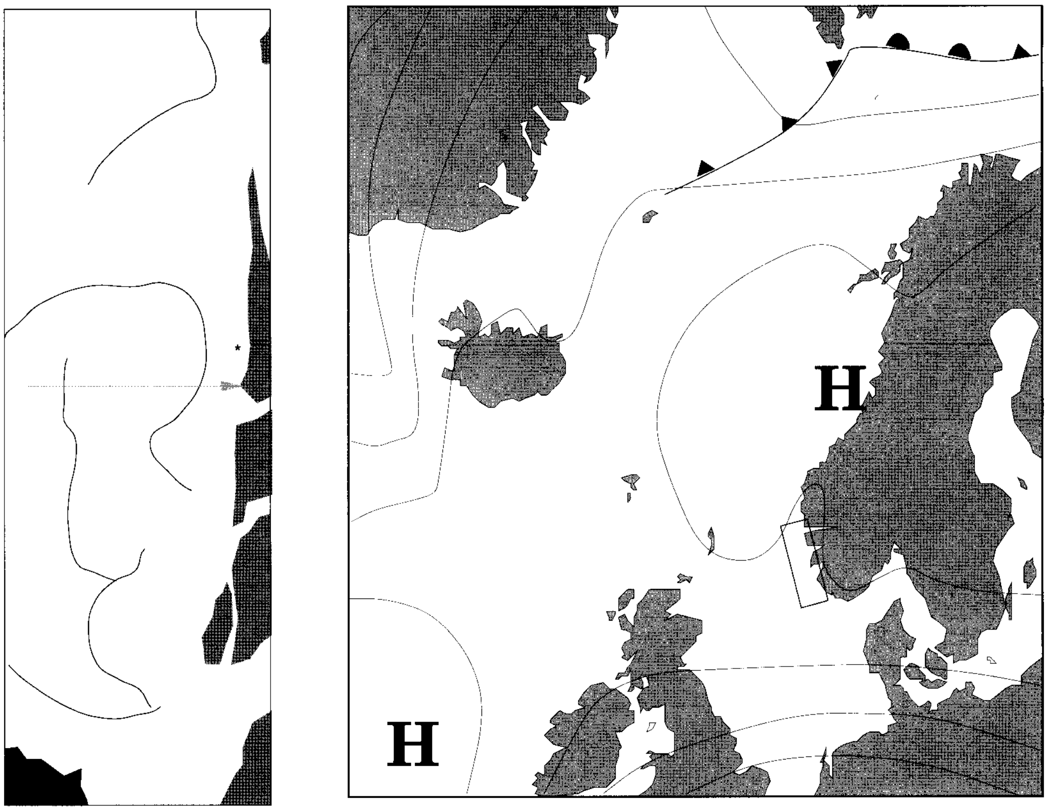

Figure 27: Interpreted image and weather map. The asterisk in the interpretation indicates the position of a Seawatch buoy

3.2 Upper ocean

3.2.1 Current boundaries

The NOAA AVHRR image (left) and the ERS-1 SAR image (right) were obtained six hours apart on 3 October 1992 and cover a region approximately 100 km by 300 km off the west coast of Norway. The radar and radiometer manifestations of surface roughness and sea surface temperature can be compared. The spatial resolution in the infrared image is 1 km as compared with 100 m in the SAR image. AVHRR images are frequently used in studies of water-mass distribution and ocean circulation, and several examples have demonstrated that mesoscale ocean-circulation studies can be performed with the aid of the multisensor AVHRR and a radar altimeter (measures sea-surface slope) [41]. SAR images, on the other hand, have not until recently been systematically used in studies of mesoscale current features. The multisensor-IR/SAR comparison clearly favours the SAR's imaging capabilities. There appears to be a remarkable relationship between the sea surface temperature and roughness field. In the IR image the surface temperature decreases from 14°C (white) in the coastal water to 12°C (dark grey) in the Atlantic water offshore, implying the existence of the weak temperature contrast typical of this time of the year. The maximum temperature gradient is about 0.75°C km^{-1}. Across the temperature fronts, corresponding salinity and hence density fronts are present that maintain a change in the current velocity. The structure of the sea-surface-temperature field, with the curved paths of the temperature fronts, represents the mesoscale meandering pattern of the unstable Norwegian Coastal Current (NCC) with typical scales of about 50 km [23]. Smaller, 10-km-sized features are also observed. The coastal

Figure 28: Profile along the arrow indicated in the interpretation. The profile shows a 2 dB peak at the left-hand side and a 1.5 dB dip at the right-hand side

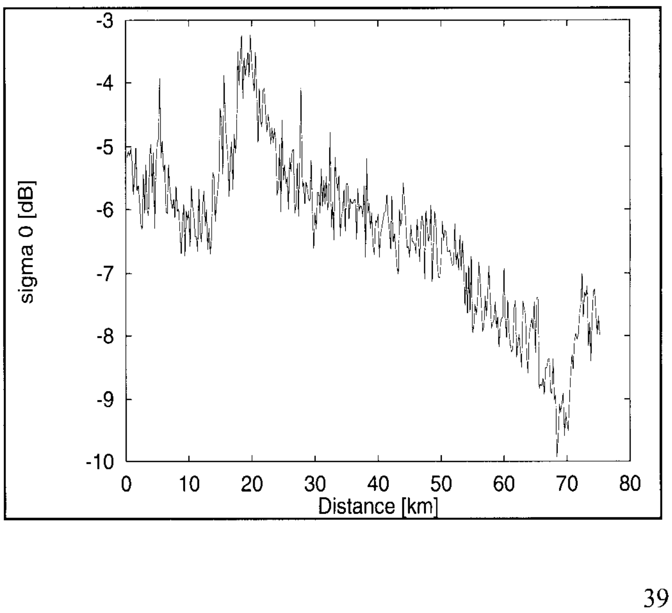

islands and the mainland are green, while clouds are masked as black in the lower part of the image.

The ERS-1 SAR image contains frontal features with configuration and orientation that are in good agreement with those seen in the IR image, both at the 50 km scale and at smaller scales of about 10 km. The coastal landscape is seen along the right-hand boundary of the image, with backscatter slightly different from that of the sea. The SAR frontal boundaries are represented by both dark and bright radar cross-sections of varying cross frontal width, in particular the bright front in the central part of the image. Spatial variations of the radar cross-section are usually induced by larger-scale features and processes such as long gravity waves, variable near-surface wind fields, air/sea temperature differences, and upper ocean circulation features, including mesoscale meandering fronts and eddies [42,14,5,39,24,3,17,9,22]. Under moderate winds between 3 and 10 m s^{-1}, the SAR is seen to be capable of revealing current boundaries, including meanders and eddies. It is suggested that the corresponding imaging mechanisms alternate among the following:

(1) damping of short gravity waves by the presence of natural slicks aligned along the frontal boundary;
(2) short gravity-wave/current interaction along shear and/or convergence zones within the front;
(3) changes in wind stress induced by strong gradients in the sea surface temperature; and
(4) long-gravity-wave/current refraction.

Auxiliary data will be required in order to rank these mechanisms.

Northerly winds of about 5 m s^{-1} and air temperatures of between 12 and 14°C were reported along the coast from the analysed weather map. Furthermore, a northward near-surface current of about 0.30 m s^{-1}, a temperature at 50 m depth of 14°C, and a significant wave height of about 1 m were reported from one Seawatch buoy deployed about 20 km offshore (asterisks). Since the temperature fronts are relatively weak, and the air/sea temperature difference remained close to neutral, the SAR image signature is not significantly modulated by wind variations induced by changes in the boundary layer stratification [4,20]. Moreover, salinity gradients are not reported to provide backscatter anomalies. Hence, according to Johannessen et al. [20], the SAR image signatures are interpreted to be a manifestation of short-gravity-wave/current interaction along the current fronts. As the short gravity waves are propagating into and/or across the current front, they change steepness and propagation direction as long as the wind is moderate. Consequently, the SAR is capable of detecting the current fronts. It is evident that this SAR image interpretation is strongly supported by the nearly coincident sea-surface-temperature field mapped in the cloud-free satellite IR image. The combined analysis therefore supports the multisensor approach to improved utilisation of the remote sensing data in mesoscale ocean studies.

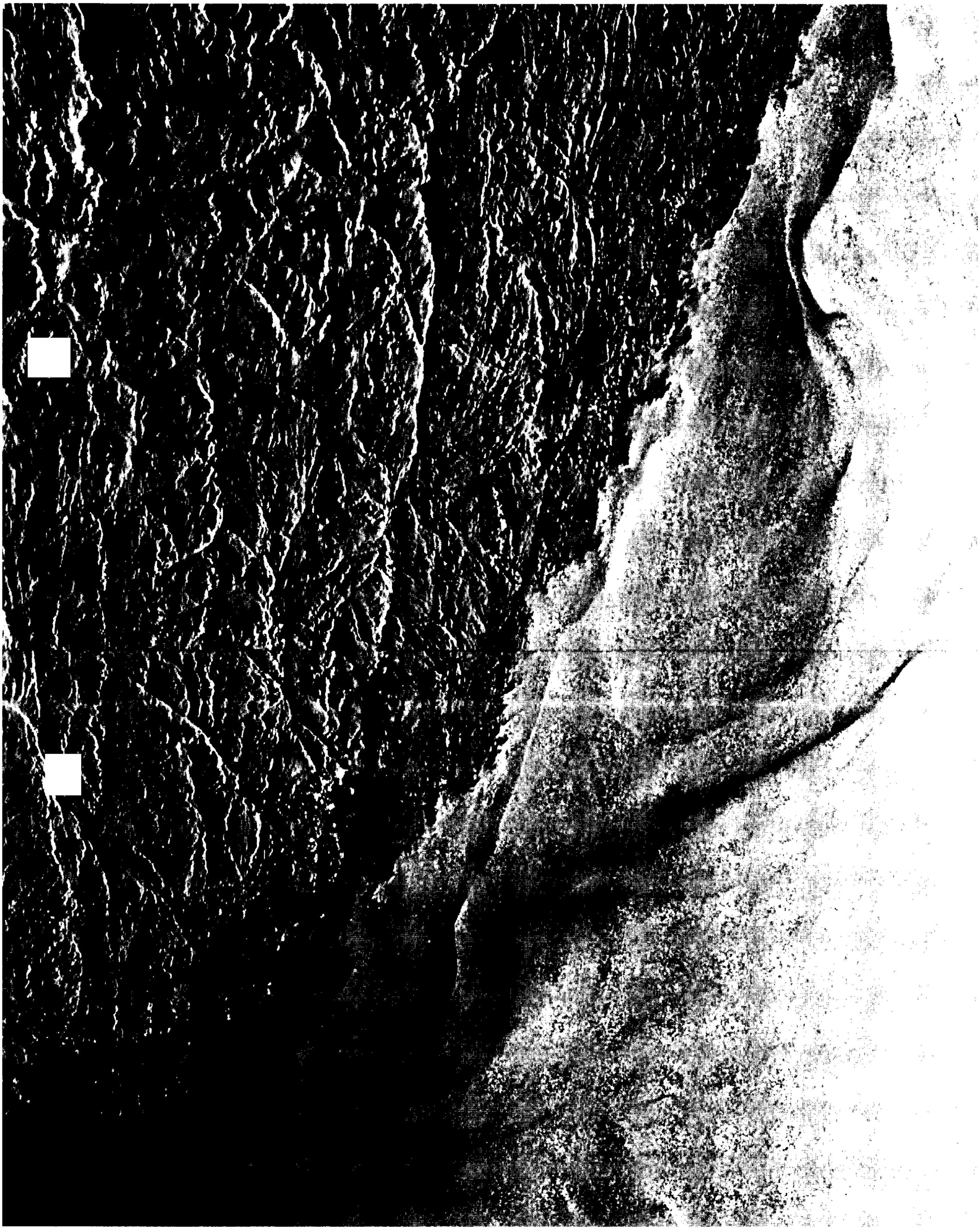

This radar image from 21 September 1994 shows bright and dark radar cross-section perturbations observed along the front of the Norwegian Coastal Current off the southeast coast of Norway

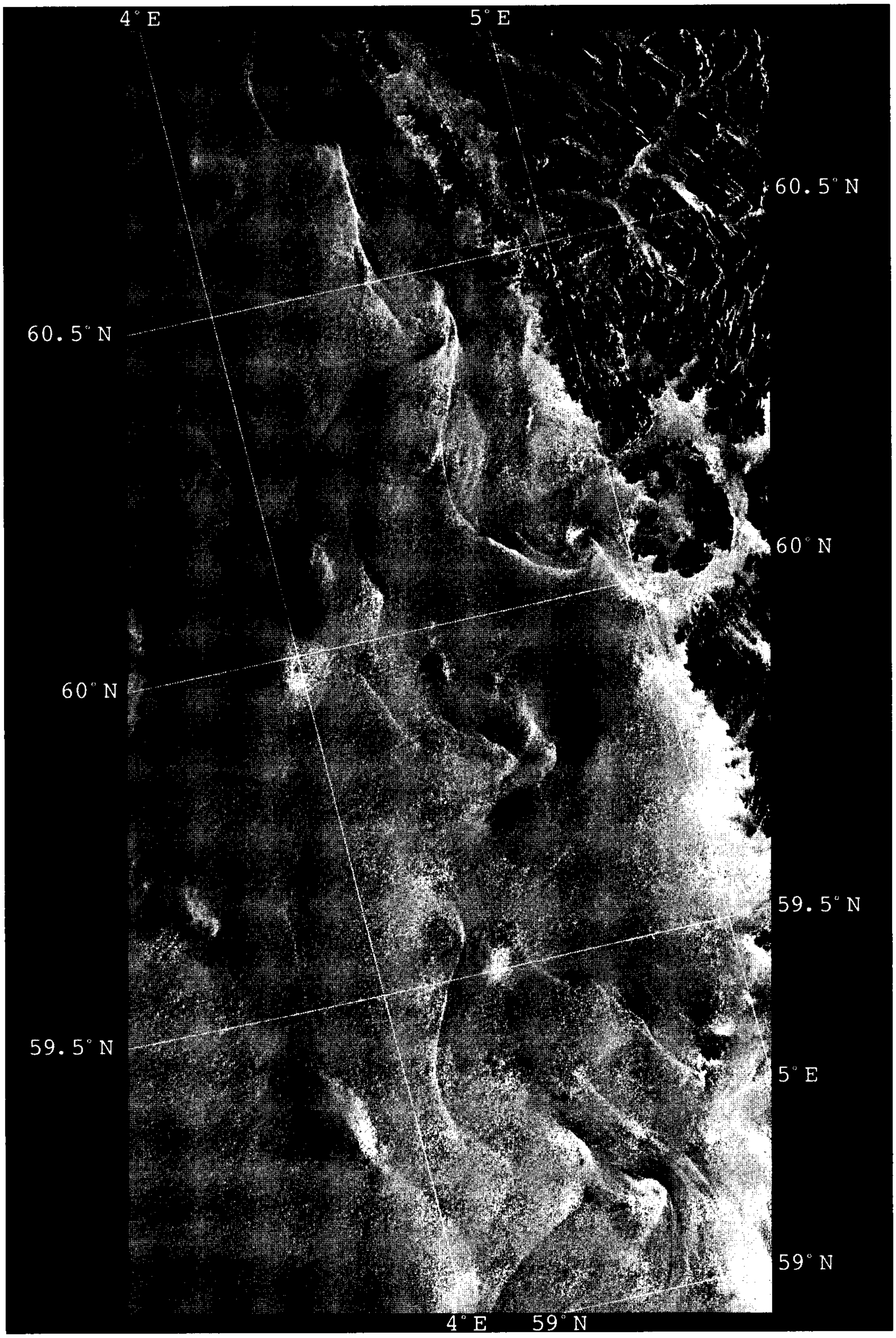

02-12.-93

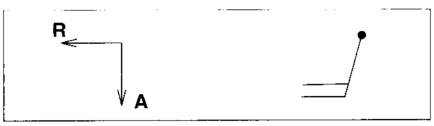

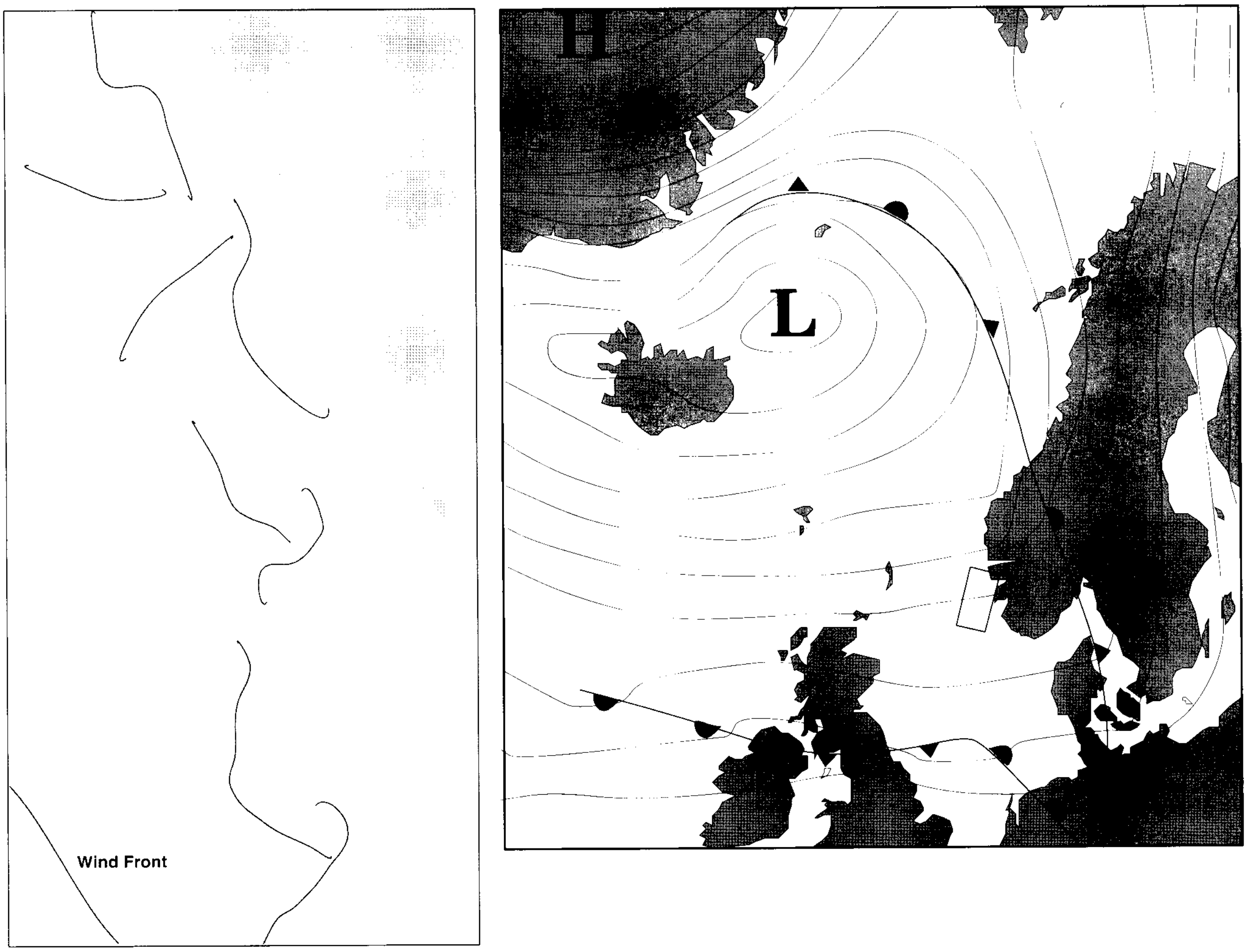

Figure 29: Interpreted image and weather map

The next image is of an area off the southwestern coast of Norway and was taken on 2 December 1993. In the interpretation (Fig. 29), several frontal boundaries are marked. The fronts are revealed by both bright and dark departures from the surrounding mean radar intensity. Again the wavelengths are of the order of 50 km as in the previous SAR image. The tendency for the fronts to be found closer to the coast in the northern sector agrees with previous observations [23]. A weak wind front is found in the southwest corner of the image. Westerly winds of about 10 m s^{-1} from the south are reported at the time of SAR acquisition.

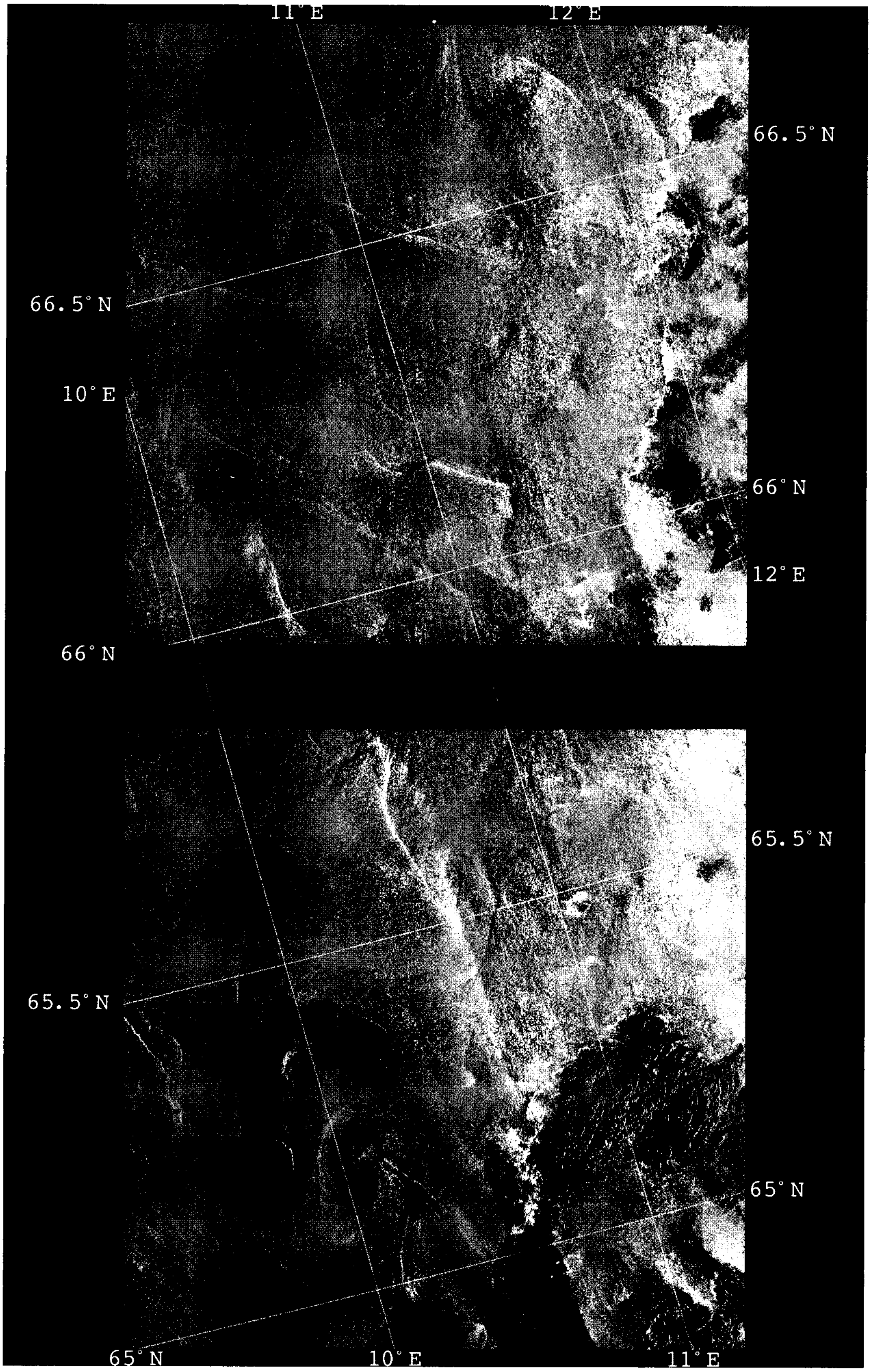

26-03-93

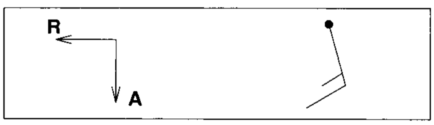

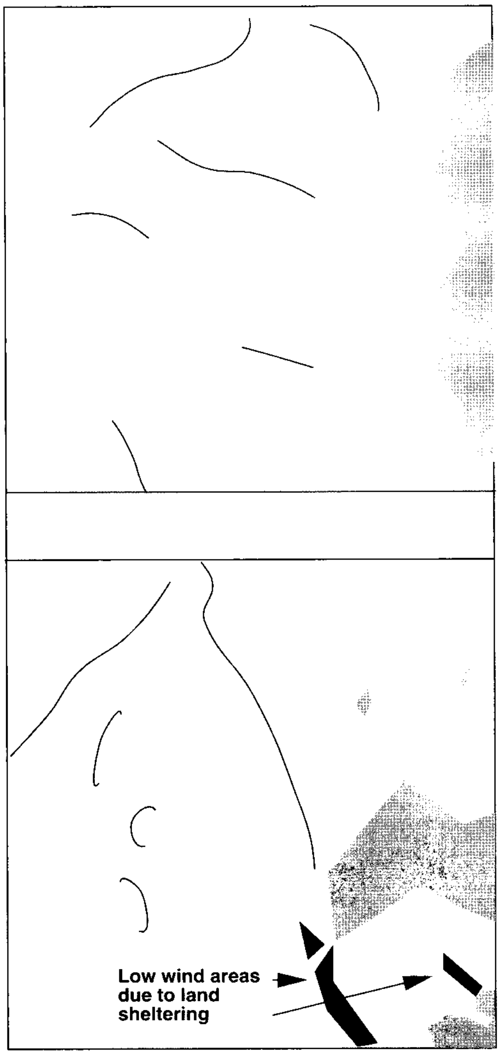

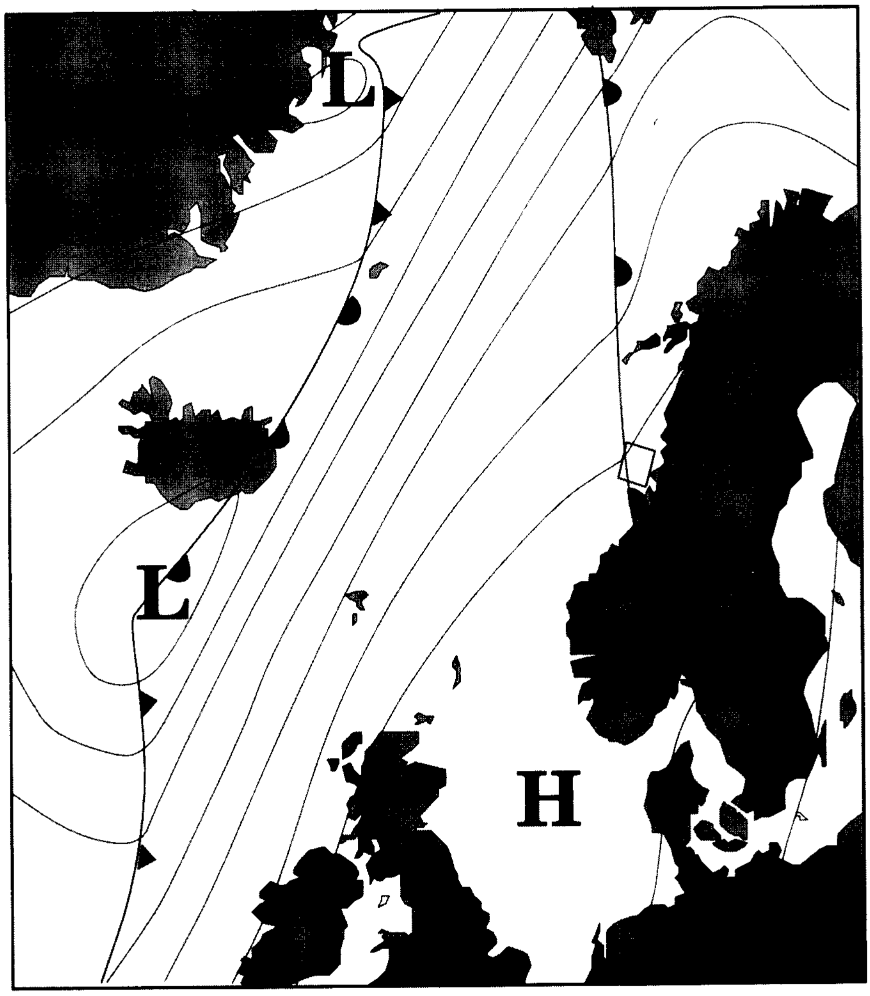

Figure 30: Interpreted image and weather map

The interpretation of the image taken on 26 March 1993 off the western coast of Norway shows a mixture of curved fronts and small-scale eddy features. Calm northerly winds of about 3 m s^{-1} are reported. The Norwegian Coastal Current in general flows northwards in this region. Several topographic features are present which can cause steering of the current, and we assume that to some extent this is expressed in the SAR image.

06-05-93

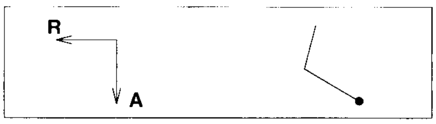

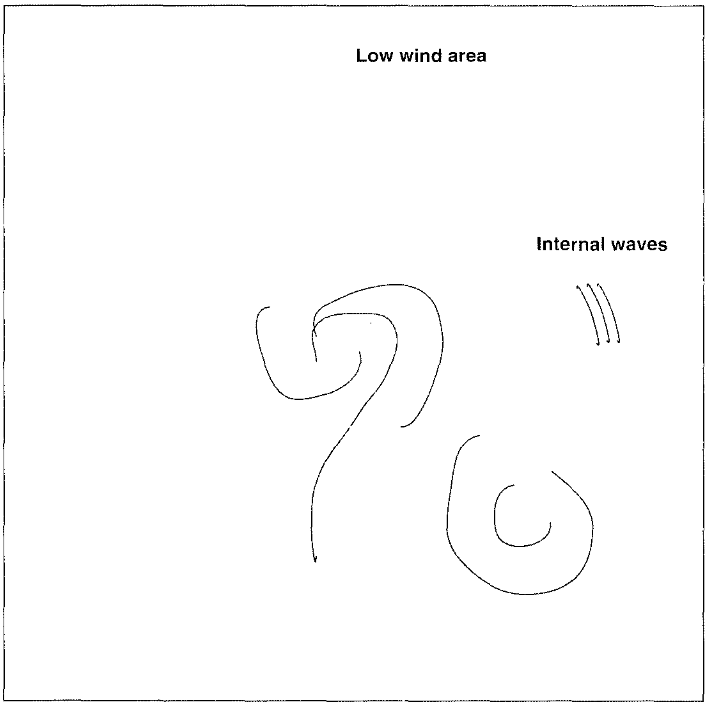

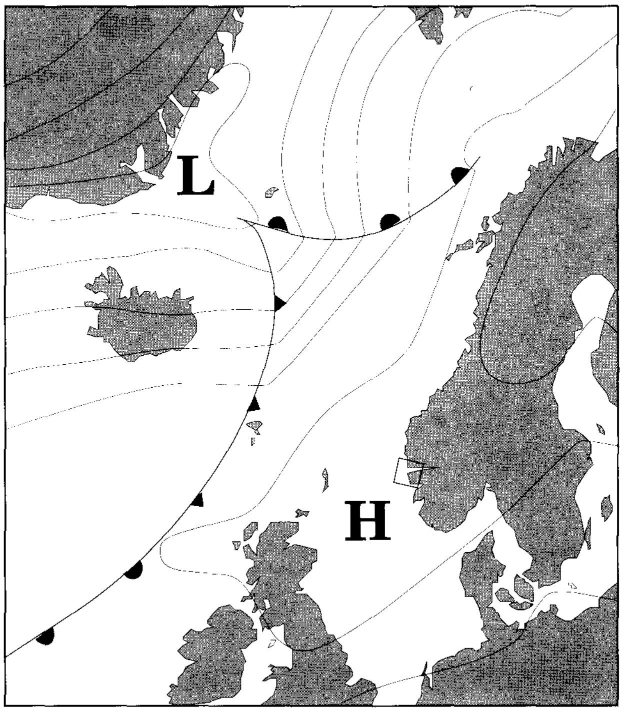

Figure 31: Interpreted image and weather map

3.2.2 Eddies

This ERS-1 SAR image was acquired off the southwest coast of Norway on 6 May 1993. The eddy structures are presumably responsible for collecting the surfactants into the curved and spiral patterns observed. The abundance of surfactant material was probably coincidental with the spring blooms of algae and other planktonic organisms, which release hydrophobic oils. The band of low wind velocities stretching down the right-hand side of the image exposes a train of bright internal wave crests propagating westwards. The synoptic wind recorded close to the time of acquisition was 10 knots from the northwest.

A backscatter profile across a dark band in the image is shown in Figure 32.

Eddies usually show up in SAR images as a result of wave/current interaction, which outlines the curved shape of the eddy, or are revealed indirectly through the presence of natural film trapped within spiralling lines associated with the eddy's orbital motion. In connection with eddies having strong thermal signals, such as warm or cold rings, the eddy can also be expressed by the change in wind stress across the temperature front [27]. Along the coast of Norway the latter type of expression is rare.

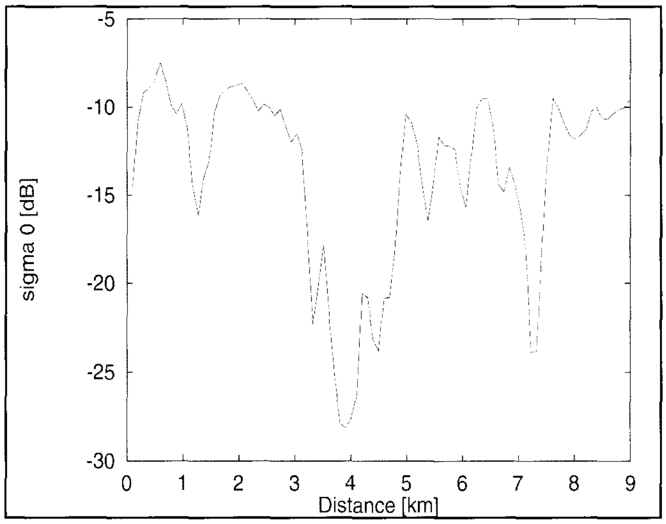

Figure 32: Backscatter cross section across a dark band in the image. The position of the profile is marked by the arrow in the interpretation figure

In the ERS-1 SAR image acquired off the southwest coast of Norway on 6 May 1993, a cyclonic eddy feature is revealed by the spiral-shaped lines associated with small-scale turbulence aligned in the direction of the orbital motion of the larger-scale eddy. The turbulence, in turn, leads to convective motion in the water that can bring organic material present in the upper layer to the surface where it can remain as a microlayer of natural surface film [39]. As the concentration of this surface film (surfactant molecules) increases, it can exert sufficient surface tension to inhibit the growth of capillary and short gravity waves. In addition, the film edge may reflect the short waves that propagate at oblique angles to it, thus limiting the advance of short-wave roughness through the slick-covered region. In turn, the lack of small-scale surface roughness attenuates the radar echo from the surface, which means that the surface slicks show up as dark, low-backscatter features. In the SAR image, the intensity of the dark spiral lines does not vary as a result of radar look angle dependence. The dark spiral lines are expected to disappear at higher wind speeds (7 m s^{-1}) since wind-induced mixing in the upper layer will redistribute the surface slicks and prevent the damping mentioned above [34]. Hence, the fully developed 0.07-0.08 m waves necessary to provide resonant Bragg backscatter are formed in the eddy region, and surface film if present in sufficient concentration can in turn cause the formation of areas of slick, which leads to the backscatter contrast of about 6-10 dB. In addition, the backscatter front and region of low radar return in the eastern sector are caused by the fact that the wind has dropped below the threshold.

The spiral lines suggest convergence towards the eddy centre. Indications of the convergence suggest that this cyclonic eddy may be important for the distribution and concentration of chlorophyll *a*, algae and pollutants such as oil spills. These synoptic manifestations of the eddy's rotational direction, horizontal dimensions and possible surface convergence offer a valuable opportunity for comparison and validation of model simulations of surface-current pattern [18]. Moreover, since there is no sequence of SAR images of this case, the temporal characteristics of such eddies, as they form, develop or decay, cannot be determined, unless such observations as this are combined with modelling tools.

SAR image received at Tromsø Satellite Station (Norway) of the cyclonic eddy in Frohavet obtained at 21:10 UTC on 21 August 1991. The image is a blow-up of a standard scene (100 km × 100 km) with a size of 25 km × 25 km. The pixel size in this full-resolution image is 16 m in azimuth and 20 m in range. The bright point return in far range is caused by a ship, whereas larger bright returns in near range and along image top are coastal islands. Data reception and SAR processing were carried out at Tromsø Satellite Station. The image was processed at Nansen Environmental and Remote sensing Center. Arrows mark azimuth and range (look) directions. (Copyright ESA)

26-03-93

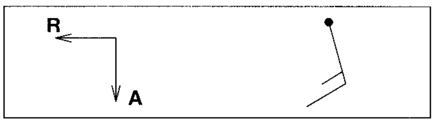

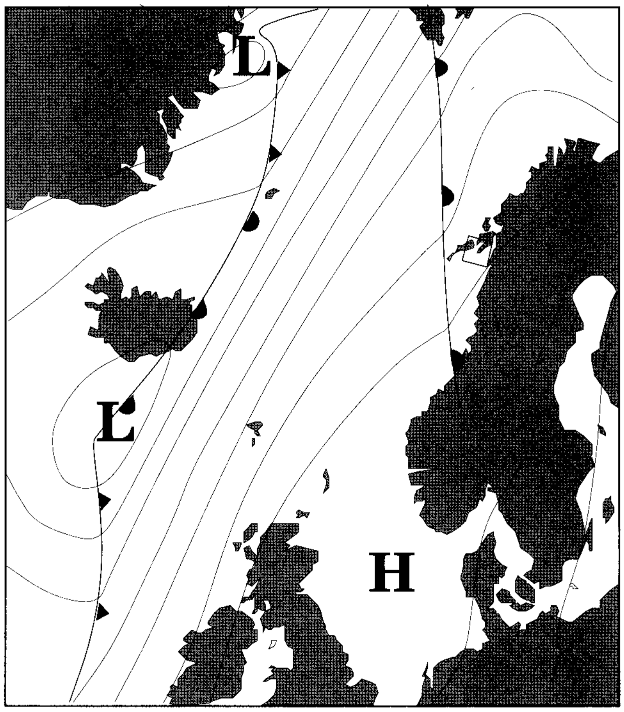

This ERS-1 SAR image, which is from 26 March 1993, is an example of the way in which eddy currents are made visible as a result of short-wave/current interaction near the Lofoten Islands. The curved lines in the interpretation (left-hand figure) indicate regions of high backscatter, probably caused by roughened surface water within certain sectors of the eddies. The synoptic wind was reported to be southerly with a speed of 7-8 m s^{-1}.

Figure 33: Interpreted image and weather map

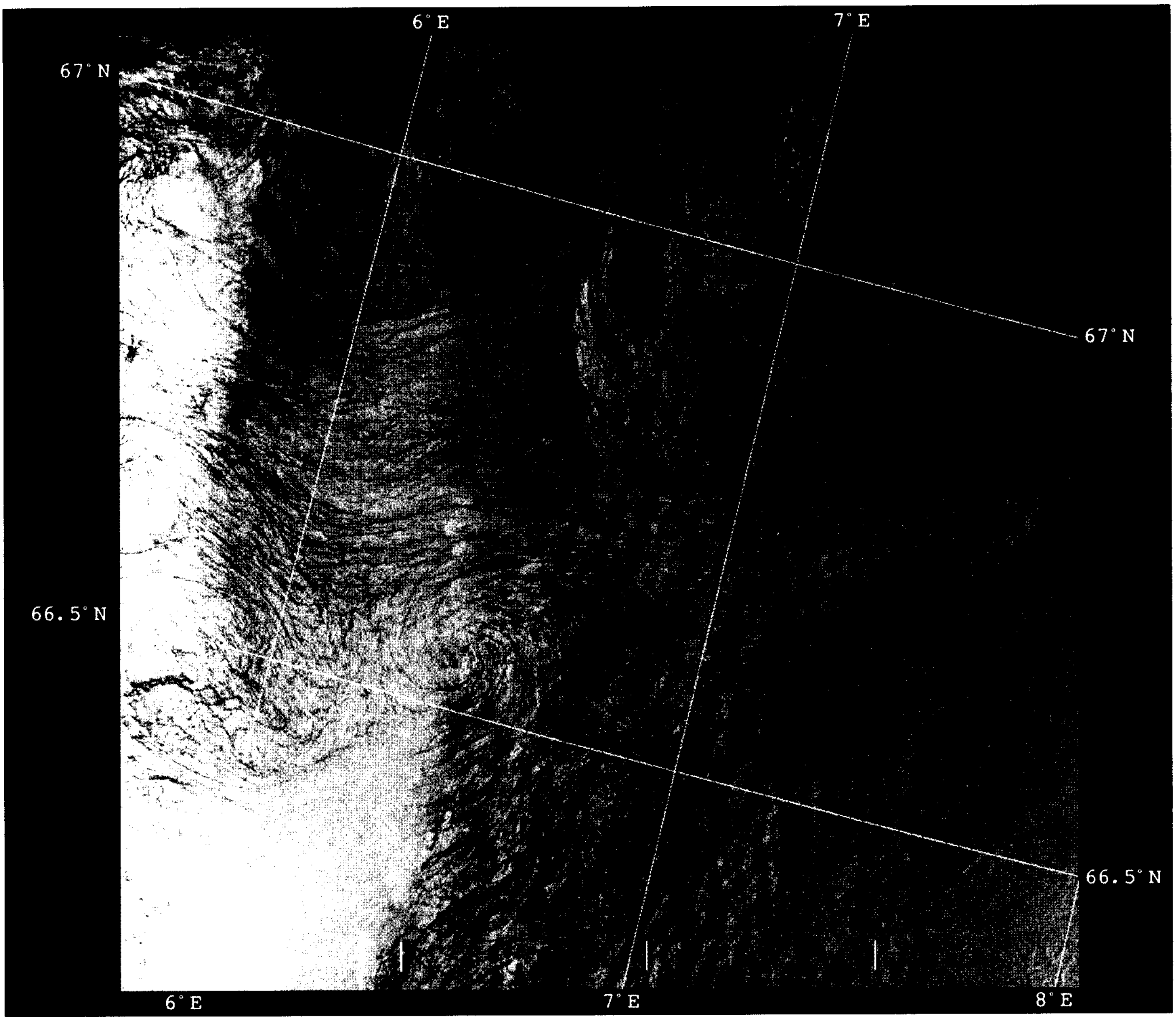

14-07-93

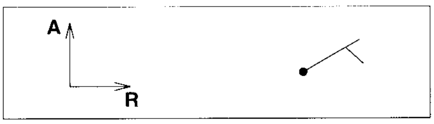

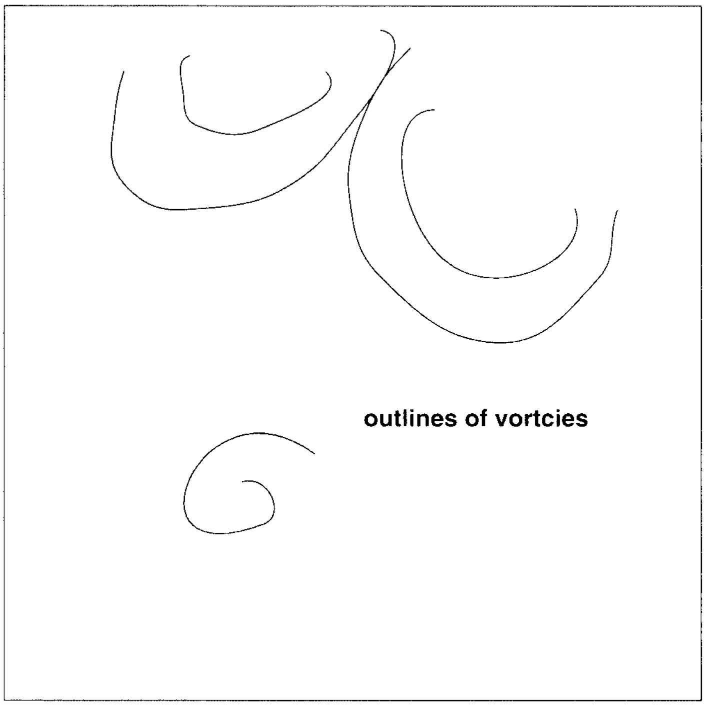

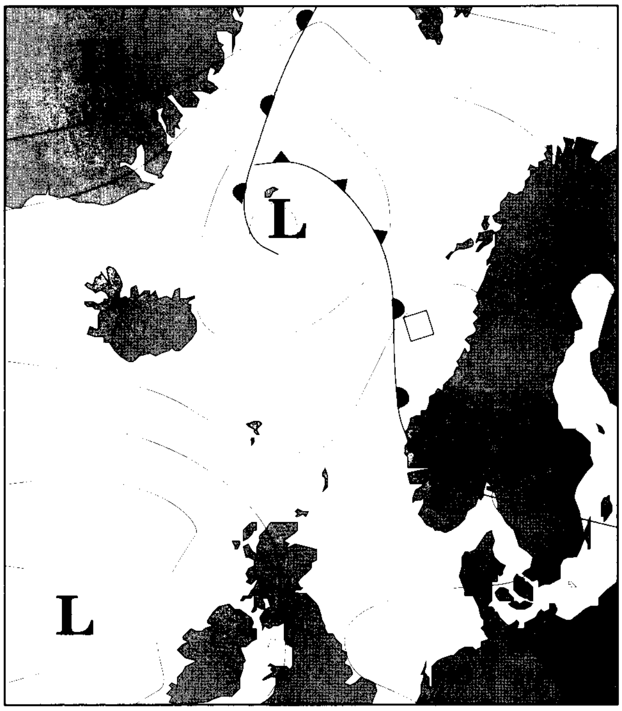

This ERS-1 SAR image is from 14 July 1993 and shows a series of cyclonic eddy structures off the west coast of Norway. Accumulation of surfactants is assumed to be the reason for the streaked ribbonlike patterns of low backscatter. The synoptic wind recorded in the region close to the time of acquisition of the image was 5 m s^{-1} from the north. The lines in the interpretation (left-hand figure) mark vortex outlines.

Figure 34: Interpreted image and weather map

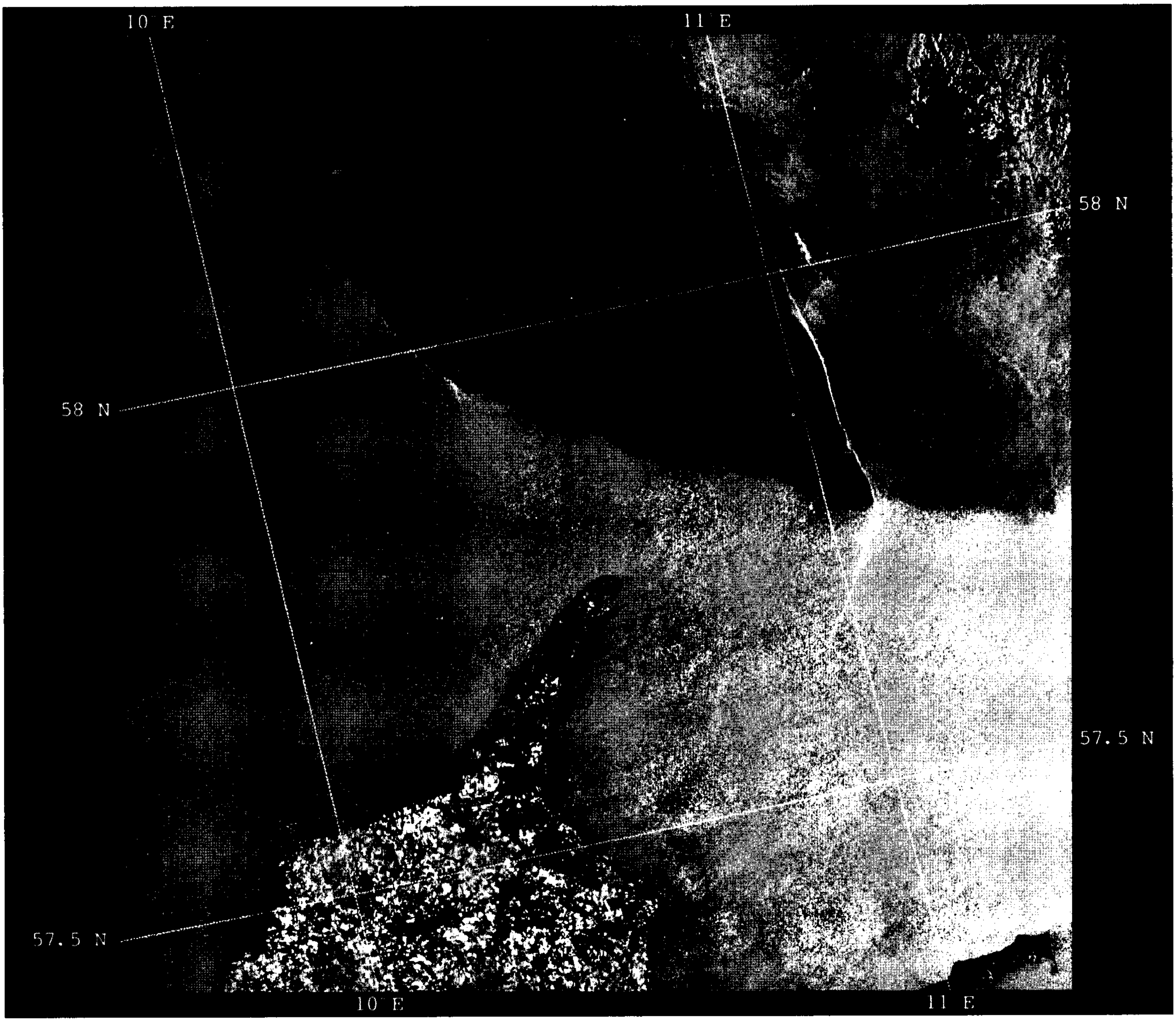

13-10-93

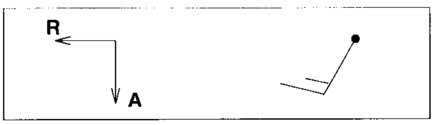

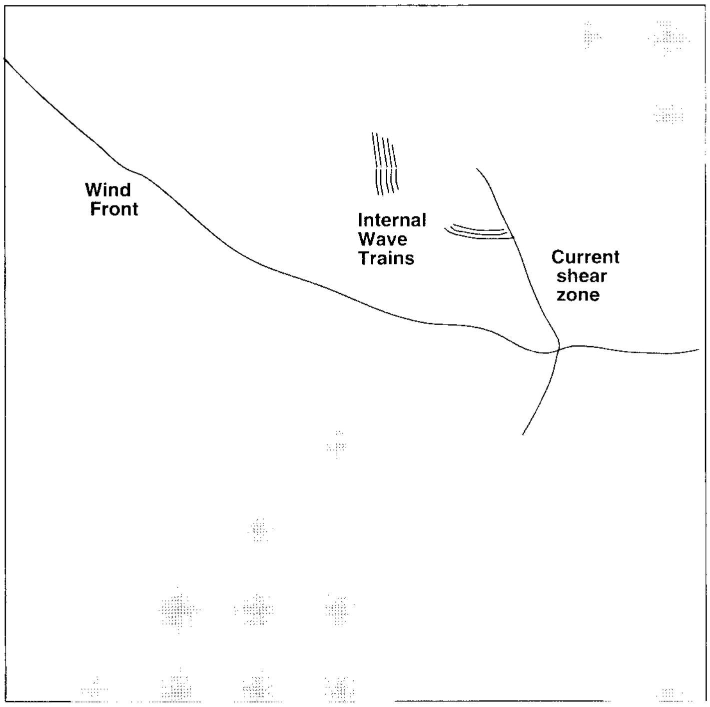

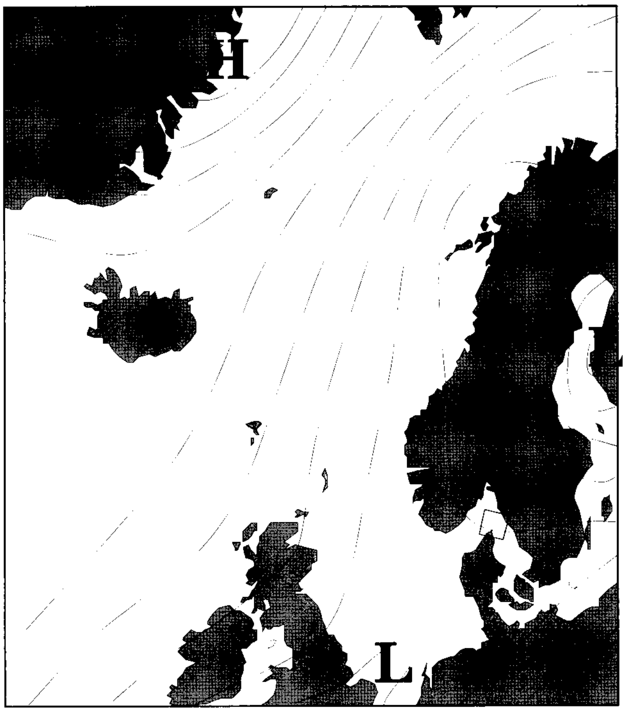

Figure 35: Interpreted image and weather map

3.2.3 Internal waves

The ERS-1 SAR image from 13 October 1993 shows the northern part of the Kattegatt between the Skagen peninsula in Denmark and the western coast of Sweden. Packets of internal waves are visible in the dark region, which is in the lee of the wind front, represented by the north-south boundary between rough (light) and calm (dark) water. The wavelengths seem to indicate that the group is propagating westwards, since the spacing between waves increases away from the leading edge as is to be expected in dispersive waves. The crest lengths are seen to decrease towards the trailing edge. It is assumed that tidal currents are responsible for creating the internal waves. The bright linear feature to the east of the image, oriented in a north-south direction is thought to show current shear. The local wind speed was recorded as $7\,m\,s^{-1}$ from the southwest.

Figure 36 shows the perturbation in surface roughness created by the packet of internal waves. The amplitude of the backscatter perturbation is seen to decrease away from the leading edge.

Figure 36: An enlarged subsection of the internal wave train and an accompanying profile of radar backscatter along the transect highlighted in the interpretation image

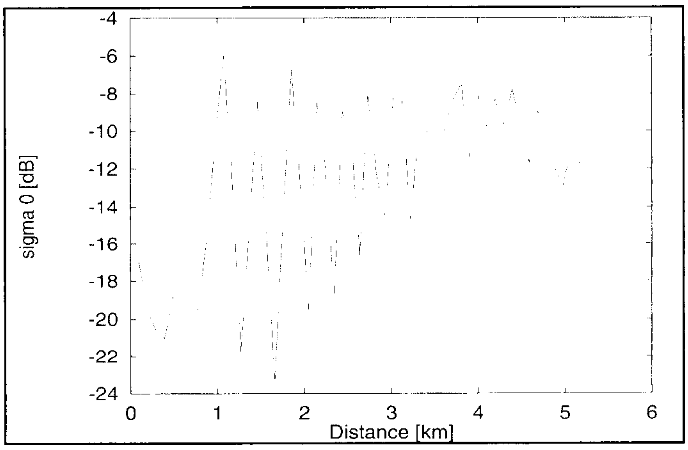

Internal waves are solitary wave trains that are generated mainly by interaction between tidal currents and abrupt topographic features. They propagate near the surface in regions which are stratified. Their surface manifestations are patterns of alternating bands of rough and smooth sea surface [8]. Figure 37 illustrates how the orbital motion of the fluid particles is directed by the internal waves. The motion of the surface water is thought to create a surface signature in one of two ways: either by the accumulation of wave-damping surface-active material at the convergence, or by turbulent ripples generated at a more vigorous convergence. Straightforward dispersion-relation models can provide an approximate framework for extracting useful information from the spatial measurements of internal waves obtained from SAR images. For example, measuring the packet spacing, and assuming a tidal periodicity between them, makes it possible to calculate the wave-group velocity, which enables an estimate to be made of the depth of either the thermocline or the density contrast. This may be obtained from the group velocity C_g,

$$C_g = \sqrt{g \frac{\Delta\rho}{\rho} h_1} \tag{11}$$

where $\Delta\rho$ is the difference between ρ_2 and ρ_1, h_1 is the mixed layer depth (as illustrated in figure 37), and g is the constant of gravitational acceleration.

Figure 37: A sketch of an internal wave showing the fluid-particle velocities and the surface convergence zone; ρ is the density, where $\rho_1 < \rho_2$ and h_1 the mixed layer depth. The vector arrows indicate direction and particle velocity

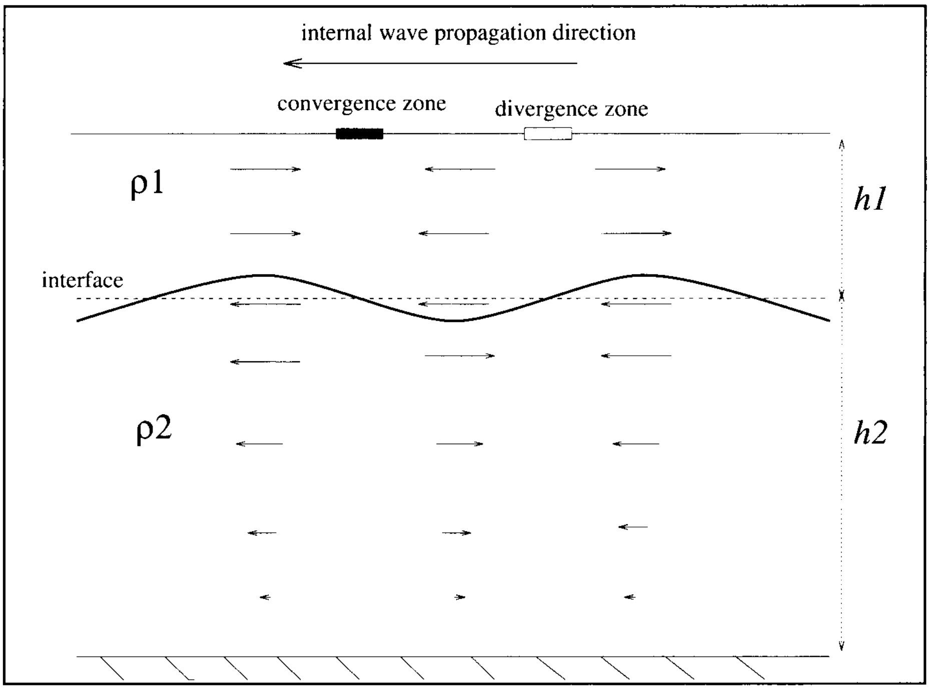

This subimage is a 'blow-up' from the radar image of an area off the west coast of Norway obtained on 6 May 1993 (see page 46). The internal wave train is expressed by the bright, parallel lines which propagate in a northwesterly direction. The dark surrounding area sugests that the wind speed is below threshold (about 3 m/s)

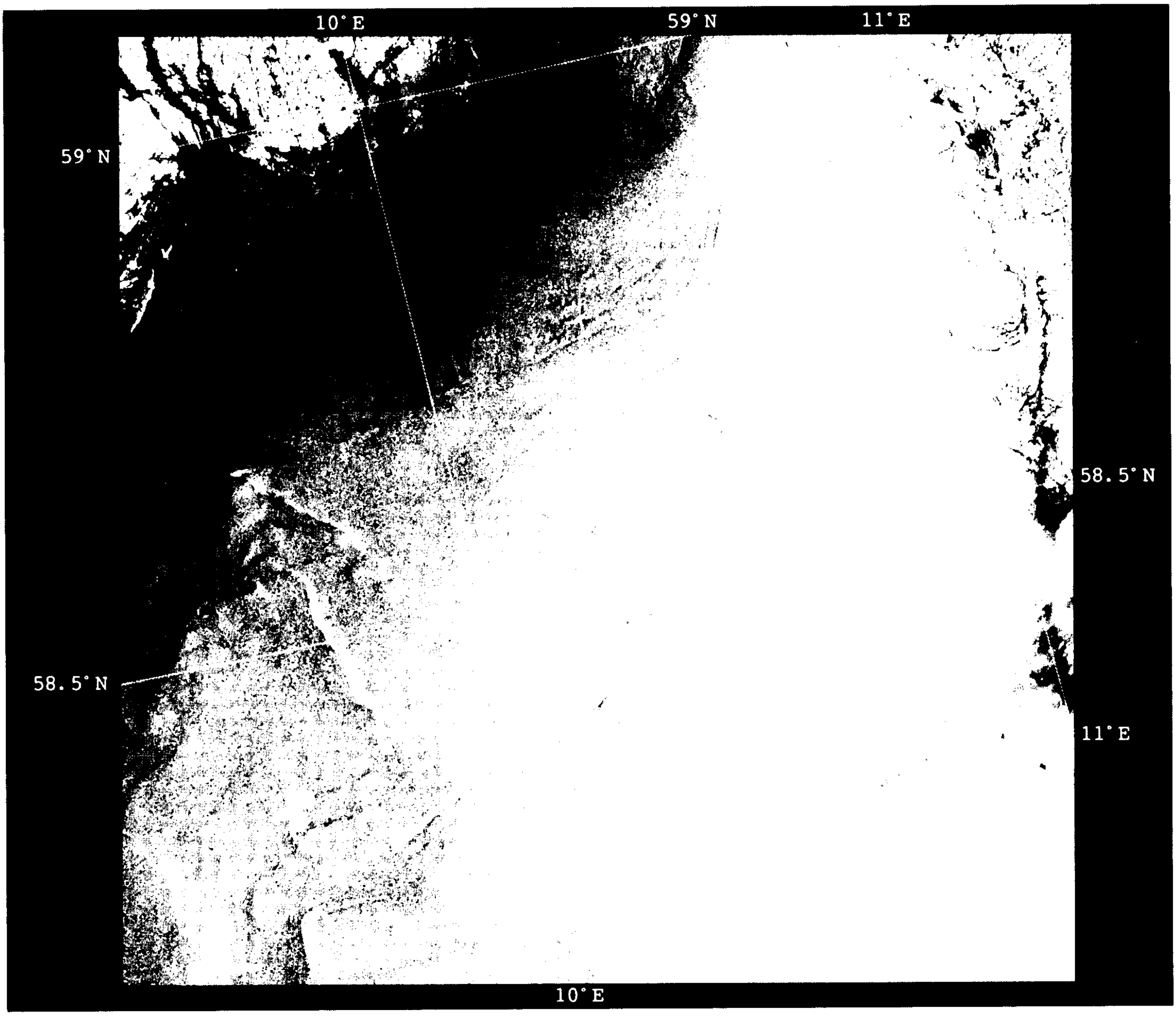

10-05-93

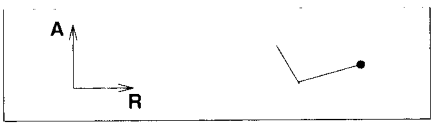

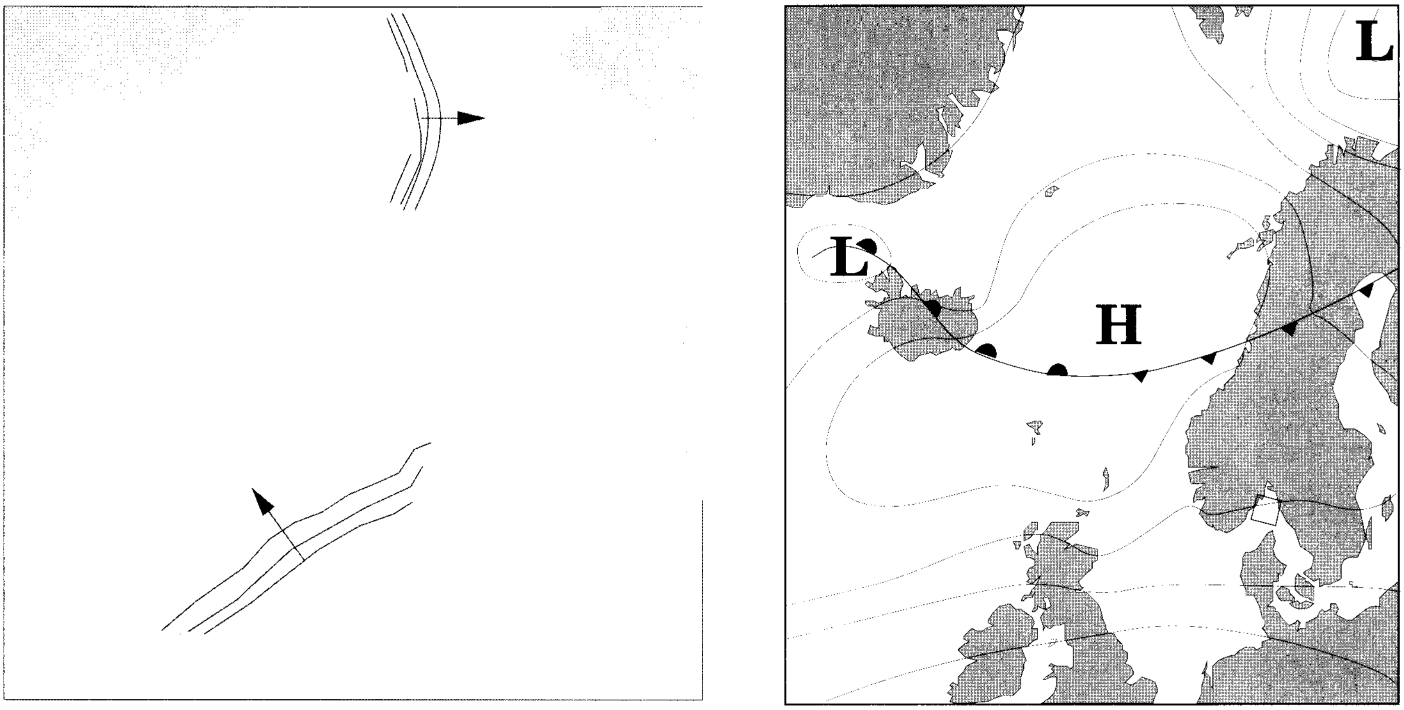

Figure 38: Interpreted image and weather map

The image taken on 10 May 1993 and the next example are both from Oslofjord in southern Norway. This first case illustrates several separate groups of wave packets. The trains do not appear as clearly as in the second example, but the long, gentle arcs of the crests give an indication of individual propagation directions. The local wind velocity at the time of acquisition of this image was 5 m s^{-1} from the east.

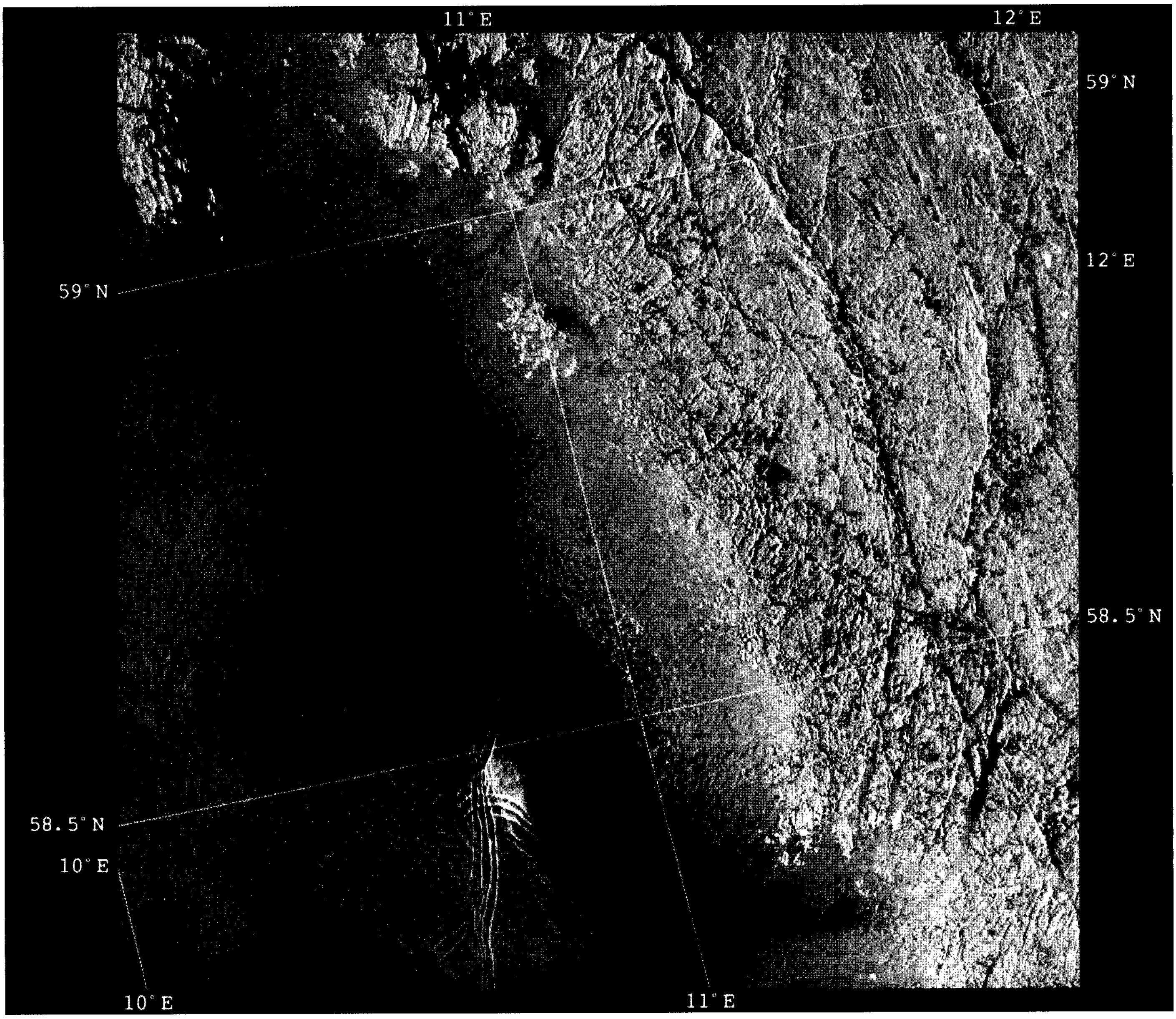

26-05-93

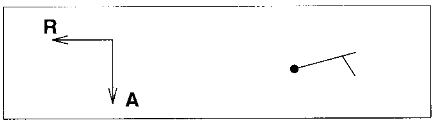

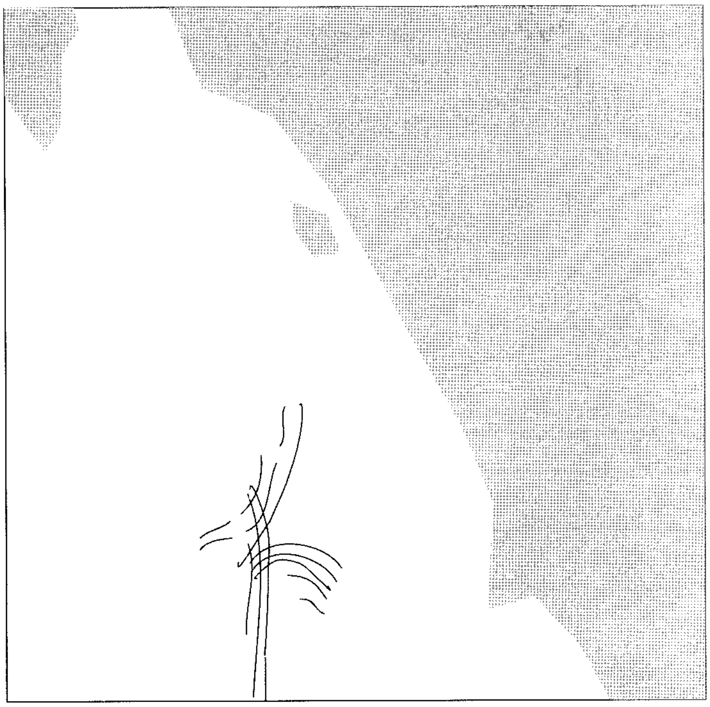

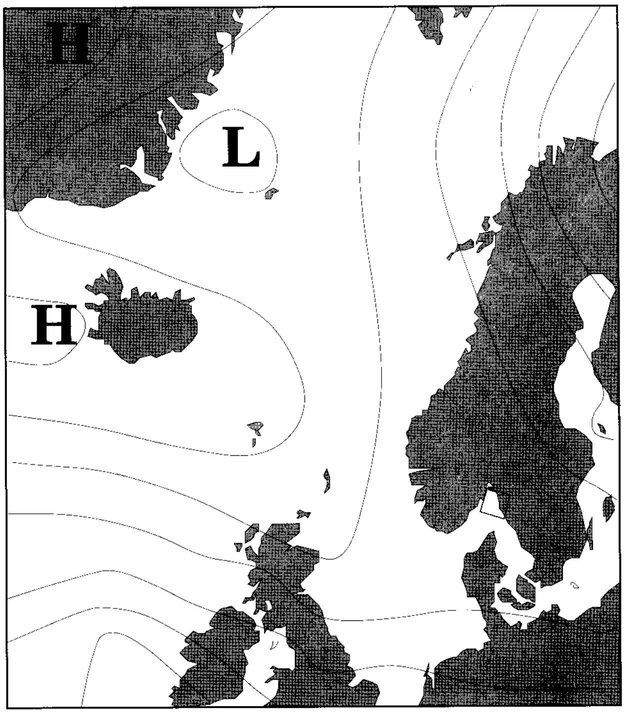

This image, from 26 May 1993, clearly illustrates three trains of internal waves converging on a point in the bottom centre of the image. Up to five crests may be seen in each wave train, and their wavelengths appear to decrease towards the trailing edge of the group. The gentle arc of the lines of surface roughness also indicates the propagation direction. The local wind velocity at the time of acquisition of the image was 2.5 m s^{-1} from the east.

Figure 39: Interpreted image and weather map

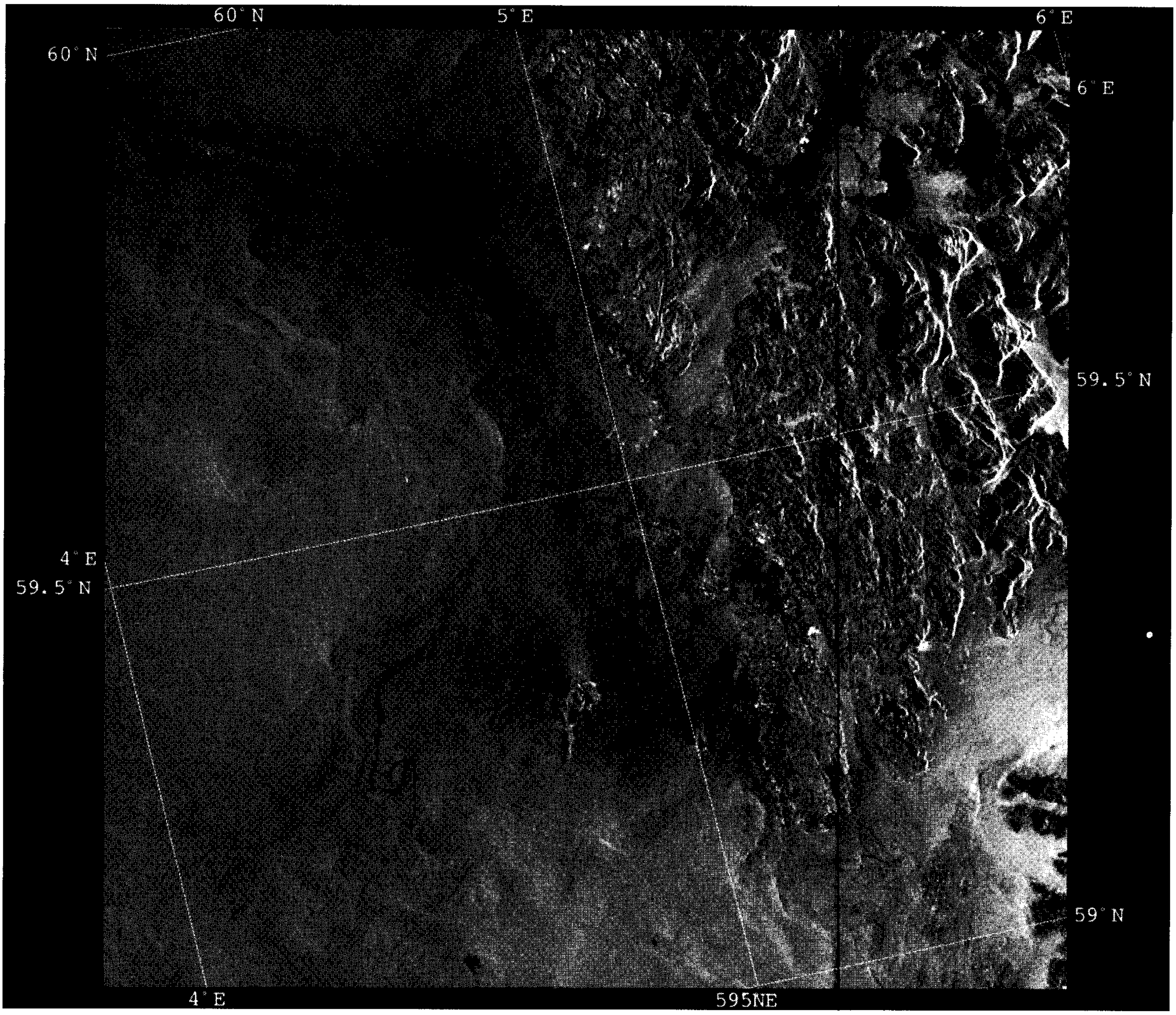

26-06-93

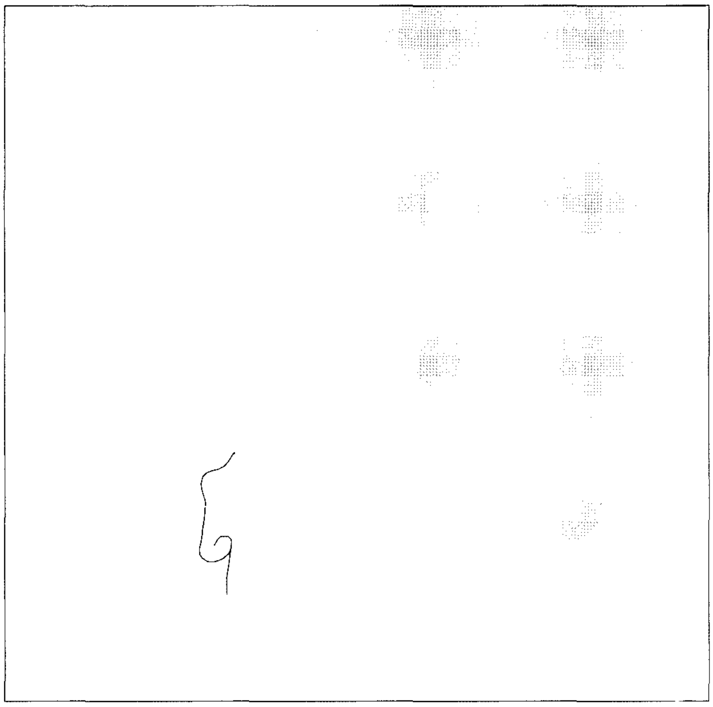

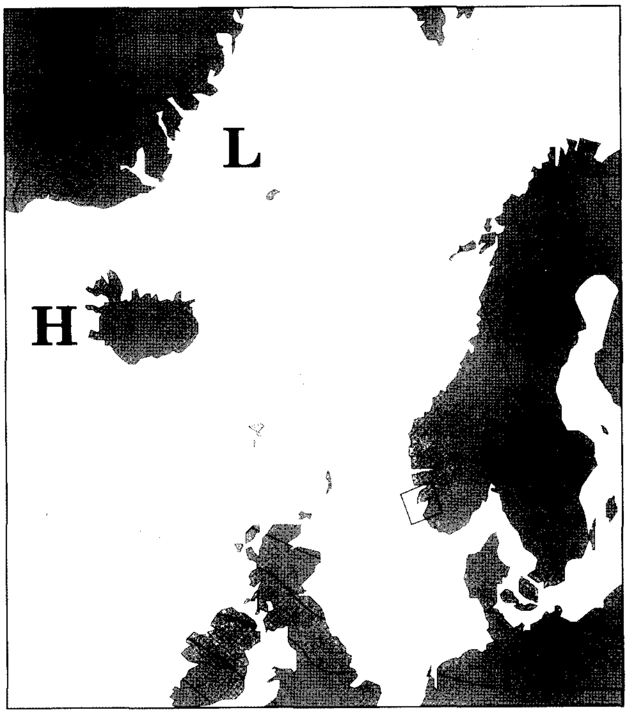

Figure 40: Interpreted image and weather map

3.2.4 Natural films

The very long dark slick in the image has aligned itself with the current shear and is therefore believed to be of natural origin. A natural film has a lower viscosity than oil originating from a man-made spill and it may therefore reconfigure more easily when subjected to currents. Hence, such slicks may give good indications of the circulation patterns in the imaged region. The island Utsira may be seen due east of the slick. The wind speed on 26 May 1993 was 7-8 m s^{-1} from the southeast.

A profile across the slick is shown in Figure 41. The profile illustrates the 5 dB radar backscatter suppression associated with a slick of natural film.

Organic substances secreted by fish and other planktonic species in the upper ocean can under certain oceanographic and meteorological conditions be transported to the surface by rising bubbles, convection, upwelling and diffusion. When they reach the surface, these surfactant biological materials tend to be adsorbed at the air/water interface and remain there as a microlayer. Under relatively calm conditions, this microlayer can form uniformly over extensive areas of ocean. Accumulation may take place in regions of high biological activity, i.e. in coastal regions, in regions of upwelling [2,28] and along current boundaries [21].

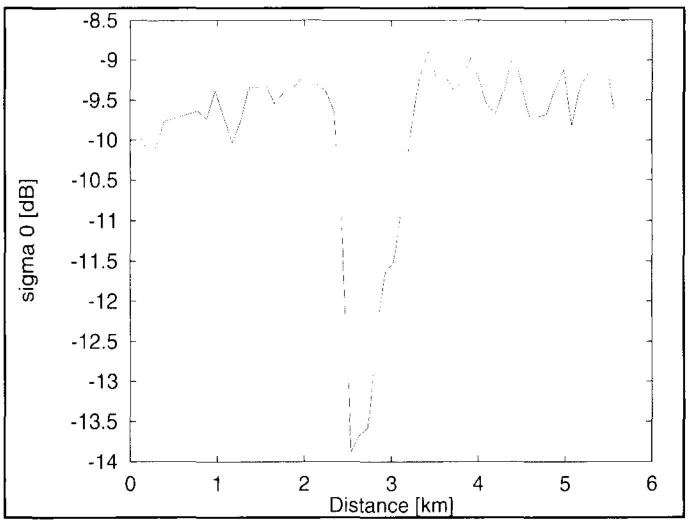

Figure 41: Backscatter cross section across the slick in the image

Waves propagating across a film-covered surface will cause compression and dilation of the film [12]. This gives rise to surface-tension gradients, which in turn bring about vertical velocity gradients within the surface layers where the film is present. Increased viscous damping is induced, so the short Bragg waves are attenuated and the scattered signals returning to the SAR are significantly reduced.

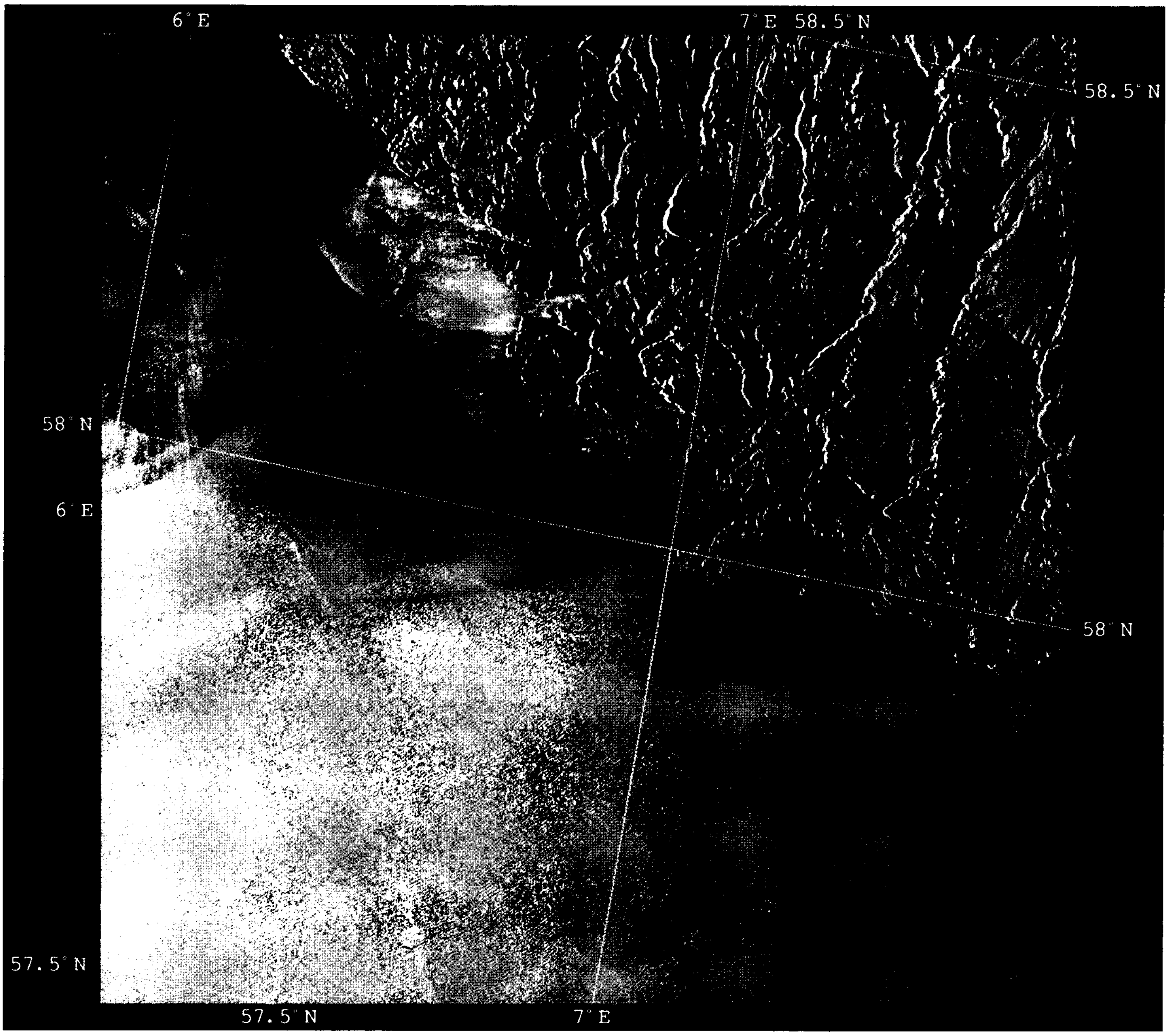

28-04-93

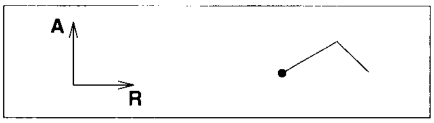

The radar cross section value of a slick-covered area may be as much as 80% lower than that of the surrounding water, implying that up to 80% of the energy of the surface wave component corresponding to Bragg conditions may be lost by damping effects. This is, however, very dependent on wind speed [7].

Natural films are usually dissolved at wind velocities above 7 m s^{-1} [34] and, because they are easily broken up by currents, including both shear and convergence, such slicks easily configure into spatial variations that are related to the surface current circulation pattern [16,18]. This will in turn make it possible to detect the surface current circulation pattern in a way similar to that discussed above in connection with eddy orbital motion, internal waves and jets.

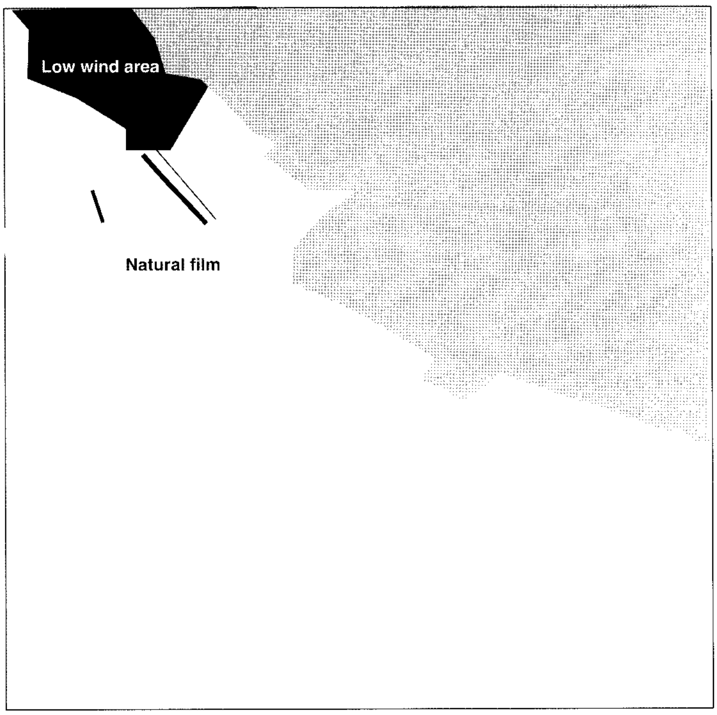

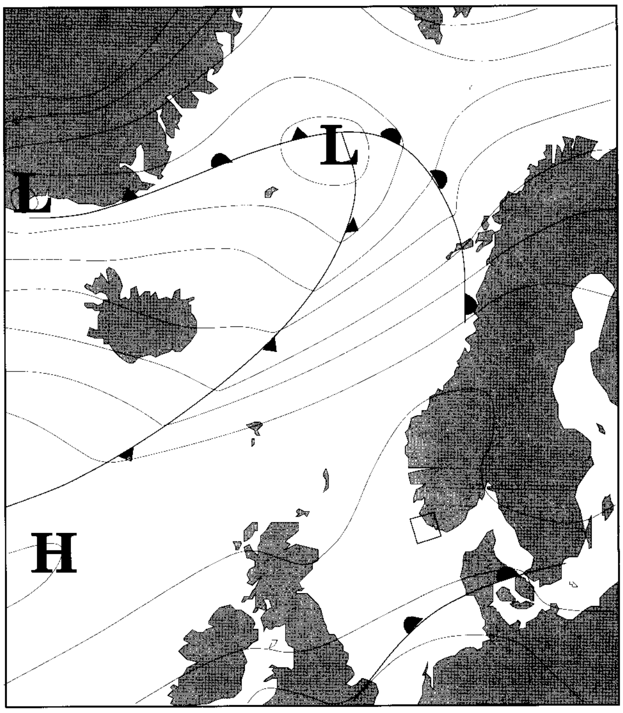

Figure 42: Interpreted image and weather map

This image, taken on 28 april 1993, and the following one are from an area close to the southern coast of Norway near Lista. The wind speed at the time of acquisition measured $5 \mathrm{~m} \mathrm{~s}^{-1}$ from the northeast. The two long dark strips (thick lines in the interpretation image) in the top left-hand part of the image occur close to a region where the wind must have been so low that it had fallen below the SAR imaging capability (less than 2-3 $\mathrm{m} \mathrm{~s}^{-1}$) and created a large dark region. This may be caused by wind sheltering by land. The slicks in this low-wind-speed area have aligned themselves parallel with what could be a bright current shear or a convergence zone (thin line in interpretation image). It is for this reason that the dark lines are believed to represent natural film.

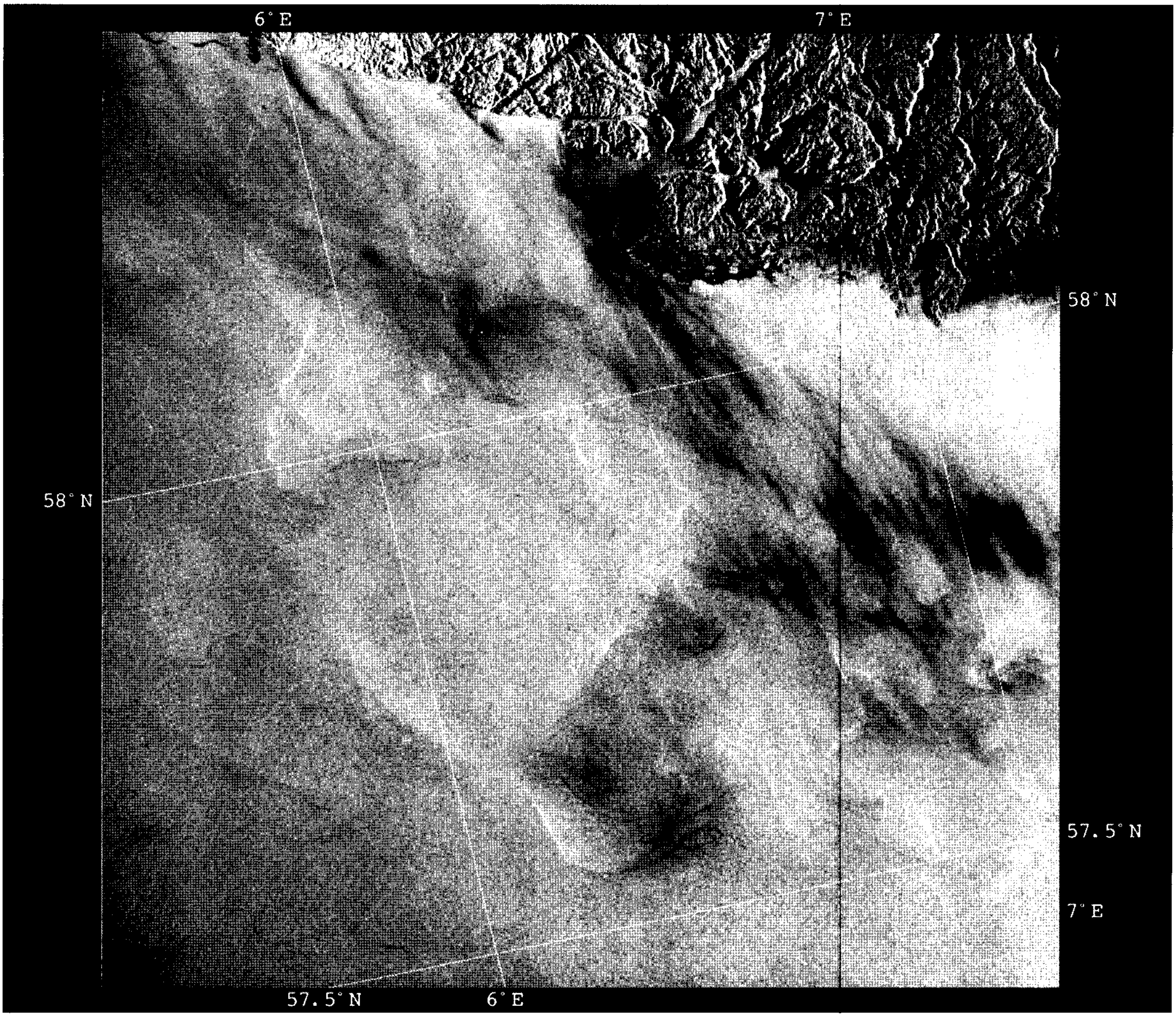

04-06-93

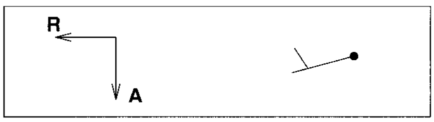

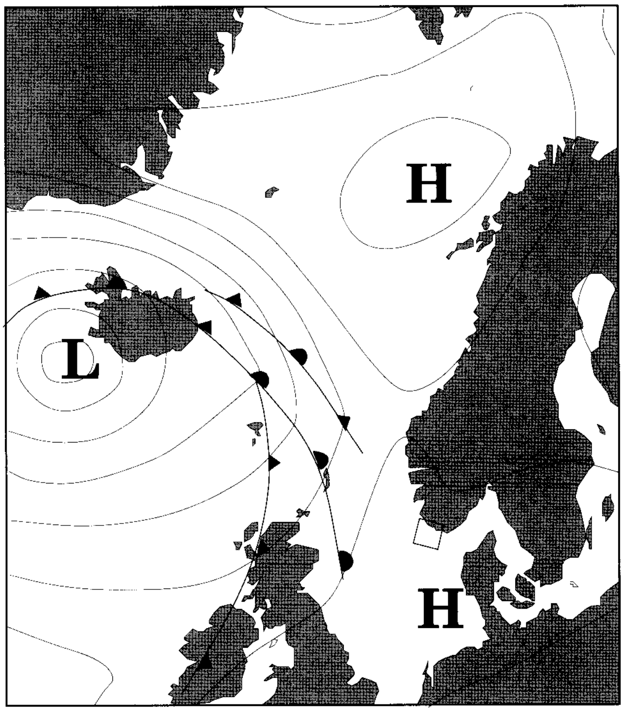

In this image, from 4 June 1993, several areas of natural film may be seen offshore. The two dark slicks in the top left-hand corner of the image frame could be either oil spill from a ship cleaning its tanks or natural film. The slicks were classified as of natural origin because of their form, which indicated that they had drifted with the currents in this low-wind-speed area. Close to the coast, two large regions of wind sheltering are apparent. The synoptic wind record close to the time of acquisition was 2-3 m s^{-1} from the west.

Figure 43: Interpreted image and weather map

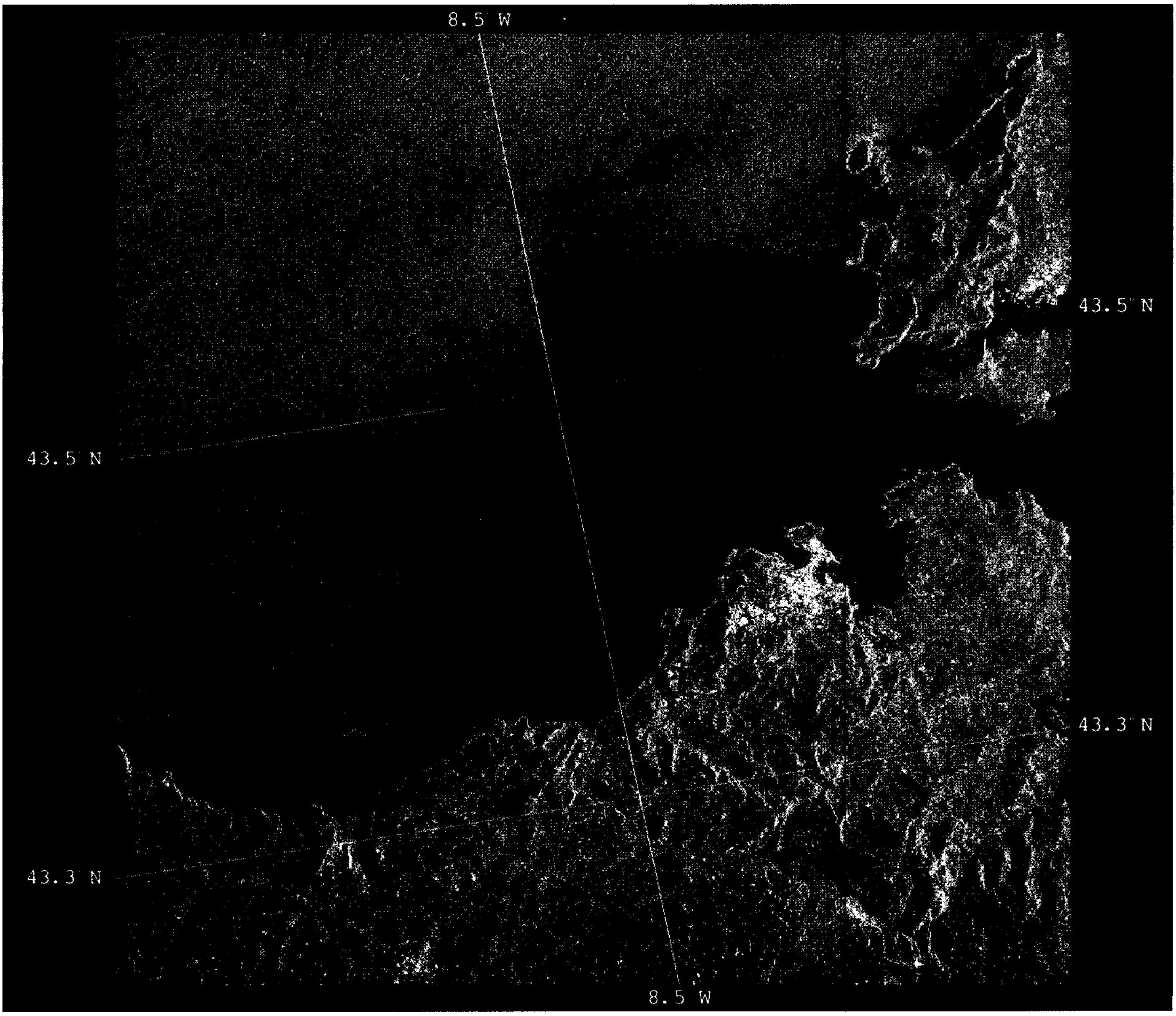

13-12-92

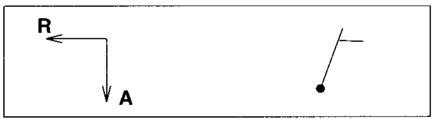

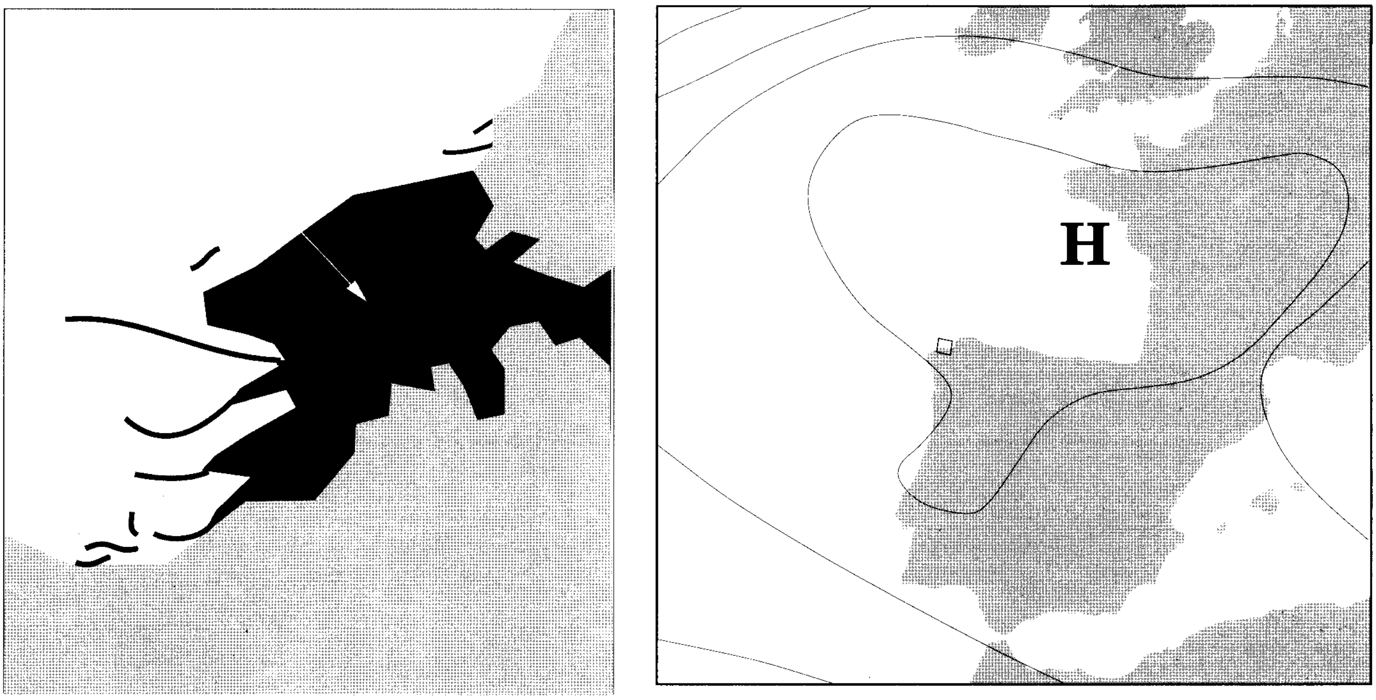

3.2.5 Oil spills

Figure 44: Interpreted image and weather map

The ERS-1 SAR image of the bay of La Coruña, Spain, was acquired on 13 December 1992, 10 days after the oil tanker 'Aegean Sea' had been wrecked (43). In the days after the accident, the winds were light and from the southwest, turning northwesterly on 7 December with a maximum wind speed of 23 m s^{-1}. From December 10 to 12, the wind blew from the northeast with a wind speed not exceeding 13 m s^{-1}. In the SAR image, the dark areas in the bay may be caused by low winds (less than 3 m s^{-1}), but observations made from helicopters indicate that the 70 000 tons of crude oil spilt during the accident polluted the whole bay. Outside the bay, the wind speed is higher than 3 m s^{-1}, and the dark areas along the coast north of the bay may indicate that some of the oil has drifted northeastward during the first period when the winds came from the south. This ERS-1 SAR image covers an area of 50 × 50 km.

A profile from clean to oil-covered surface is shown in Figure 45. The oil causes a 14 dB decrease in backscatter.

Large oil spills at sea may cause considerable damage to the environment, especially if they occur close to the coast. Man-made oil spills originate from;
— Releases from ships, e.g. during cleaning of oil tanks;
— Offshore oil installations;
— Ship accidents.

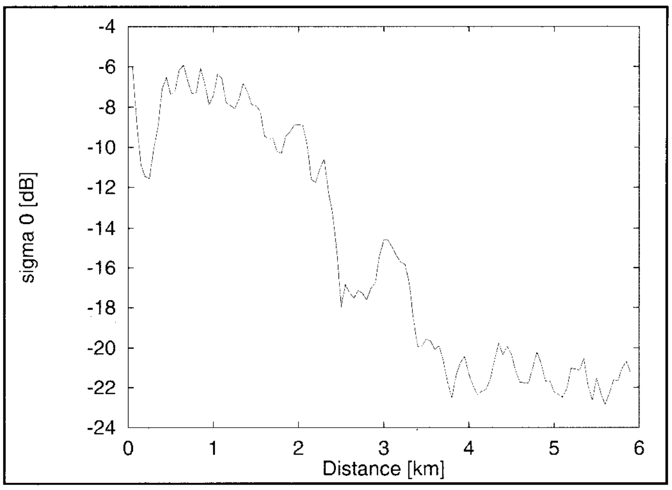

Figure 45: Profile of radar backscatter across edge of oil spill

Spaceborne SAR may contribute to an oil-spill detection and monitoring system, by supplying early warnings and drift surveillance. In the case of accidents, the spill is likely to be reported and the SAR may be used to keep track of the drift and spread of the oil slick. However, illegal oil spills from ships cleaning their tanks may prove to be a much worse source of pollution. If SAR images are to become useful for

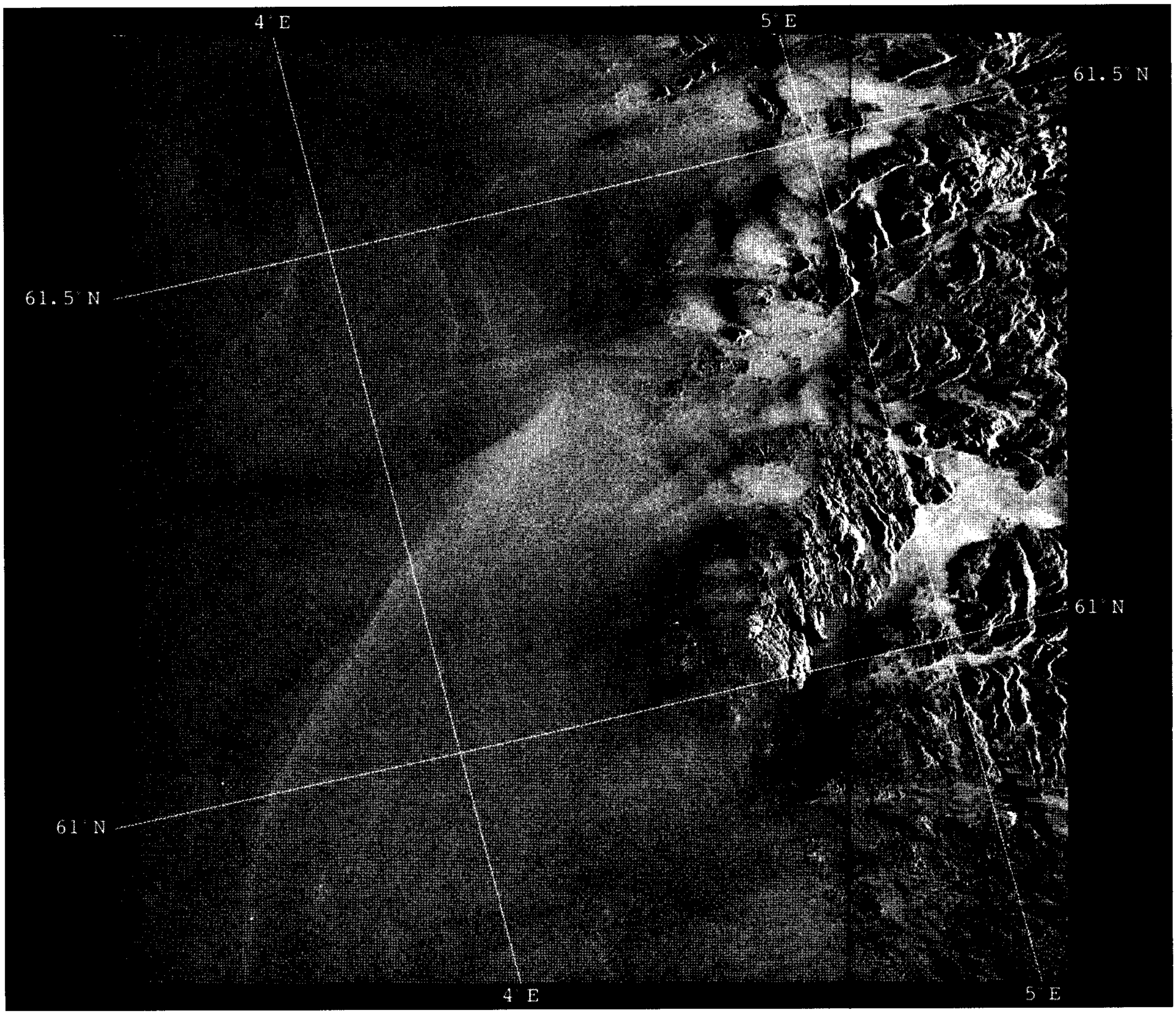

22-09-92

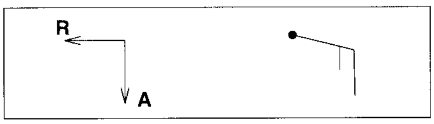

detecting such spills, slicks resembling oil spills need to be studied and understood thoroughly [16]. The main limitation at present is the difficulty experienced in distinguishing between oil slicks and natural films produced by plants and animals in the ocean. Such films reduce the radar backscatter by similar amounts, and generally have the same shapes and sizes.

Another limitation is the fact that oil-spill monitoring employing satellite-based SAR data is limited by an upper (10-12 m s^{-1}) and a lower (2-3 m s^{-1}) wind speed. Below 2-3 m s^{-1}, SAR images of the ocean become dark because the Bragg scattering waves are not present. In this case, it is almost impossible to distinguish different features on the sea surface. Above 10 m s^{-1} most kinds of oil are dispersed into the water column by the wind waves [6], although they can re-appear at the surface during subsequent calm weather.

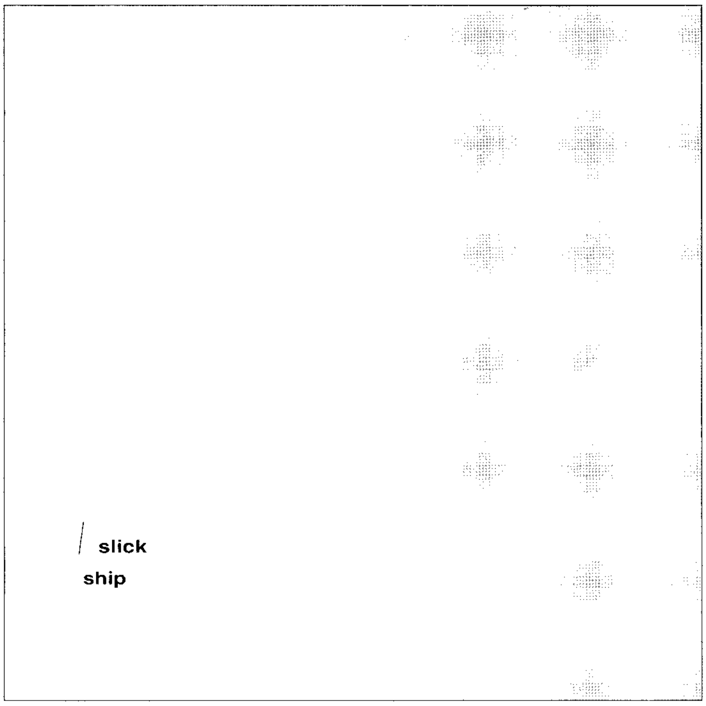

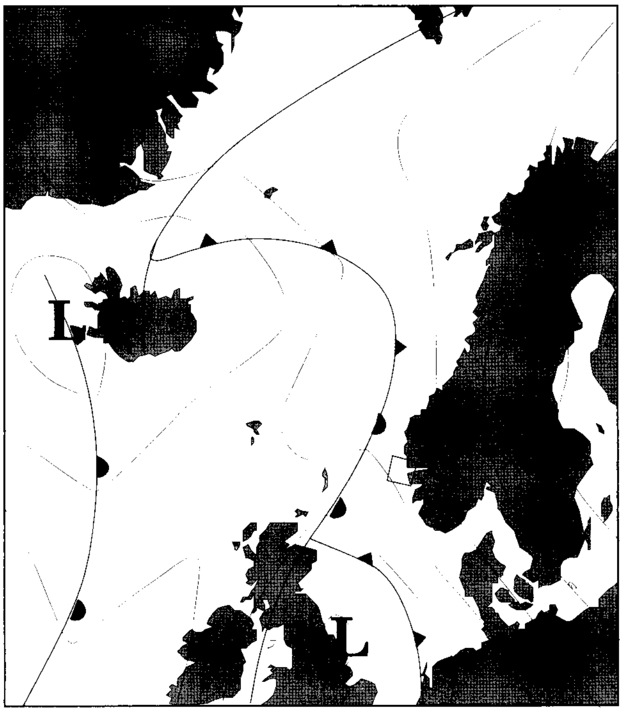

Figure 46: Interpreted images and weather map

This image, acquired off the coast of Sogn in western Norway on 22 September 1992, shows what is believed to be a ship spilling oil. In the blow-up in Figure 47, the ship can be seen as a bright point and the spill appears as a dark band behind the ship. The reason for not interpreting the dark feature as a wake is that wakes are usually straight lines unless the ship has changed its heading. But even if this ship had changed course, it would be very unlikely to have such a long (4 km) winding wake as is seen here. Measurements indicate a wind speed of approximately 5 m s^{-1} from the east.

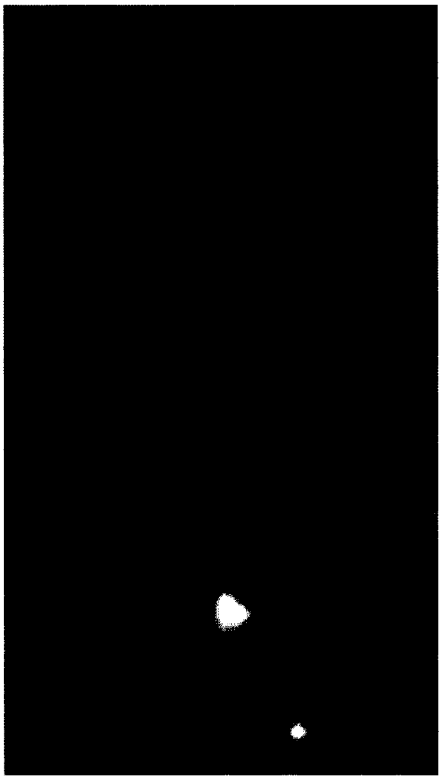

Figure 47: Enlarged section of the image from 22 September. It shows a bright backscatter signal from a ship and possibly a slick of oil

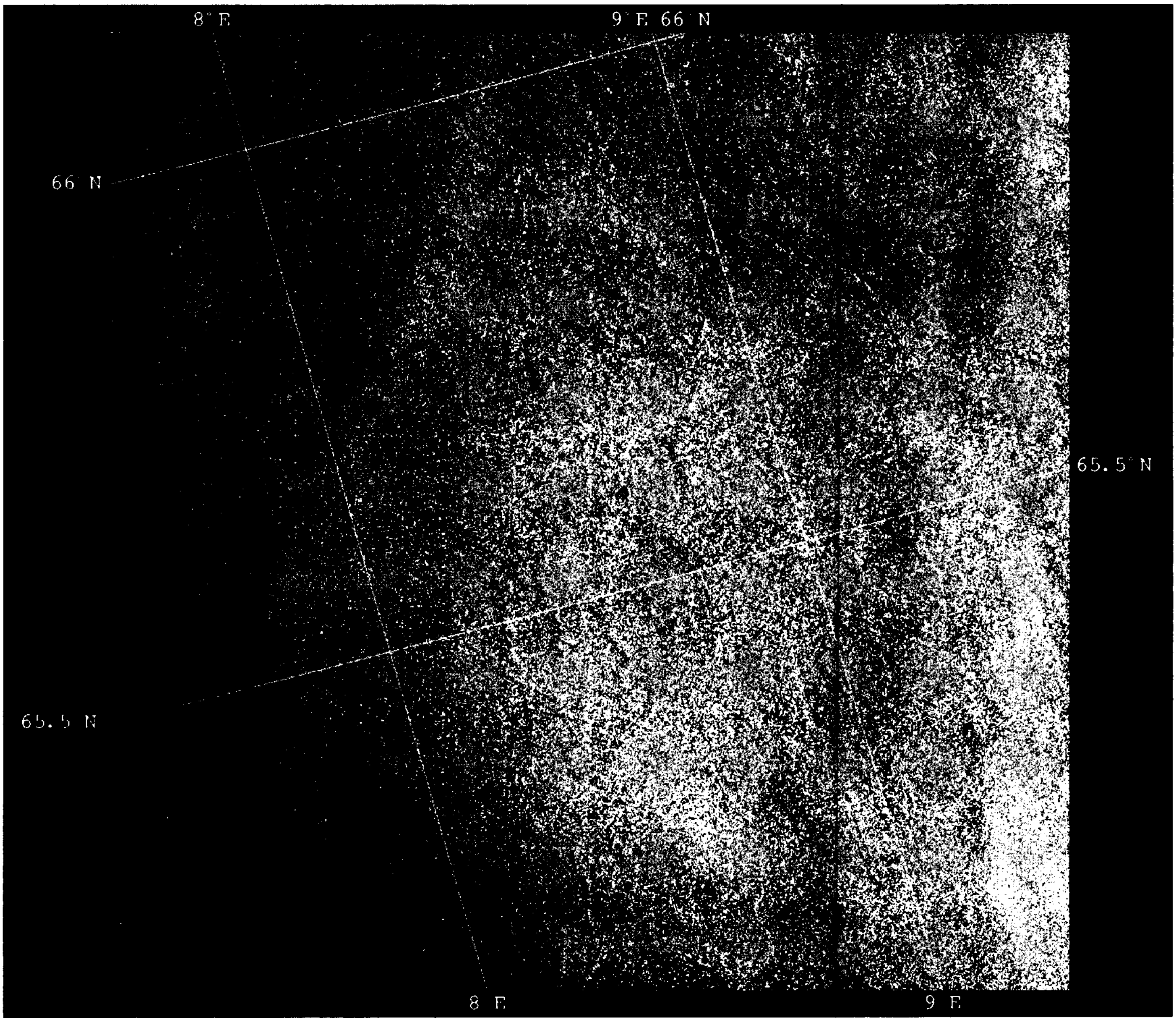

09-10-93

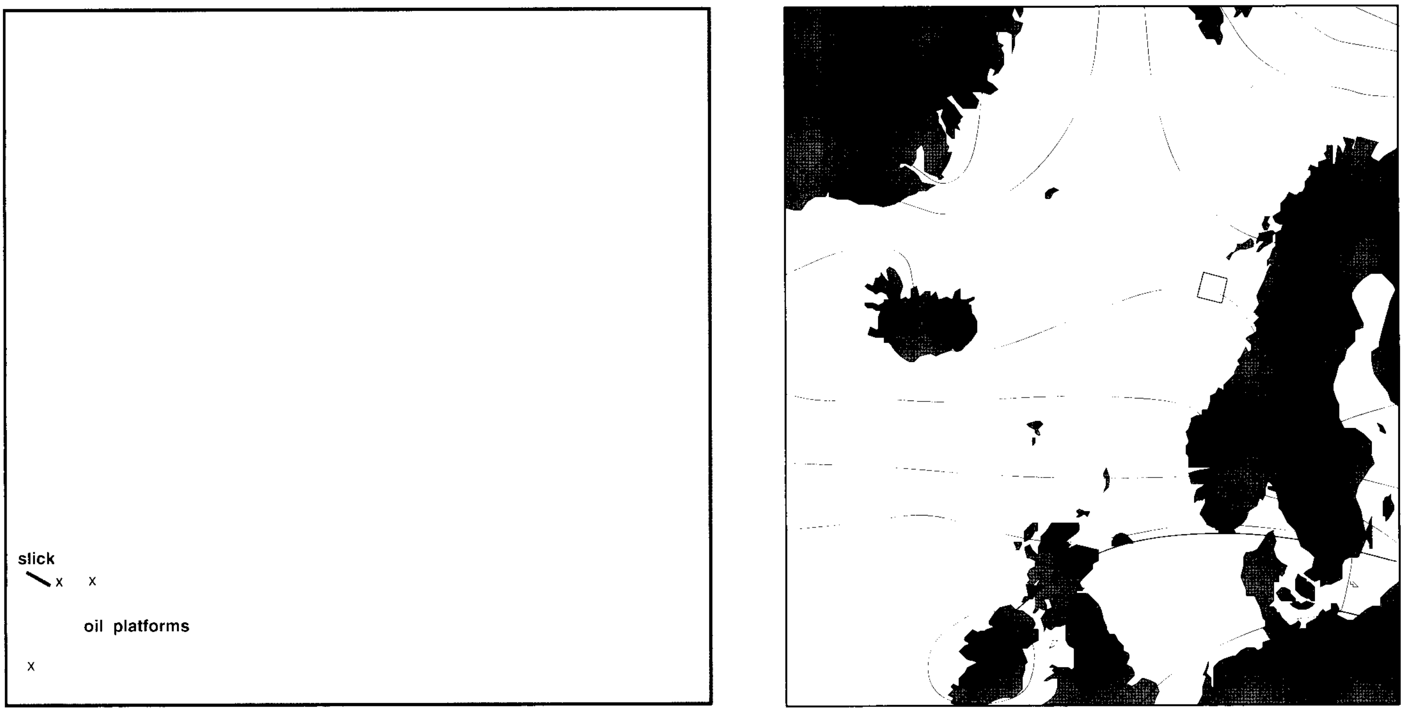

Figure 48: Interpreted image and weather map

In the bottom left of this image, from 9 October 1993, a spill can be seen at the Heidrun oil field. An enlarged section of the image is shown in Figure 49. The spill consisted of 274 m^3 of drilling fluid and came from the oil drilling platform that can be seen as a bright point nearby [40]. The spill was released into the ocean within a day of the SAR overpass, but the very low wind speed of about 2.5 $m\,s^{-1}$ (from the northeast) made it possible for the spill to remain at the surface.

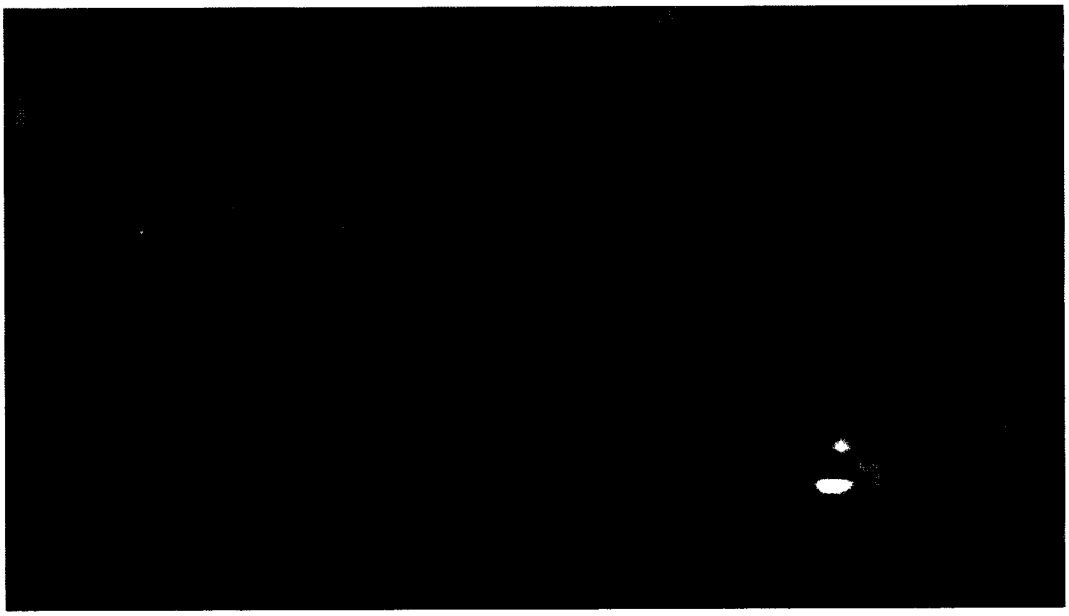

Figure 49: Enlarged section of the image from 9 October 1993

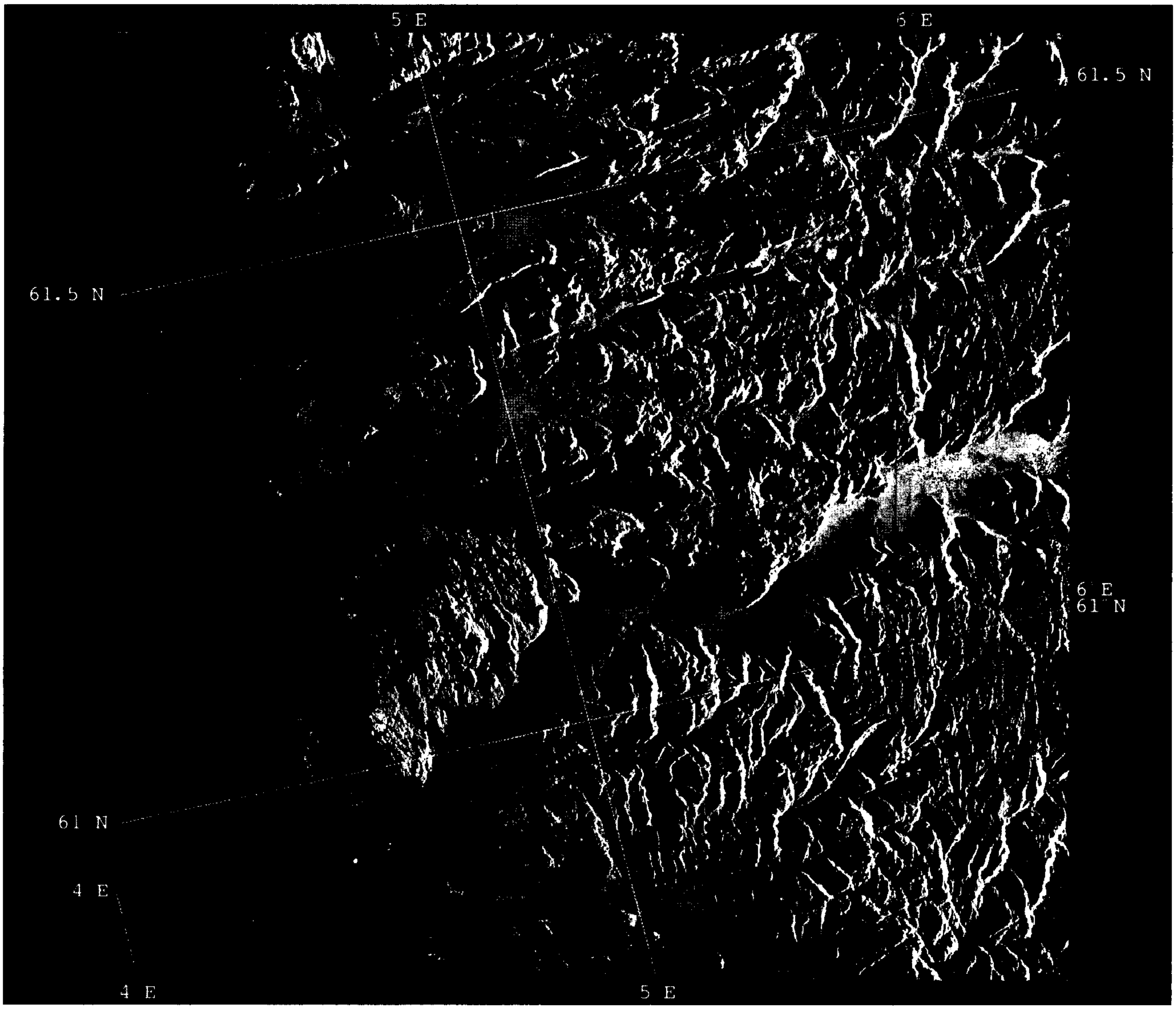

06-05-93

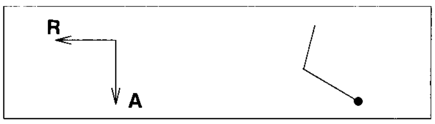

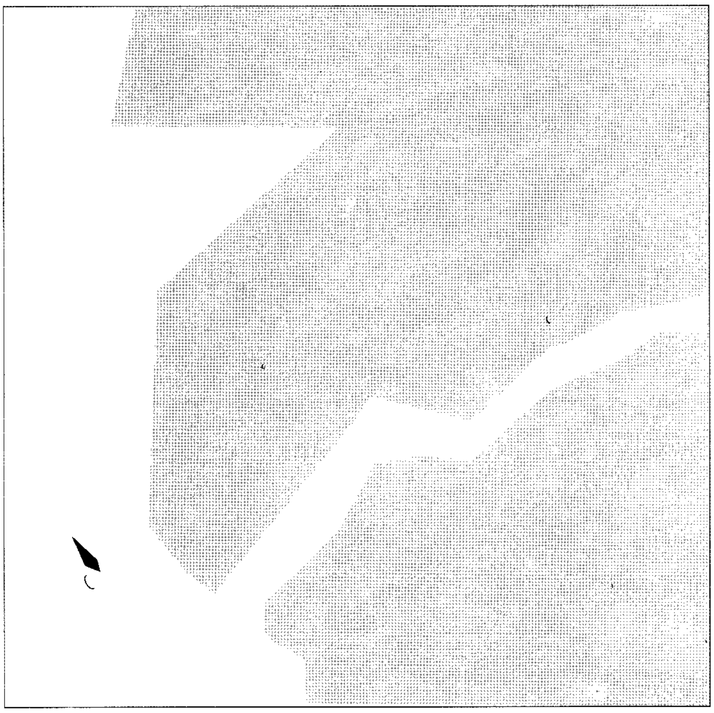

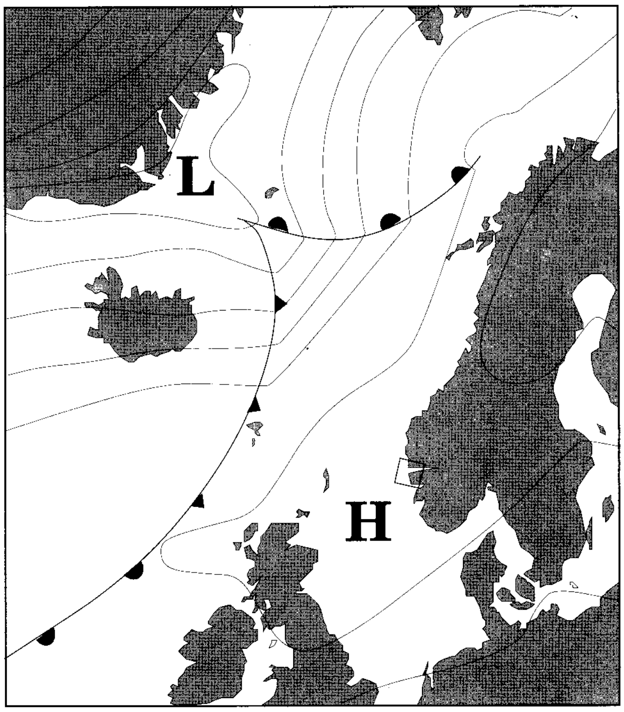

Figure 50: Interpreted image and weather map

The two dark slicks in this image from the coast of Sogn caused the Norwegian Defence Research Establishment (NDRE) to forward an alarm to the Norwegian State Pollution Control Authority (SFT). An ongoing ERS-1 project 'Oil Spill Detection Using Satellite Based SAR' made it possible for SFT to use its surveillance aircraft to check the oil spill alarms based on ERS-1 images interpreted at NDRE [40]. SFT was able to confirm the alarm. The dark slicks were caused by a mixture of diesel oil and fish oil.

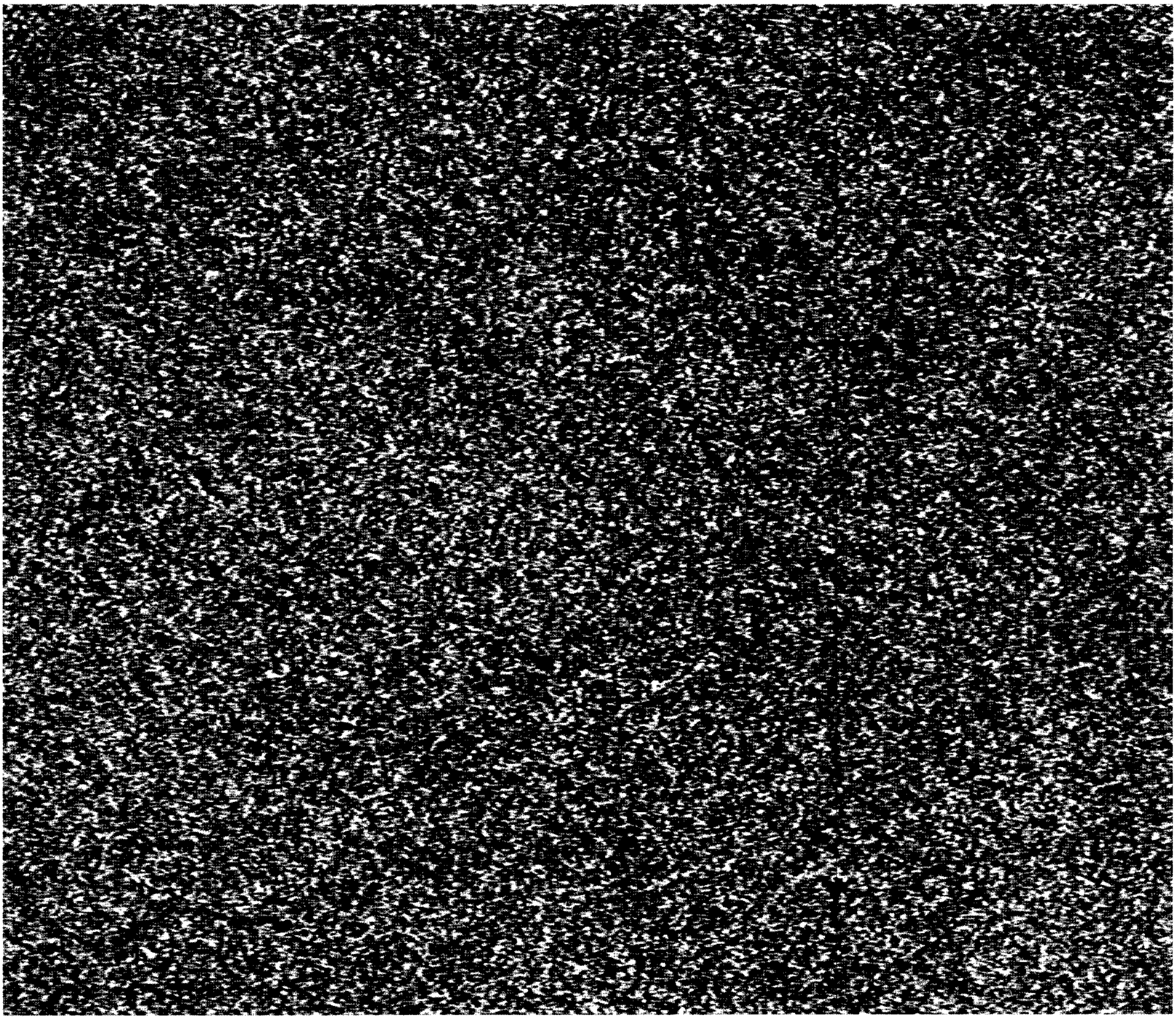

20-11-91

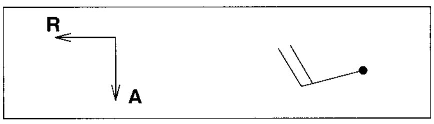

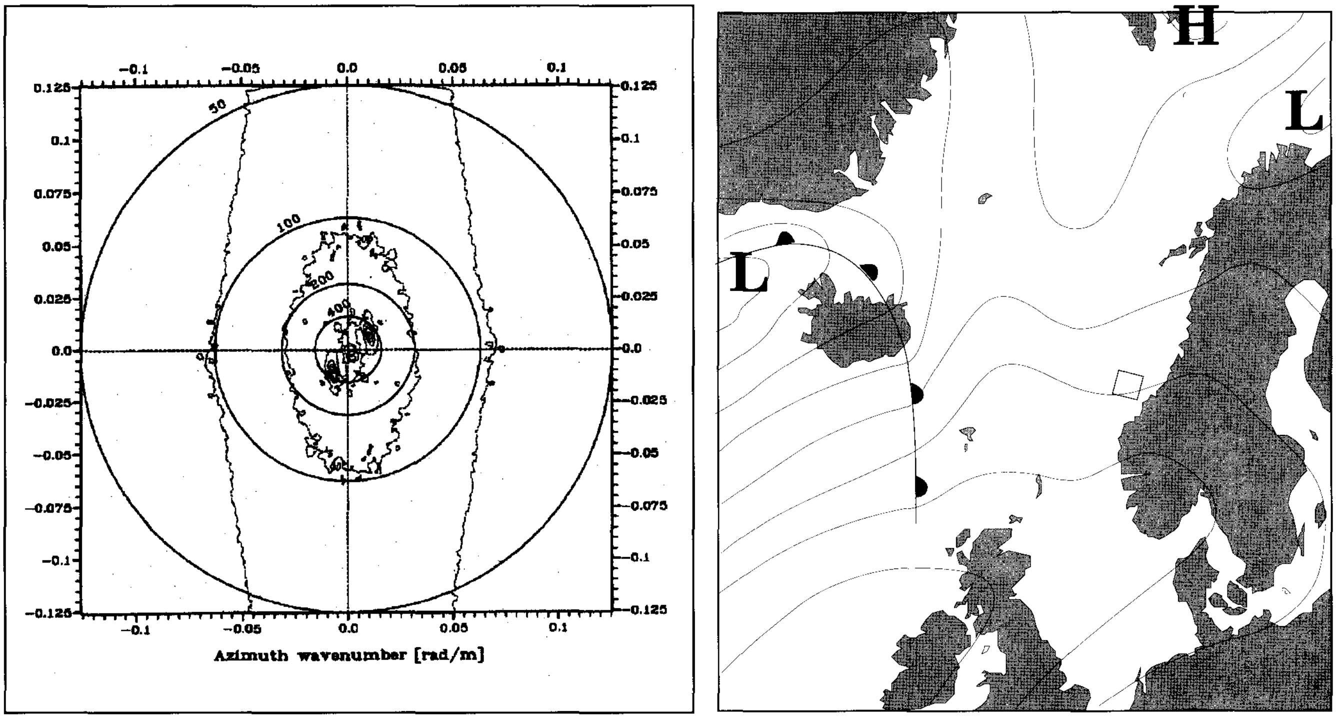

3.3 Surface wind waves and swell

Figure 51: Wave spectrum and weather map

The ERS-1 SAR image, from 20 November 1991, is of an area off the coast of Norway. It is a 1024 × 1024 pixel subscene of the full-resolution version of the image shown in Section 3.1.4. The corresponding SAR image spectrum shows several characteristic features. First, spectral peaks associated with the wave mode are present. Second, the spectral energy is restricted to a narrow azimuth passband. The passband is a direct consequence of velocity-bunching nonlinearity and coherence-time limitation. Any wave modes that lie outside the passband will not be imaged at all or will have their imaged energy shifted into the passband in a nonlinear manner. As a rule-of-thumb, the ERS-1 SAR will not accurately image azimuth traveling waves that are shorter than 200 m in wavelength.

A SAR creates a high-resolution image by recording the phase and amplitude of electromagnetic radiation reflected from the scatterers in the scene, and subsequently processing this information by means of a compression filter. The phase results from the relative motion between the platform and each scatterer in the scene. For a static point target, the phase is a deterministic function and the compression filter is designed to match the phase perfectly. For the dynamic ocean surface, the motion of each scatterer within the scene distorts the expected phase function with two important results. First, the linear component of the target motion causes an azimuth shift of the imaged location of each target [30]. Thus, periodic forward and backward shifting of imaged scatterer positions due to the wave orbital motion leads to strong wavelike modulations in the SAR image [36]. This imaging mechanism is termed velocity bunching and is nonlinear, becoming more nonlinear as the ratio of scene range to platform velocity (R/V) increases [14]. Secondly, higher-order components of the target motion result in a coherence time limitation which degrades the SAR's azimuth resolution with respect to that expected for a static point target [31]. The degradation in resolution becomes greater as R/V increases. The scene motion due to the presence of ocean waves sets up a competitive process: wave image formation due to velocity bunching and image degradation due to the coherence time limitation. For the ERS-1

SAR $R/V \approx 115$ s, which is fixed by the choice of orbit. An R/V of this magnitude is acknowledged to be too large for a SAR accurately to image an arbitrary ocean wave system.

The quantitative utilisation of ERS-1 SAR image spectra is difficult. However, development of the Hasselmann transform [13,25], which analytically represents the mapping of an ocean wave spectrum into a SAR image spectrum, represented a signficant advance in our understanding of the imaging process, and has led to the inversion of SAR image spectra into ocean wave spectra. SAR inversion is usually based on the iterative minimisation of a cost function and requires a model wave spectrum as a starting point. Of course, useful ocean wave information cannot be derived for regions of the spectrum that lie outside the azimuth passband, and the initial model spectrum must be relied upon for that information. Inversion of ERS-1 SAR spectra into ocean wave spectra is now quite routine. Experiments and demonstration projects are being carried out in which SAR-derived ocean wave information is being assimilated into wave models. The ERS-1 SAR is particularly useful for updating swell (long wavelength) information. Global sets of SAR image spectra, for wave model assimilation are available from ERS-1's wave mode.

4. Time series

4.1 Daily/weekly

The following timeseries is from the ERS-1 commissioning phase in 1991. The satellite was then operated in a three-day repeat cycle, and NERSC conducted an ERS-1 validation study off the coast of Norway [19]. The frame of the SAR scenes is shown in a geocoded map of the experimental region in Figure 52.

The received SAR scenes had varying azimuth start positions and have been cut to fit the frame in Figure 52. A few of the images will therefore be lacking some of their data. Most of the images were received at the Tromsø Satellite Station, but the image from 1 November is a fast delivery copy from the Kiruna station. The image was histogram equalised, which accounts for its slightly different appearance.

An interpretation figure, including a wind arrow, is shown to the right of each image. The figures shows that in almost half the images, a current front is seen in the channel between the coast and the bank in the upper right-hand corner in Figure 52. In general, the Norwegian Coastal Current (NCC) is steered northeastward through this channel, while a weak anticyclonic flow of mostly Atlantic water usually appears to be trapped on the bank. In turn, a current front with cyclonic current shear is formed at the boundary between the two characteristic water masses [15]. A complete analysis of these images for application in a study of coastal oceanographic and atmospheric boundary-layer processes is given in Johannessen el al. [20] and Rufenach et al. [32].

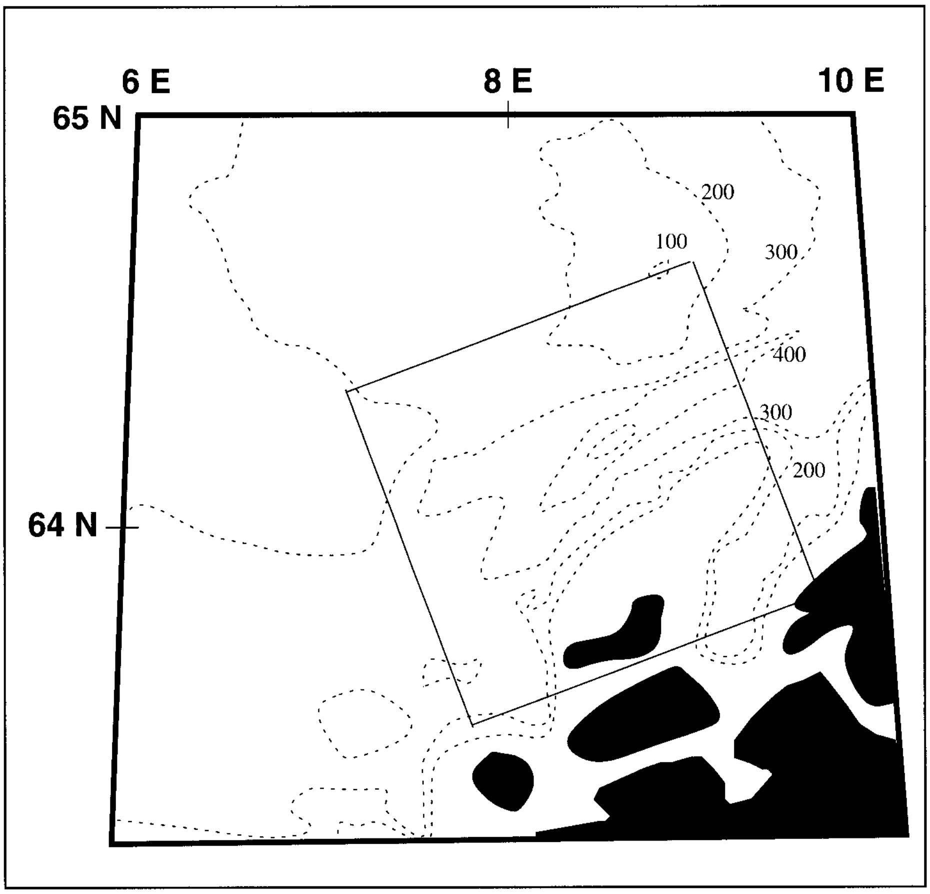

Figure 52: A map of the bathymetry in the region. The box indicates the position of the SAR frames

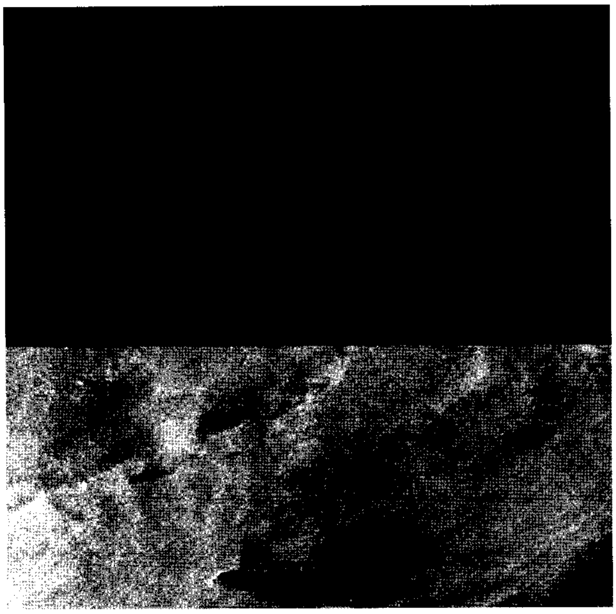

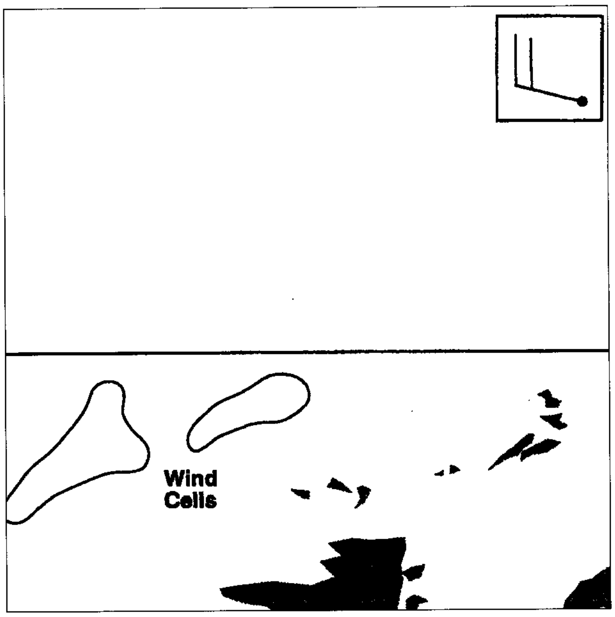

20-10-91

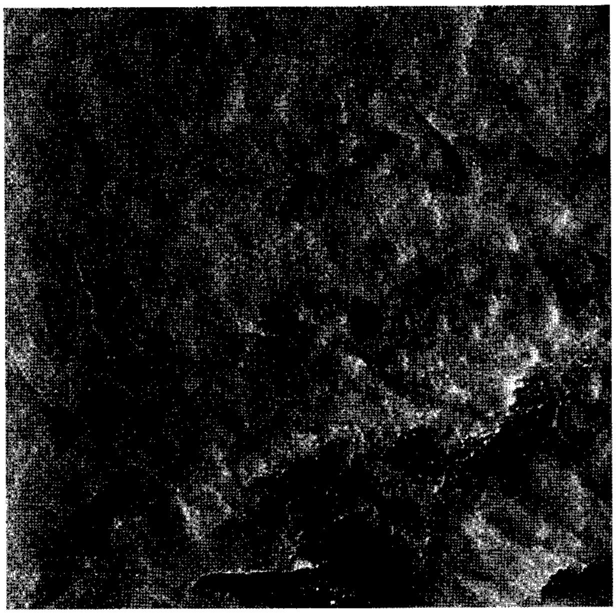

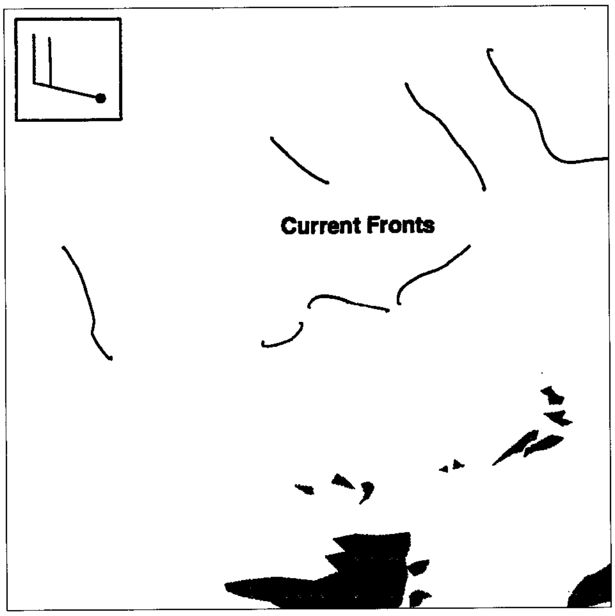

23-10-91

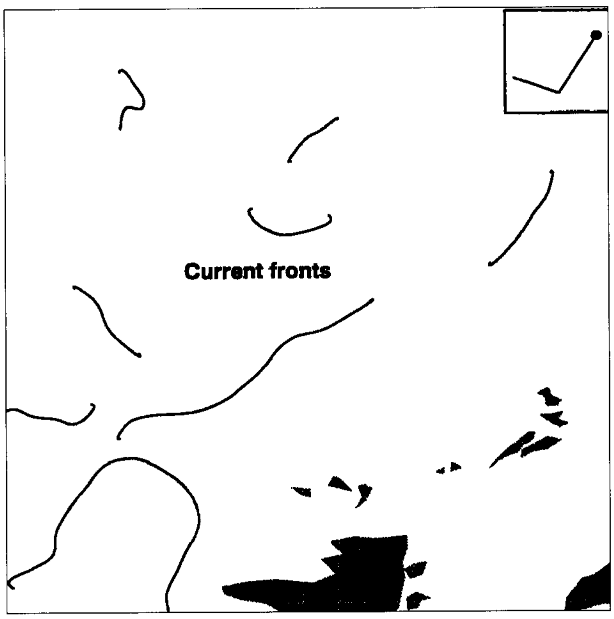

26-10-91

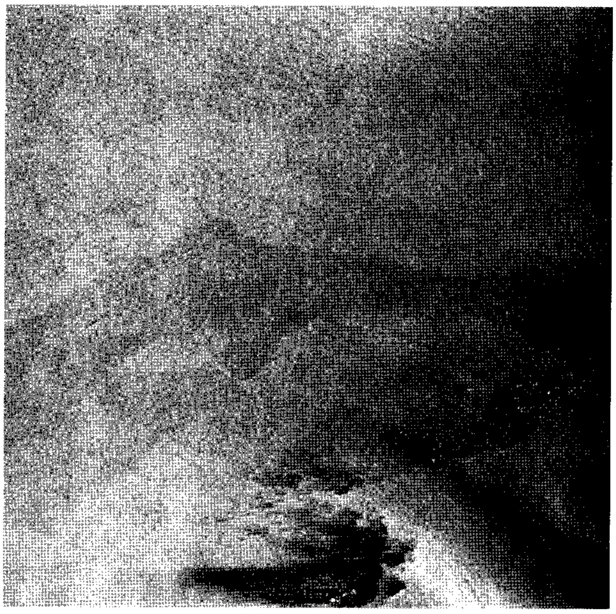

29-10-91

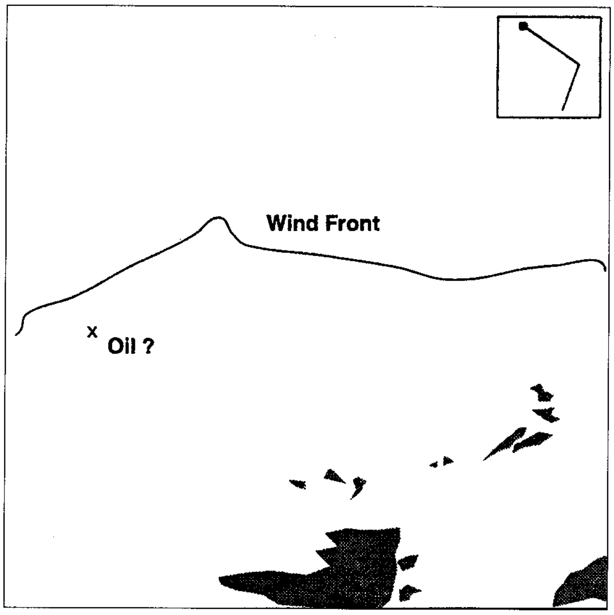

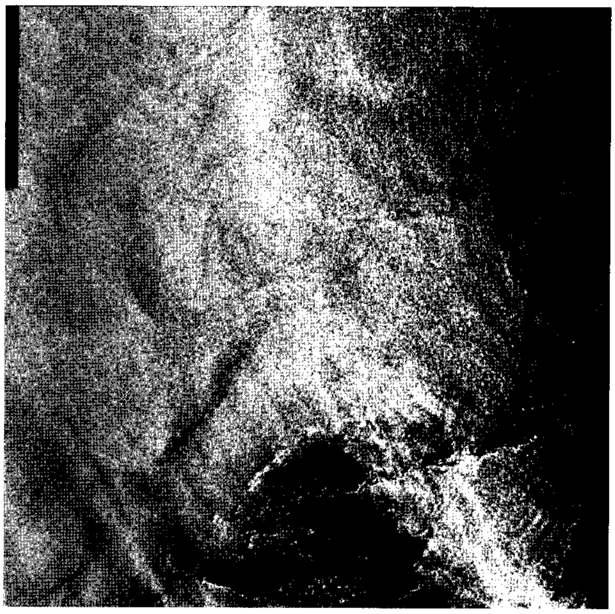

01-11-91

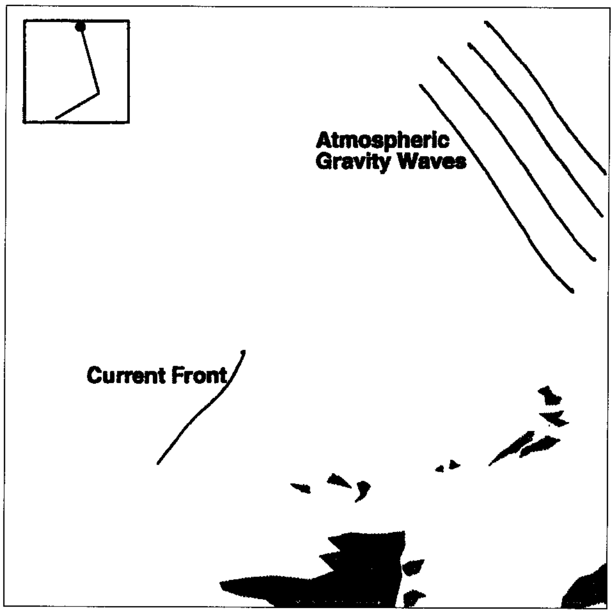

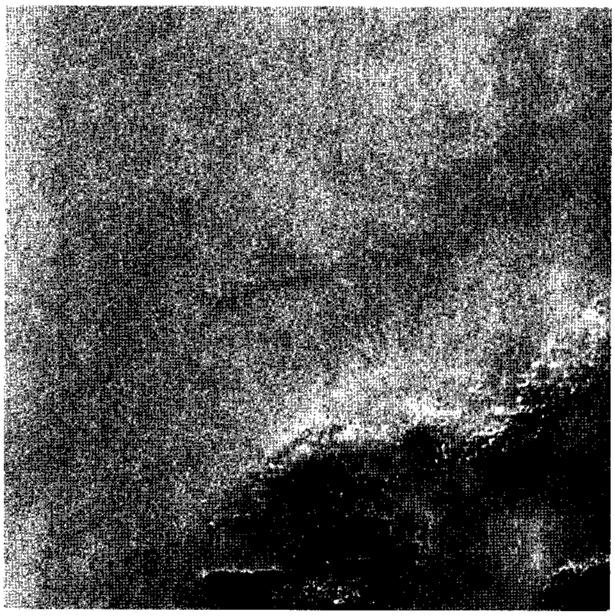

04-11-91

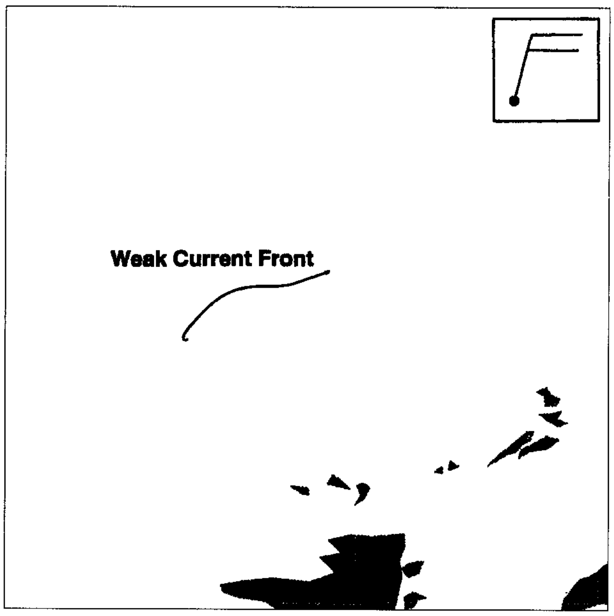

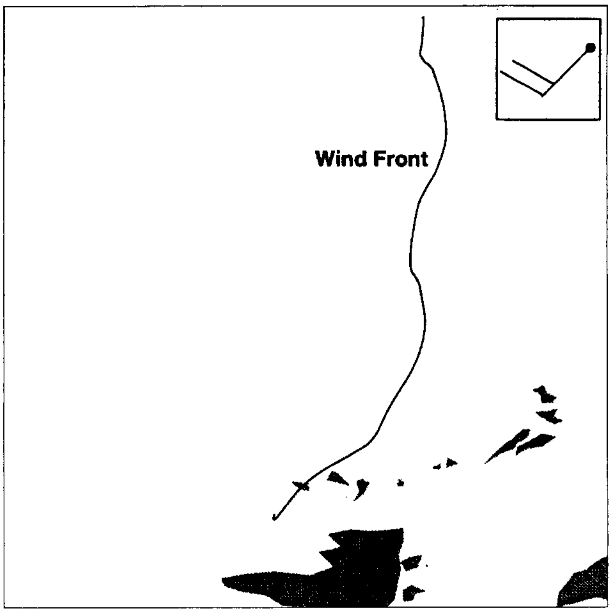

07-11-91

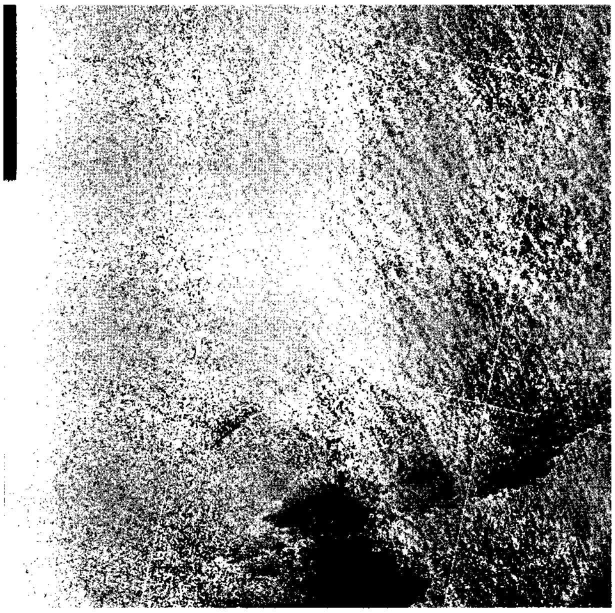

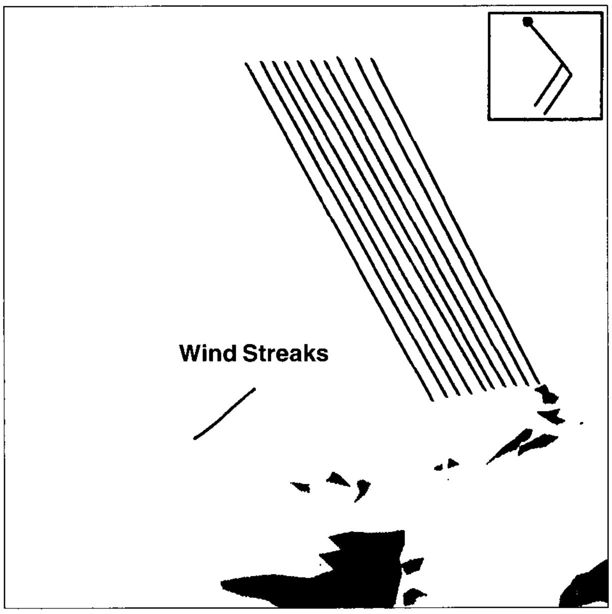

10-11-91

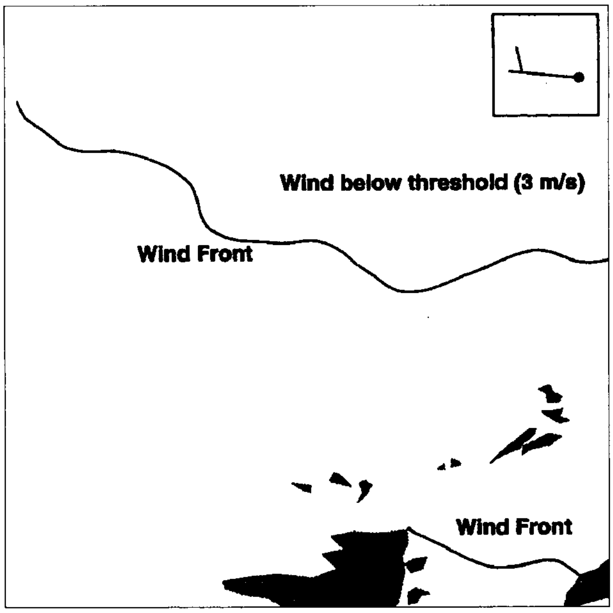

13-11-91

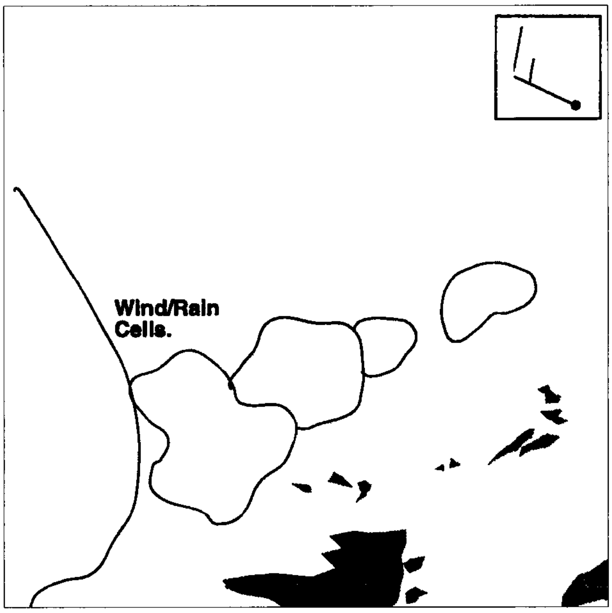

16-11-91

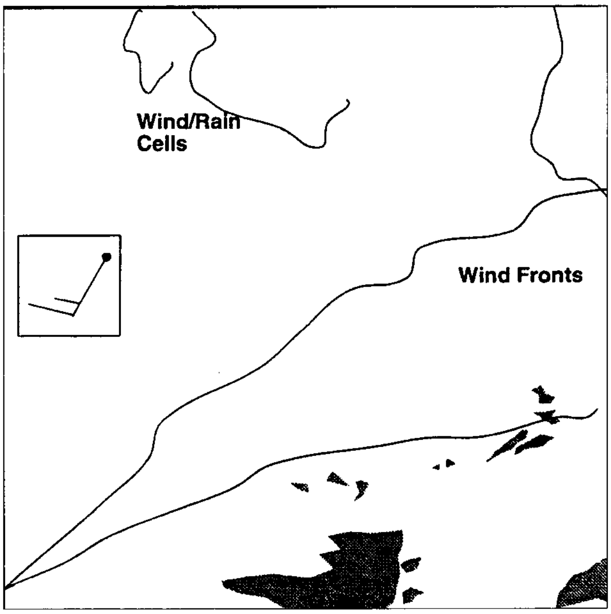

19-11-91

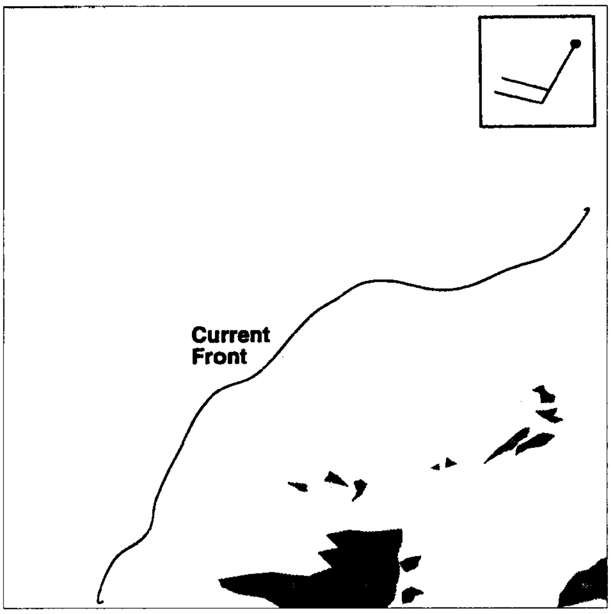

22-11-91

25-11-91

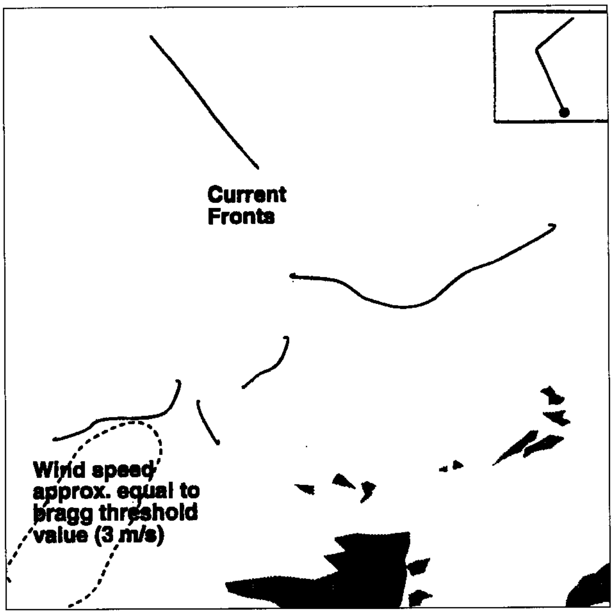

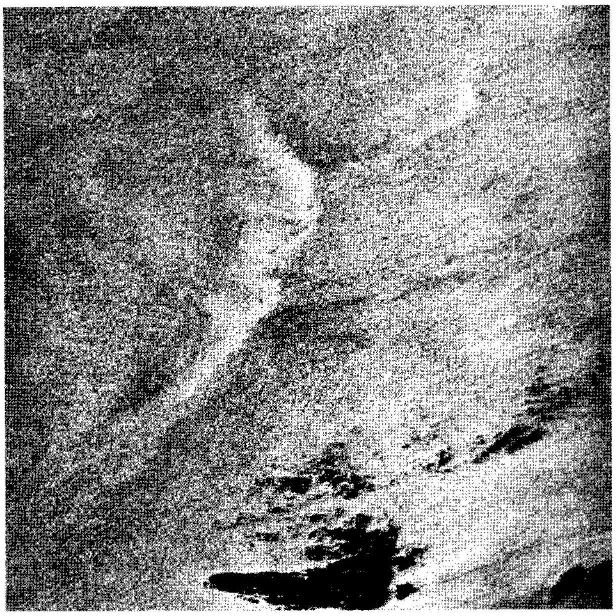

28-11-91

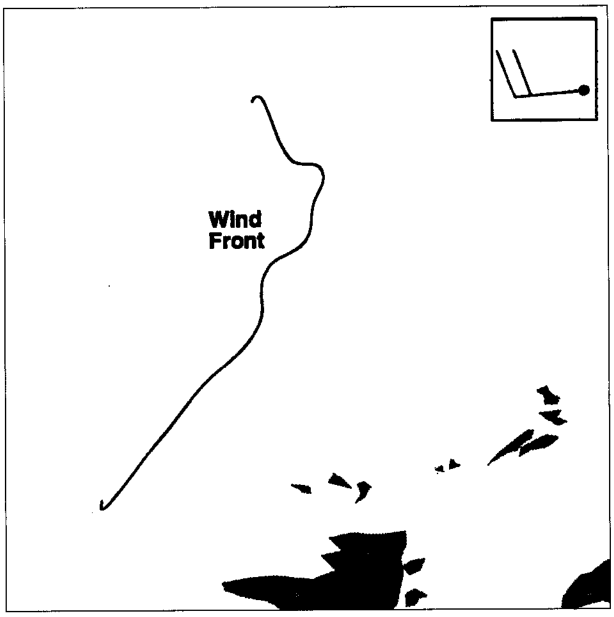

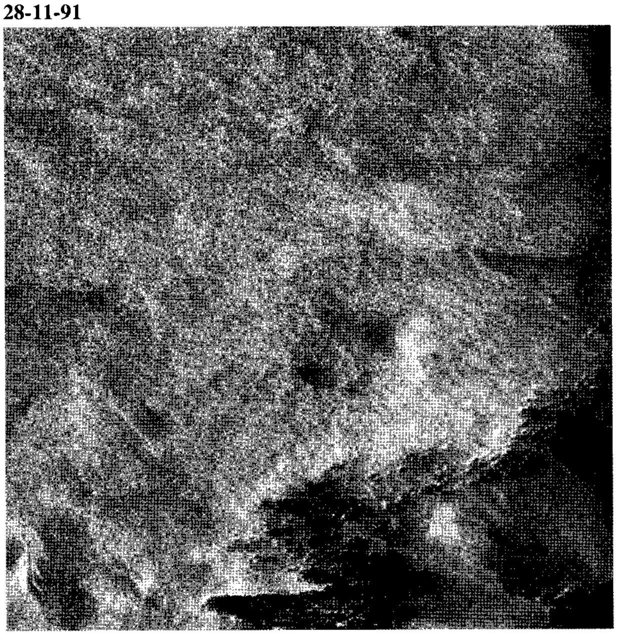

01-12-91

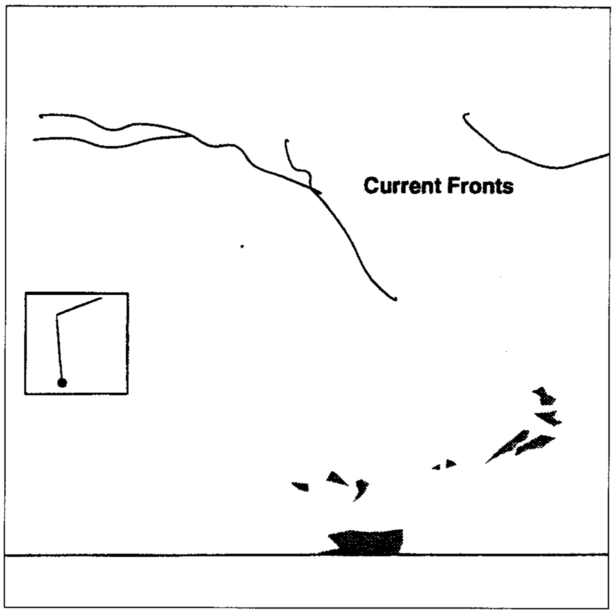

04-12-91

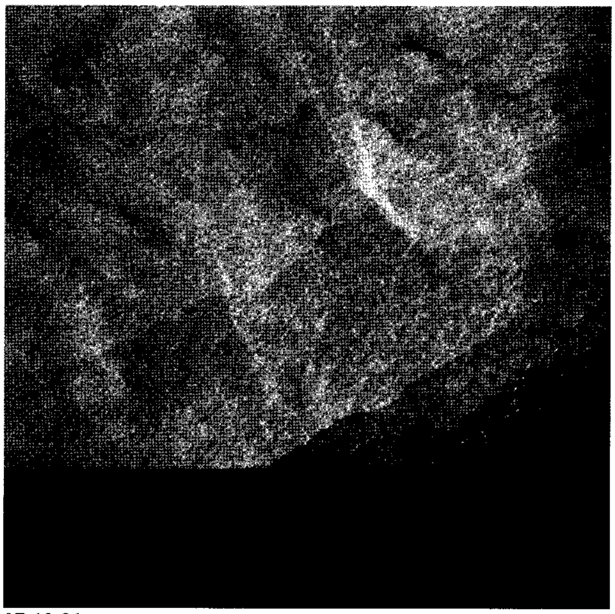

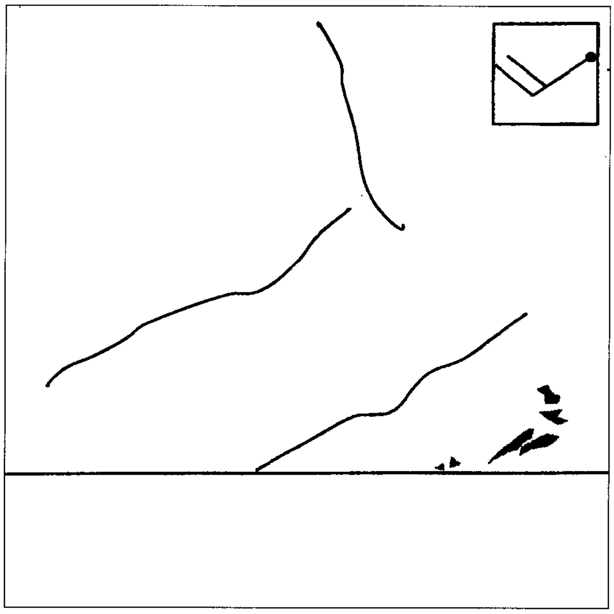

07-12-91

4.2 Seasonally

The seven images presented in this section have all been obtained along the west coast of Norway and cover the period from February to December 1993. The time and position of each image is shown in Figure 53. Calm weather during the spring and summer causes images from those seasons to have features dominantly expressed by the presence of natural film such as spiralling eddies. On the other hand, during autumn and winter, when the weather is at its roughest, images are dominated by wind streaks, wind fronts and current fronts predomaintly expressed by short-wave/current interaction. This visible difference in image expression with the season can clearly be seen by comparing images A and C, or images B and F.

Brief description of the images:

06-02-93 (A): Current shears along the coast and internal waves in the upper left-hand corner.

06-05-93 (B): Low wind and natural film combine to make the dark band that dominates the image. Several spiralling eddies are seen. Parts of this image have been discussed earlier in Sections 3.2.5 and 3.2.2.

22-05-93 (C): A very spectacular image in which natural film has accumulated and the dark bands form this 'fractal' image. Several spiralling eddies are again seen.

05-06-93 (D): One of the few summer images without any slick features. An internal wave train is clearly seen in the lower part of the image just north of the island Utsira.

03-08-93 (E): Low wind near the coast causes the dark band. No evidence of slicks are seen offshore.

04-10-93 (F): Dominated by current fronts along the coast. As seen in the upper left-hand corner, natural film still appears this late in the year. The dark areas in the fjords are due to sheltering of the water by the land.

02-12-93 (G): The image is dominated by current boundaries along the coast and a weak wind front in the lower left-hand corner. The primary expressions in this image have been discussed in more detail in Section 3.2.1.

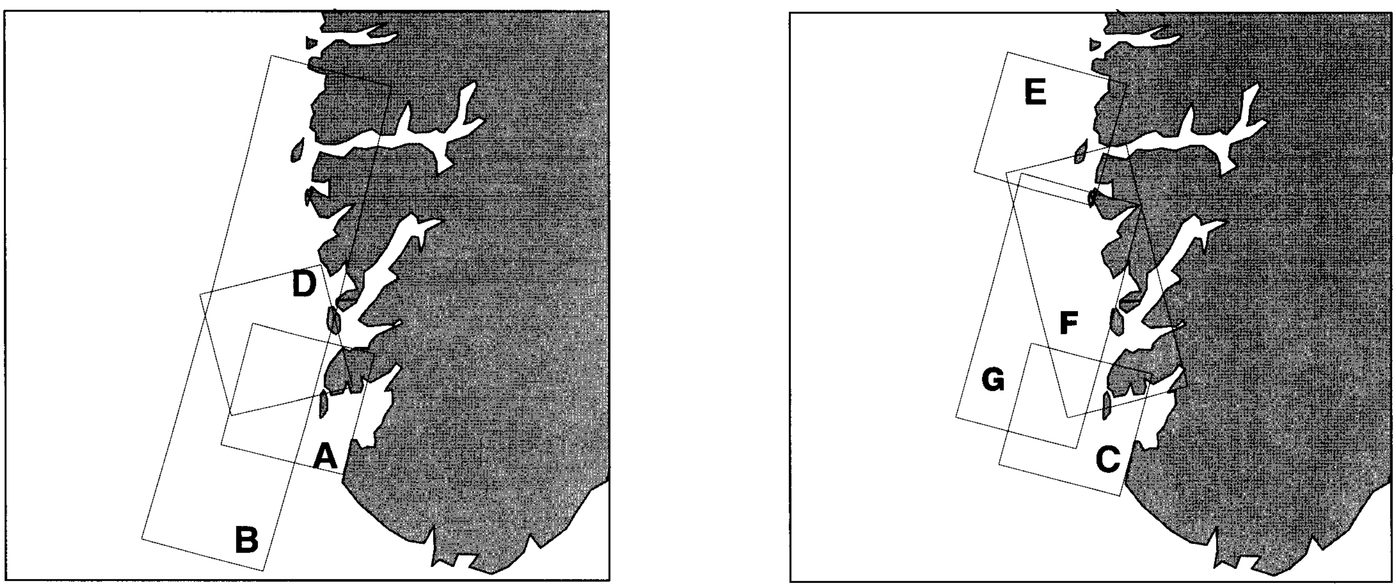

Figure 53: Position of the images used in this section — A: 6 February; B: 6 May; C: 22 May; D: 5 June; E: 3 August; F: 4 October; G: 2 December

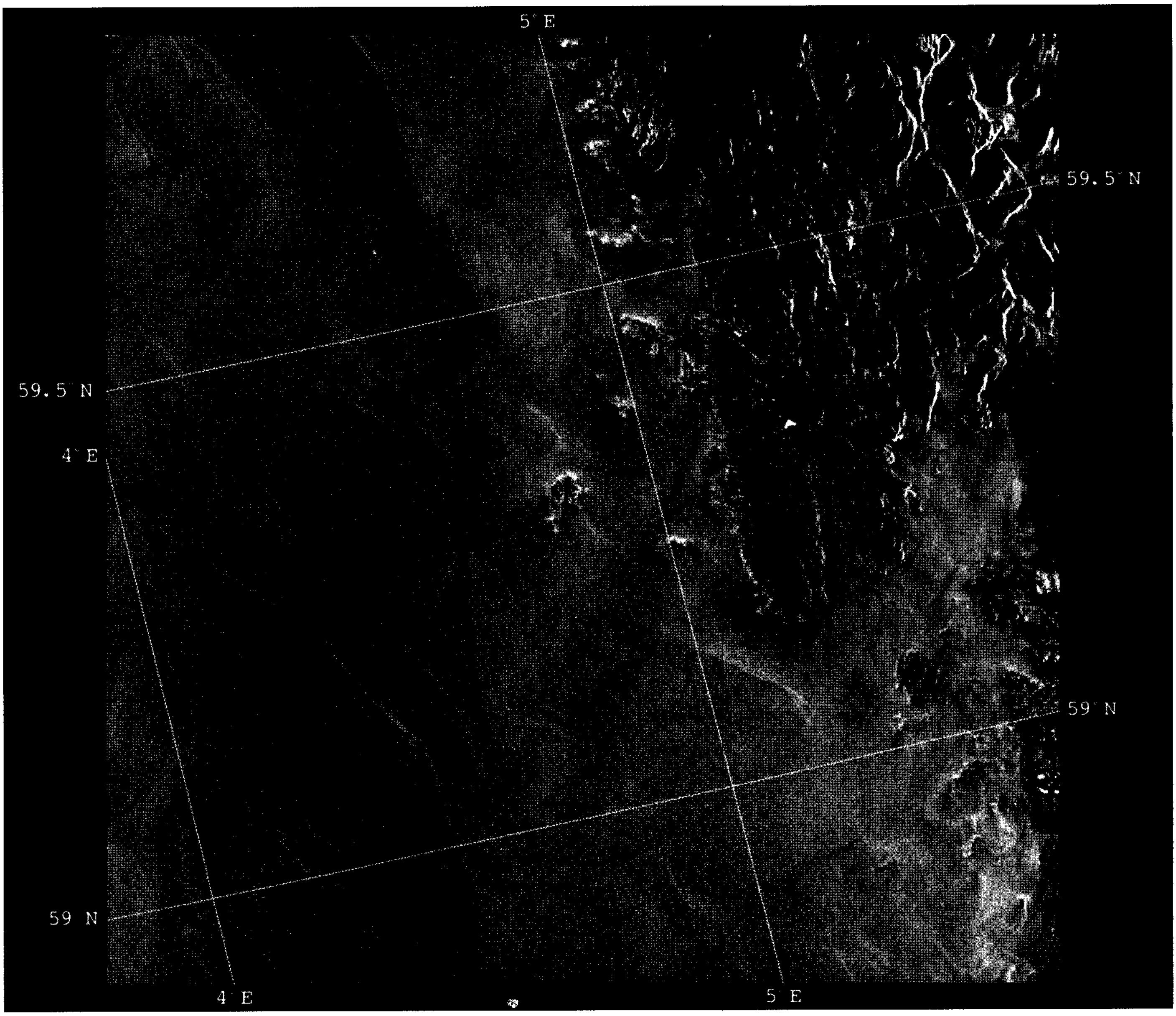

06-02 -93

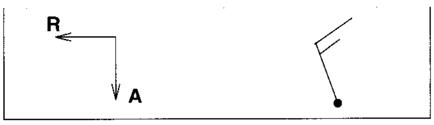

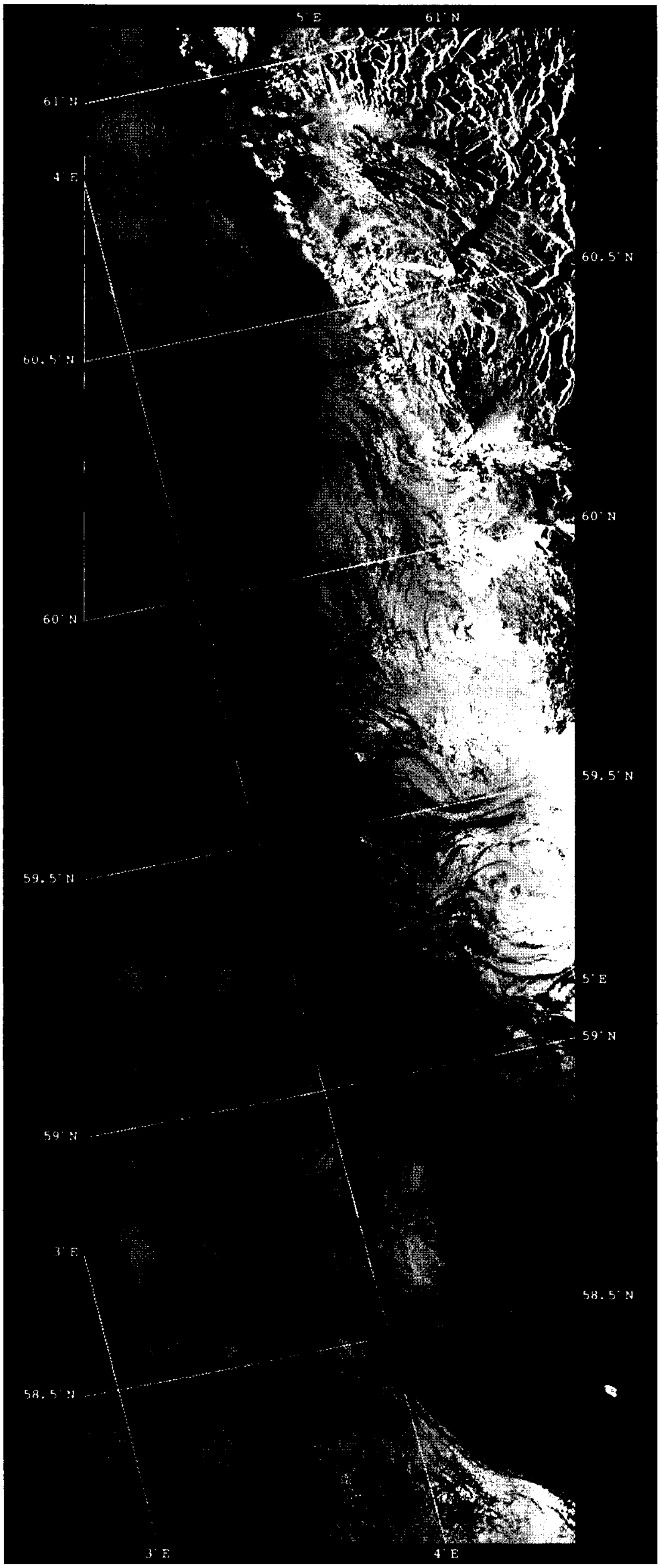
5°E
61°N
61°N
4°E
60.5°N
60.5°N
60°N
60°N
59.5°N
59.5°N
5°E
59°N
59°N
3°E
58.5°N
58.5°N
3°E
4°E

06-05-93


R
A

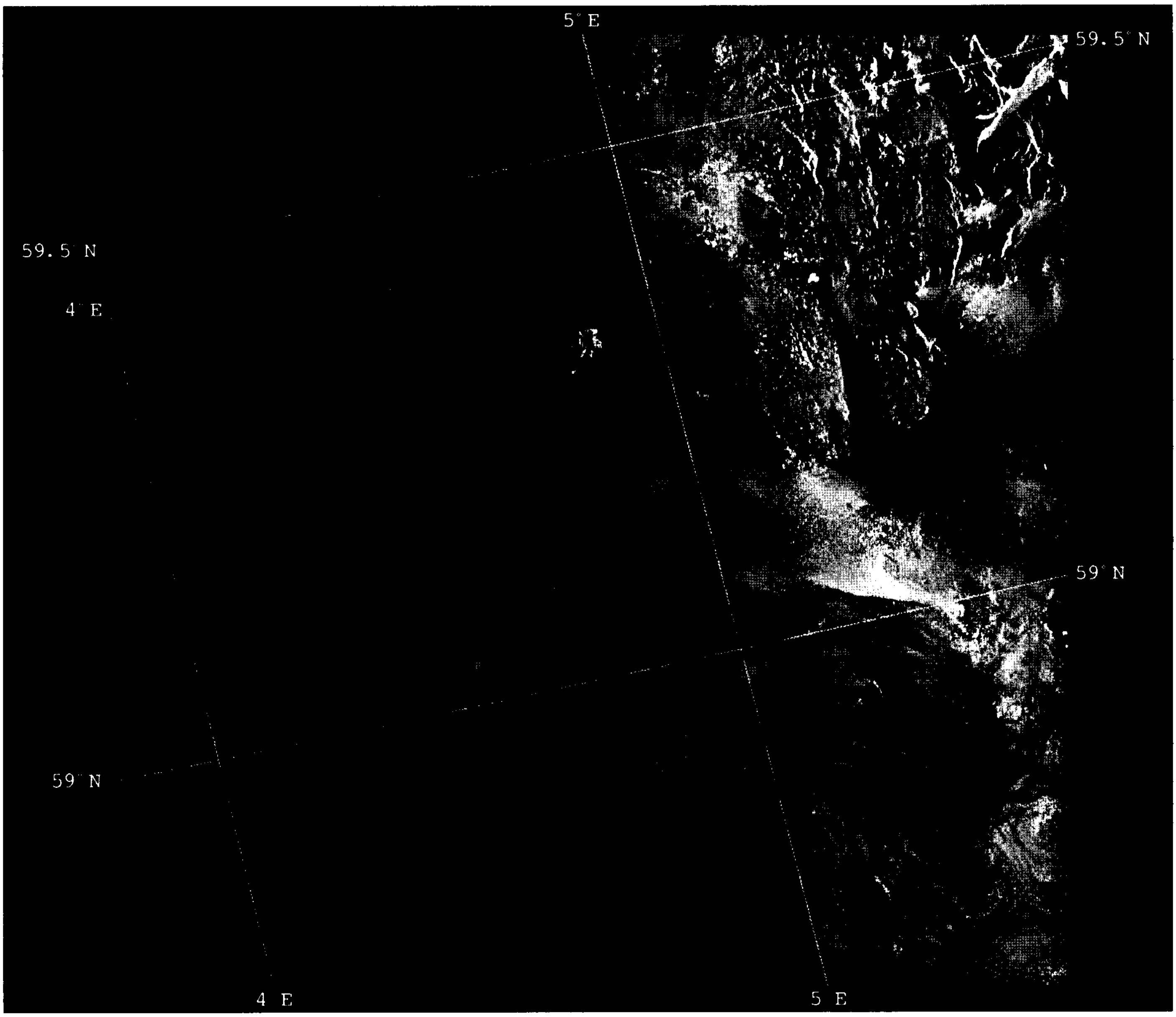

22-05-93

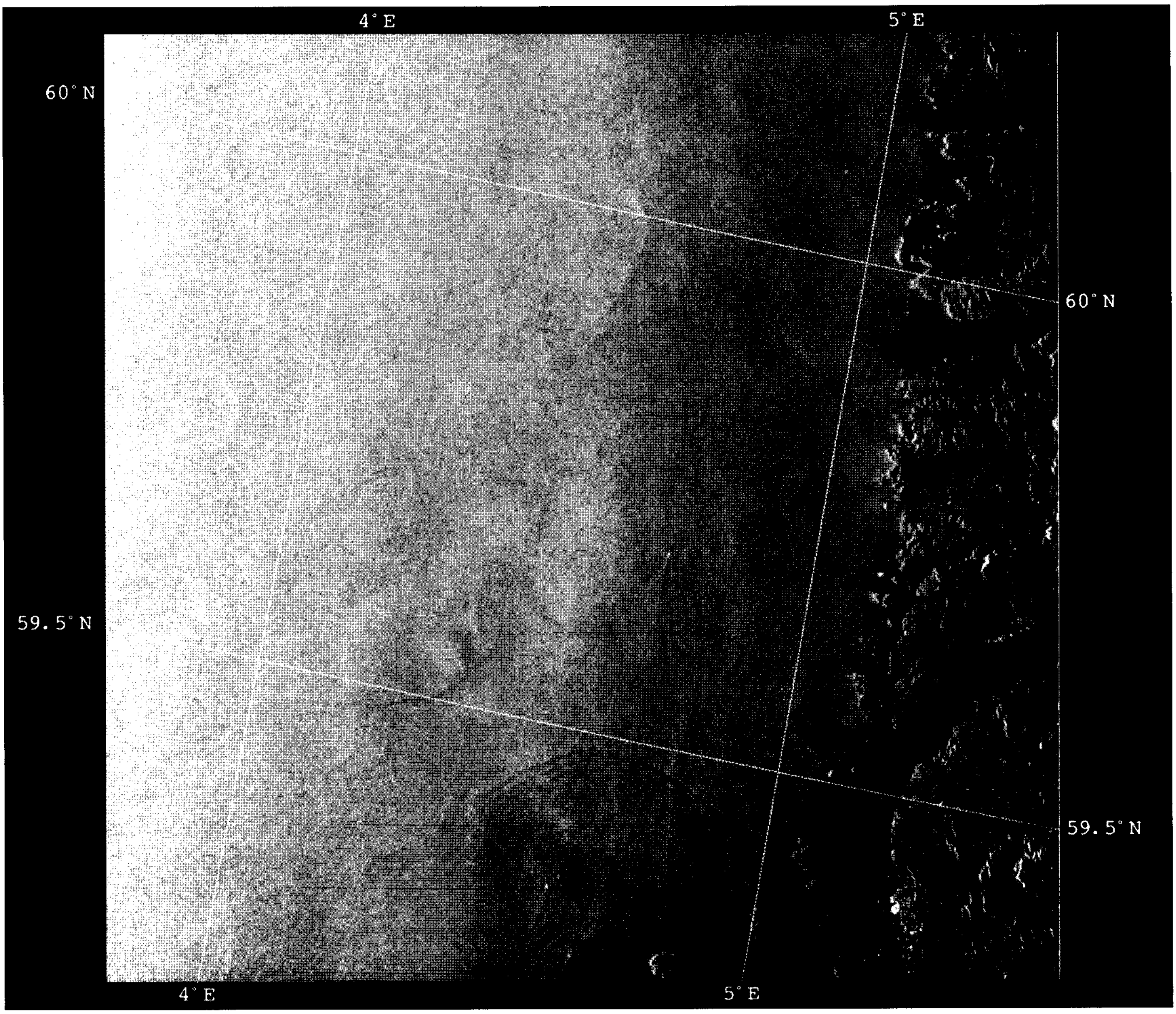

05-06-93

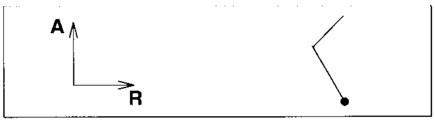

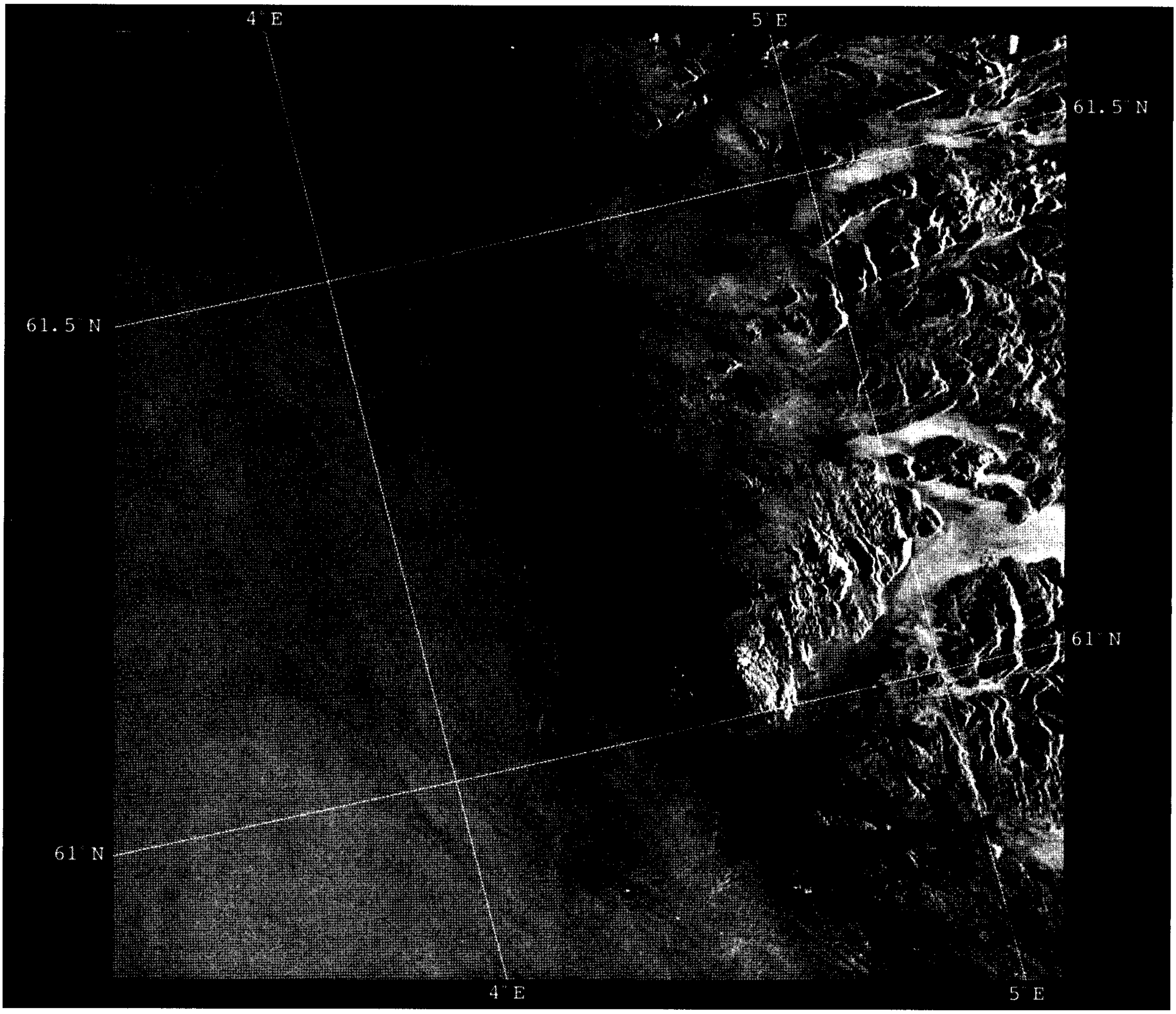

03-08-93

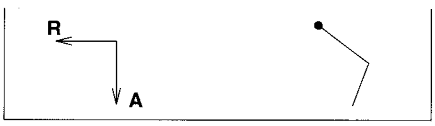

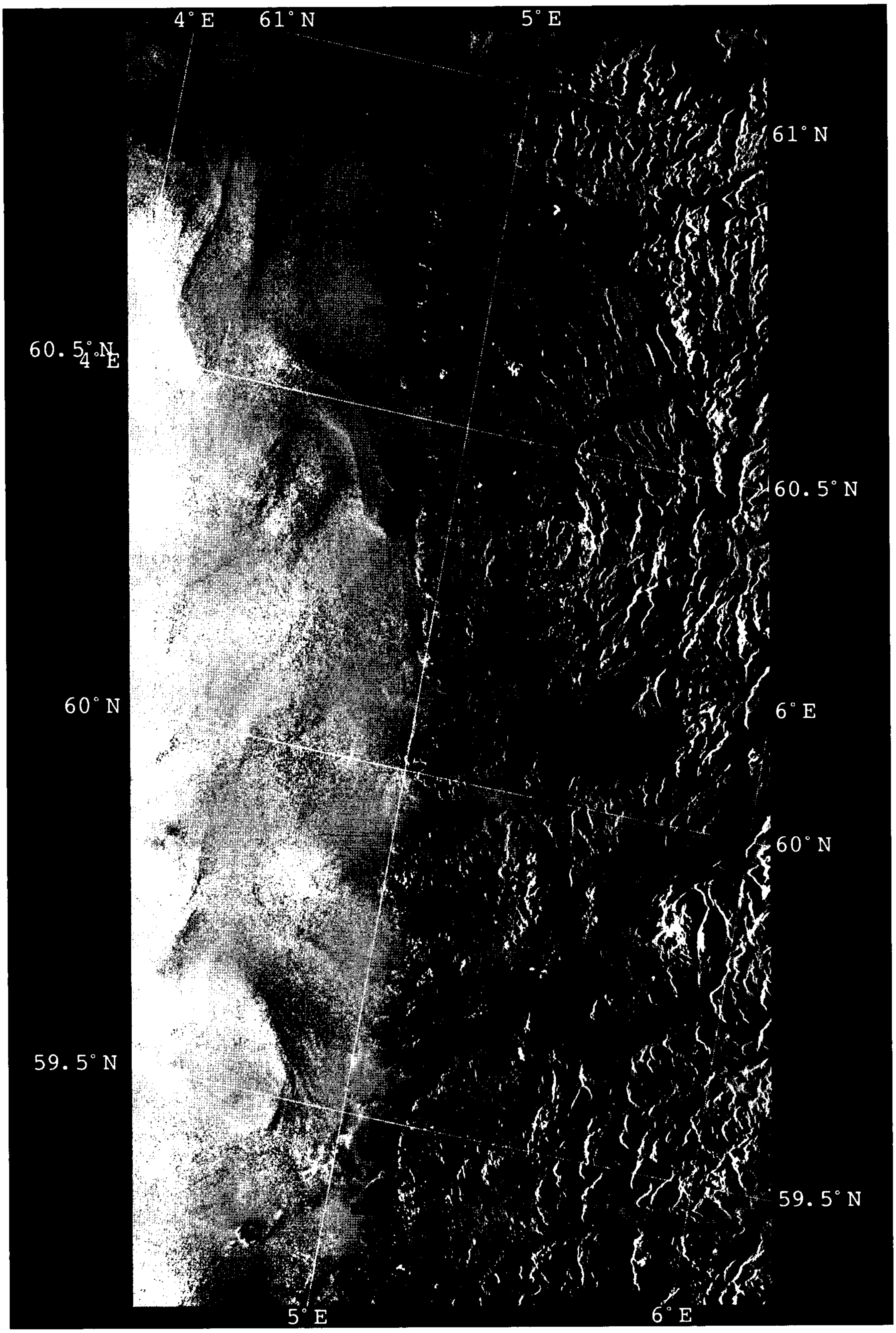

04-10-93

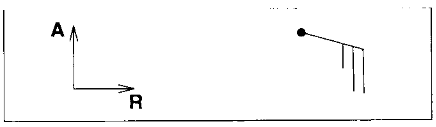

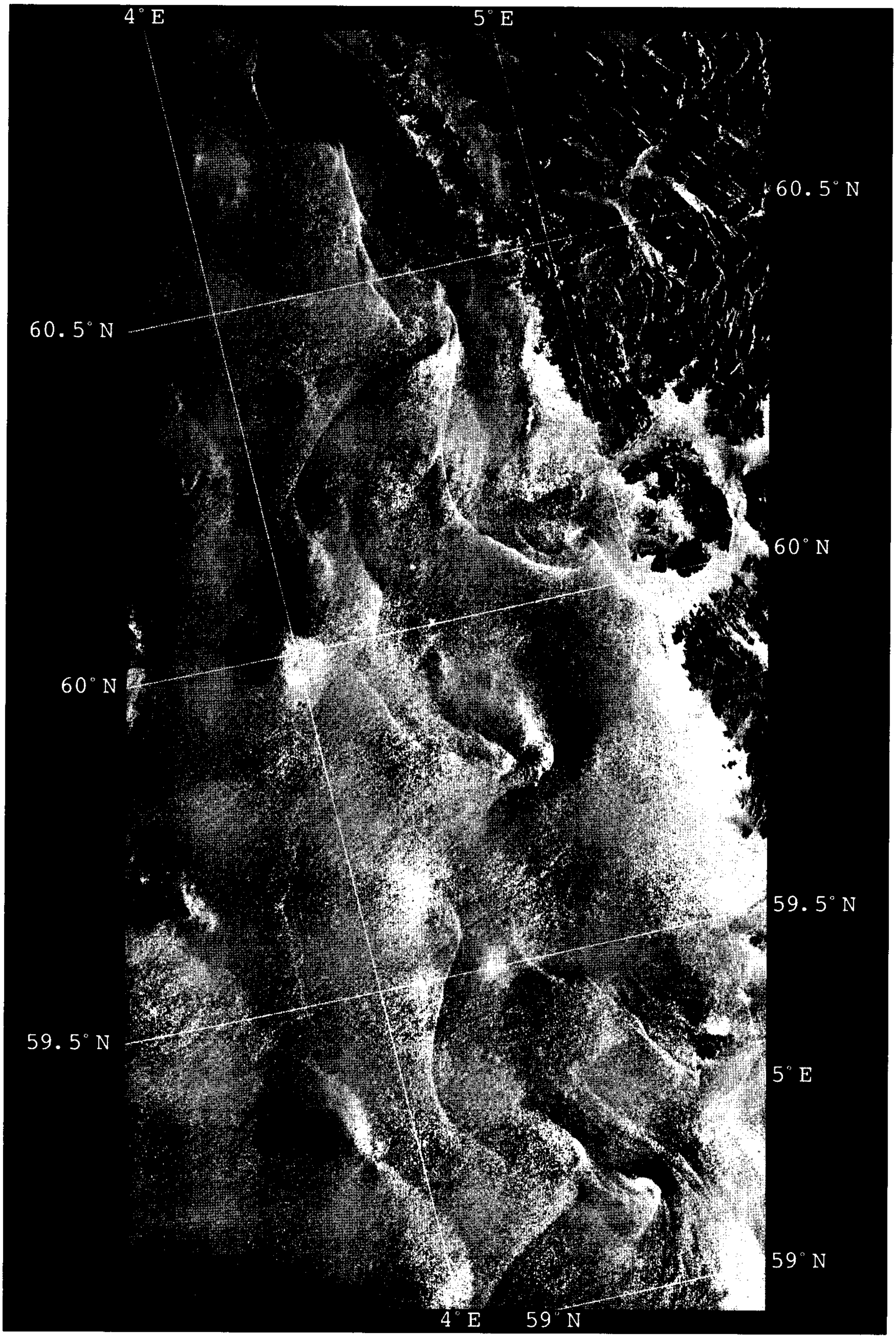

02--12-93

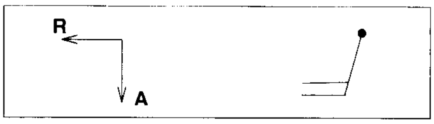

References

1. Alpers., W. & Brümmer, B., Athmospheric boundary layer rolls observed by SAR onboard the ERS-1 satellite, *J. Geophy. Res.* **99,** 12613-12621 (1994).
2. Alpers, W., Wismann, V., Theis, R., Hühnerfuss, H., Bartsch., N., Moreira, J. & Lyden, J., The damping of ocean surface waves by monomolecular sea slicks measured by airborne multi-frequency radars during the saxon-fpn experiment, *IGARSS'91 (International Geoscience and Remote Sensing Symposium), Finland, June* (1991).
3. Alpers, W.R., Theory of radar imaging of internal waves, *Nature,* **314**, 245 (1985).
4. Askari. F., Geernaert, G., Keller, W. & Raman, S., Radar imaging of thermal fronts, *Int. J. Rem. Sens.* **14**(2) (1993).
5. Beal, R.C., DeLeonibus, P.S. & Katz, I., *Spaceborne Synthetic Aperture Radar for Oceanography,* The Johns Hopkins University Press, Baltimore, MD, USA (1981).
6. Bern, T., *Norwegian Slick Study, Vol. 1: Oil slick study.* Technical report, Oceanor, Trondheim, Norway (1993).
7. Donelan, M. & Pierson, W., Radar scattering and equilibrium ranges in wind-generated waves with applications to scatterometry, *J. Geophys. Res.* **92,** C5 (1987).
8. Elachi, C., *Spaceborne Radar Remote Sensing.* IEEE Press., New York, USA (1988).
9. Fu, L.L. & Stewart, R.H., Some examples of detection of oceanic mesoscale eddies by Seasat synthetic aperture radar, *J. Geophys. Res.* **88**, 1844-1852 (1983).
10. Gjevik, B. & Marthinson, T., Three-dimensional lee-wave pattern, *Quart. J. Roy. Met. Soc.,* **104**, 947-957 (1978).
11. Gossard, E. & Hooke, W.H., *Waves in the Atmosphere.* Elsevier, New York (1975).
12. Hünerfuss, H. & Walter, W. and Lange, P. & Alpers, W., Attenuation of wind waves by monomolecular sea slicks and the Marangoni effect, *J. Geophys. Res.* **92** (1987).
13. Hasselmann, K. & Hasselmann, S., On the nonlinear mapping of an ocean wave spectrum into a SAR image spectrum and its inversion, *J. Geophys. Res.* **96** 10713-10729 (1991).
14. Hasselmann, K., Raney, R.K., Plant, W.J., Alpers, W., Shuchman, R.A., Lyzenga, D.R., Rufenach, C.L. & Tucker, M.J., Theory of Synthetic Aperture Radar ocean imaging: A MARSEN view, *J. Geophys. Res.* **90**, 4659-4686 (1985).
15. Haugan, P.M., Evensen, G., Johannessen, J.A., Johannessen, O.M. & Petterson, L.H., Modeled and Observed Mesoscale Circulation and Wave-Current Refraction During the NORCSEX'88, *J. Geophys. Res.* **96**, 10411-10422 (1991).
16. Hovland, H., Johannessen, J.A. & Digranes, G., *Norwegian Surface Slick Report,* Technical report, Nansen Environmental and Remote Sensing Center (1993).
17. Hughes, B.A., Introduction, JOWIP and SARSEX special issue, *J. Geophys. Res.* **93** (1988).
18. Johannessen, J.A., Røed, L.P. & Wahl, T., Eddies Detected in ERS-1 SAR Images and Simulated in Reduced Gravity Model, *Int. J. Rem. Sens.* **14**, 2203 (1993a).

19. Johannessen, J.A., Shuchman, R.A., Davidson, K., Frette, Ø., Digranes, G. & Johannessen, O.M., Coastal Ocean Studies With the ERS-1 SAR, During NORCSEX'91, *Space at the Service of our Environment, Proc. First ERS-1 Symposium,* ESA SP-359, 113-117 (1993b).
20. Johannessen, J.A., Shuchman, R.A., Digranes, G., Wackerman, C., Johannessen, O.M., Lyzenga, D. & Vachon, P.W., Coastal ocean fronts and eddies imaged with ERS-1 SAR, submitted to *J. Geophys. Res.* (1994a).
21. Johannessen, J.A., Shuchman, R.A. & Johannessen, O.M., Mesoscale variability studies with SAR, on ERS-1, *Oceanographic Application of Remote Sensing,* Ikeda, M. and Dobson, F. (Eds.), CRC Press Inc., Boca Raton, USA, in press (1994b).
22. Johannessen, J.A., Shuchman, R.A., Johannessen, O.M., Davidson, K.L. & Lyzenga, D., Synthetic Aperture Radar Imaging of Upper Ocean Circulation Features and Wind Fronts, *J. Geophys. Res.* **96**, 10411-10422 (1991).
23. Johannessen. J.A., Svendsen, E., Johannessen, O.M. & Lygre, K., Three-dimensional structures of mesoscale eddies in the Norwegian Coastal Current. *J. Phys. Oceanogr.* **19**, 3-19 (1989).
24. Kirwan, A.D., Ahrens, T.J. & G.H.B. (Eds.), Seasat special issue II, *J. Geophys. Res.* **88**, 1531 (1983).
25. Krogstad, H.E., A simple derivation of Hasselmann's nonlinear ocean-SAR transform, *J. Geophys. Res.* **97**, 2421-2425 (1992).
26. LeMone, M.A., The Structure and Dynamics of Horizontal Roll Vortices in the Planetary Boundary Layer, *J. Atmos. Sci.* **30**, 1077-1091 (1973).
27. Lichy, D.E., Mattie, M.G. & Mancini, L.J., Tracking of a warm water ring, *Spaceborne Synthetic Aperture Radar from Oceanography,* The Johns Hopkins University Press, 215 (1981).
28. Ochadlick, A., Cho, P. & Evans-Morgis, J., SAR observations of currents colocated with slicks, *J. Geophys. Res.* **97** (1992).
29. Palm, E. & Foldvik, A., Contribution to the theory of two-dimensional mountain waves, *Geofysiske Publikasjoner, Geophysica Novegica,* **XXI**(6), 1-30 (1960).
30. Raney, R.K., Synthetic aperture imaging radar and moving targets, *IEEE Trans. Aerospace Elect. Sys.,* **AES-7**(3), 499-505 (1971).
31. Raney, R.K., SAR response to partially coherent phenomena, *IEEE Trans. Antennas Propagat.,* **AP-26**(6), 777-787 (1980).
32. Rufenach, C., Shuchman, R.A., Wackerman, C., Johannessen, J.A. & Davidson, K., Wind and atmospheric boundary layer retrieval from ERS-1 SAR, submitted to *J. Geophys. Res.* (1994).
33. Sandven, S. & Johannessen, O., Ice Studies in the Barents Sea by ERS-1 during SIZEX 92, *NERSC Conference Report No. 4, Proceedungs of the Second Scandinavian SAR Symposium,* (1992).
34. Scott, J., Surface Films in Oceanography, *ONRL Workshop Report C-11-86,* 19 (1986).
35. Stoffelan, A. & Anderson, D.L.T., ERS-1 scatterometer data characteristics and wind retrieval skill, *Space at the Service of our Environment, Proc. 1st ERS-1 Symp., 4-6 Nov. 1992, Cannes, France,* ESA SP-359, Vol. 1, 41-47 (1993).
36. Swift, C.T. & Wilson, L.R., Synthetic aperture radar imaging of moving ocean waves, *IEEE Trans. Antennas Propagat.,* **AP-27**(6), 725-729 (1979).
37. Thomson, R.E., Vachon, P.W. & Borstad, B.A., Airborne synthetic aperture radar imagery of atmospheric gravity waves, *J. Geophys. Res.* **97**, 14249-14257 (1992).
38. Vachon, P.W., Johannessen, O.M. & Johannessen, J.A., An ERS-1 SAR Image of Atmospheric Lee Waves, *J. Geophys. Res.* 99(C11), 15 Nov. (1994).

39. Vesecky, J., & Stewart, R., The observation of ocean surface phenomena using imagery from the SEASAT SAR: an assessment, *J. Geophys. Res.* **87**(C5) (1982).
40. Wahl, T., Andersen, T. & Skøelv, Å, *Oil Spill Detection Using Satellite based SAR: Pilot Operation Phase, Final Report,* Technical report, NDRE (1994).
41. Wakker, K.F., Zandbergen, R.C.A., Naeij, M.C. & Ambrosius, B.C., Geosar altimeter data analysis for the oceans around South Africa, *J. Geophys. Res.* **95** (1990).
42. Wright, J.W., Detection of ocean waves by microwave radar: The modulation of short gravity-capillary waves, *Boundary Layer Meteorol.* **13**, 87-105 (1978).
43. Lichtenegger, J. Using ERS-1 SAR images for oil spill surveillance, *Earth Observation Quarterly 44,* (June 1994).

Appendix

Some relevant publications

The following abstracts are of four relevant publications. Reprints are available on request from:

Nansen Environmental and Remote Sensing Center
Edv. Griegsvei 3A
N-5037 Solheimsviken, Bergen
Norway
Phone: +47 55 29 72 88
Fax: +47 55 20 00 50

Eddies Detected in ERS-1 SAR Images and Simulated in Reduced Gravity Model.

J.A. Johannessen, L.P. Røed and T. Wahl
Int. J. Rem. Sens. **14**, 2203 (1993)

The first ERS-1, C-band SAR image of the western coast of Norway was received at Tromsø Satellite Station, Norway, on 21 August 1991. It clearly depicts an eddylike structure located in the coastal waters. The eddy has a cyclonic spiral structure with a diameter of about 5 km. The expressions of the dark lines outlining the spiral are probably caused by the presence of natural surface slicks resulting in a damping of the Bragg scattering waves. Eddies at this particular location with the same spatial characteristics are also detected in simulations with a nonlinear, one layer active reduced gravity model. From the model results we conclude that the eddy is formed by horizontal current shear instability associated with variations in the larger scale coastal current. A second case of an observed and simulated eddy occurred later in the Outer Oslofjord. The simultaneous observations and simulations of these eddies clearly demonstrate the potential advantage in integrated use of weather-independent SAR data and model results for the monitoring and modelling of mesoscale coastal circulation processes.

Oceanographic Application of Remote Sensing; SAR on ERS-1.

J.A. Johannessen, R.A. Shuchman, and O.M. Johannessen
Oceanographic Application of Remote Sensing: Ocean Circulation Dynamics: Mesoscale variability, SAR on ERS-1, edited by F. Dobson and M. Ikeda, CRC Press, Boca Raton, Florida, US (in press)

The first European Space Agency remote sensing satellite, ERS-1, was successfully launched on July 17, 1991 carrying a suite of microwave and infrared instruments. Since launch, a total of approximately 400,000 synthetic aperture radar (SAR) images, each 100×100 km with a center incidence angle of 23°, have been collected over the ocean and sea ice surfaces. Unlike the infrared radiometers and visible imaging the SAR is unaffected by cloud cover and visible light conditions, and unlike the radar altimeter the SAR obtains a two-dimensional image of the surface. In this paper we will provide an assessment of the capabilities and uniqueness of the vertical polarization, ERS-1 band SAR in imaging of upper ocean circulation features. For the ocean surface, high resolution (16 × 20 m) SAR images are principally formed by resonant Bragg scattering whereby the transmitted 0.056 m radar waves, insensitive to clouds, fog and visible light conditions, are reflected back to the antenna by short gravity waves of approximately the radar wavelength. These surface waves are formed primarily in response to the surface wind stress. Spatial variations of these short waves are frequently observed in SAR images as pointed out in several papers. These variations are usually induced by larger scale features and processes such as long gravity waves, variable wind velocities and stratification in the marine atmospheric boundary layer, and variable currents associated with upper ocean circulation features including fronts, eddies, upwelling and internal waves, tidal circulation as well as bottom topography. In spite of the remarkable imaging capabilities reported from Seasat and SIR-A/B, the lack of space-borne SAR data, between Seasat (launched in July 1978 and failed in October 1978), SIR-A/B (Space Shuttle flight A in November 1981 and flight B in October 1984), ALMAZ-1 (launched in March 1991 and ended in October 1992) and ERS-1 (launched in July 1991), has to some extent limited the development of SAR application areas in oceanography. Most of the systematic studies of radar backscatter from the ocean have meanwhile been obtained through airborne SAR imaging campaigns, in particular providing essential understanding of SAR imaging of wind waves and swell. However, since the launch of ALMAZ-1 and ERS-1, spaceborne SAR data have been regularly available, and a large number of validation studies have been conducted that are promising for improved quantitative understanding of the SAR imaging mechanisms and subsequent application in oceanography including air-sea interaction.

An ERS-1 SAR Image of Atmospheric Lee Waves

P.W. Vachon, O.M. Johannessen and J.A. Johannessen
J. Geophys. Res., Oceans, 99, (C11) 15 Nov. (1994)

An ERS-1 synthetic aperture radar (SAR) image of the island Hopen and the surrounding ice pack shows a distinct long wavelength scale phenomenon near the island. The phenomenon is interpreted as the surface imprint in open water regions of atmospheric lee waves. The physical setting for the observation is presented and discussed. Analysis results based upon a lee-wave model with an atmosphere having an exponential Scorer Parameter profile and a bell-shaped barrier are shown to be compatible with the SAR-observed phenomenon.

SAR Imaging of Marine Boundary Layer Processes

J.A. Johannessen, P.W. Vachon and O.M. Johannessen
Earth Observation Quarterly (ESA), 46 (Dec. 1994)

Combination of spaceborne synthetic aperture radar (SAR) images and advanced very high resolution radiometer (AVHRR) images is shown to improve quantitative interpretation of the radar imaging mechanism for the ocean surface. This in turn leads to more complete understanding of geophysical processes in the marine environment. We examine two case studies: first, the structure of horizontal roll vortices in the atmospheric boundary layer imaged bv SAR (sea surface roughness) and by infrared radiometer (IR) (cloud top temperature); and second, features of mesoscale coastal circulation also imaged by SAR (sea surface roughness) and IR (ocean surface temperature).

Geophysical Glossary

Advective motion
Motion in liquids and gases whereby heat, for example, is transported in a horizontal direction.

Anticyclonic
Sense of rotation about the local vertical that is clockwise in the Northern Hemisphere, counterclockwise in the Southern Hemisphere and undefined at the equator.

Atmosphere boundary layer
The layer of air directly above the Earth's surface (land and ocean). Over open ocean, the layer usually has a vertical depth of less than 2 km.

Buoy
A platform at or below the sea surface for carrying instruments to measure oceanographical and meteorological parameters.

Buoyancy frequency
Maximum frequency of internal waves [q.v.].

Capillary waves
Waves at the surface of the sea caused by surface tension. The wavelength of capillary waves is of the order of 1 cm.

Convective motion
Motion in liquids and gases whereby heat, for example, is transported in a vertical direction.

Coriolis force
A force due to the Earth's rotation that acts on the motion of air and water masses.

Current front
The boundary between two areas of different current speed and direction, often associated with different water masses.

Cyclonic
Sense of rotation about the local vertical that is counterclockwise in the Northern Hemisphere and clockwise in the Southern Hemisphere.

Eddies
Circular ocean currents having a horizontal scale of between 10 and 100 km.

Eddy orbital motion
Rotational velocity of an eddy.

Geostrophic velocity
Motion of air and water masses caused by the balance between the Coriolis force and the pressure-gradient force in the horizontal plane.

Geostrophic wind
A wind whose direction and speed are determined by a balance of the pressure-gradient force and the force due to the Earth's rotation.

Gravity waves
Waves in the atmosphere, at the ocean surface and in the interior of the ocean (internal waves [q.v.]).

Hydrodynamic modulation
A mechanism at the sea surface responsible for the varying backscatter of SAR microwaves.

Hydrophobic oil
Water-repellent oil.

Internal waves
Waves in the deep ocean; in SAR images such waves having a wavelength of 1 to 5 km are often observable.

Inversion layer
A layer in the atmosphere in which the temperature increases with height; this is the reverse of the normal situation where temperature decreases with height.

Isobar
Lines joining point of equal atmospheric pressure.

Jet
Narrow and intense current or wind.

Lee waves
Gravity waves [q.v.] created in the atmosphere by the perturbation of air masses flowing over a mountain.

Mesoscale currents
Ocean currents appearing in patterns ranging in scale from tens to hundreds of kilometres.

Meander
A deviation of the flow pattern of a current.

Natural film
A thin layer at the sea surface consisting of biochemical material.

Orographic interaction
The modification of the characteristics of air masses flowing over mountains, valleys and other topographic features.

Roll vortices
Cloud streaks observed in visual satellite images over open ocean and caused by convergence and upward motion between the circulating helices in the atmospheric layer. The rolls are oriented parallel to the main wind direction.

Shear zone
Current front with sharp gradient.

Slicks
Dark patches on the surface of the sea observed in SAR images and caused by a thin layer of oil or other natural substances (surfactants [q.v.]) that damps the short surface waves.

Squall lines
Features in SAR images caused by sudden wind gusts.

Stratification
Vertical density structure of the atmosphere or ocean, caused by different air or water masses.

Surfactants
Chemical or biological substances that form a film at the sea surface.

Swell
Ocean waves that have travelled away from the area in which they were generated; they are of relatively large wavelength and period and are regular in character.

Synoptic wind
The wind field in a region at a specified time.

Temperature front
A boundary between two water or air masses characterised by a difference in temperature.

Temperature inversion
A layer in a large body of water in which temperature increases with depth.

Tilt modulation
A mechanism at the sea surface responsible for the varying backscatter of SAR microwaves.

Troposphere
The layer of the atmosphere extending from the Earth's surface to an altitude of about 10 km.

Upwelling
The process by which water rises to the surface, usually as a result of wind driven offshore upper layer (Ekman) transport.

Velocity bunching
A mechanism responsible for the varying backscatter of SAR microwaves.

Viscosity
The resistance that a gaseous or or liquid system offers to flow when it is subjected to a shear stress. Also known as flow resistance.

Wave/current interaction
The modification of waves by ocean currents (change in surface wavelength, steepness or direction of propagation).

Wave front
A surface of constant phase.

Wave guide
A layer in the atmosphere or the ocean in which waves can be trapped and caused to propagate horizontally.

Wave number
A wave parameter that is inversely proportional to the wavelength.

Wind front
A boundary between areas of different wind speed and direction.

Wind shear
A local variation of the wind vector or any of its components in a given direction.

Wind wave
A wave resulting from the action of wind on a water surface.